Title

Parametrically-aided sensing in the short-wave infrared frequency band and beyond

Author

Moro, Slaven

Publication Date

2011

UNIVERSITY OF CALIFORNIA SAN DIEGO

Parametrically-aided sensing in the short-wave infrared frequency band and beyond

A dissertation submitted in partial satisfaction of the
requirements for the degree Doctor of Philosophy

in

Electrical Engineering (Photonics)

by

Slaven Moro

Committee in charge:

Professor Stojan Radic, Chair
Professor Dimitri Basov
Professor James Buckwalter
Professor Vitaliy Lomakin
Professor Oleg Shpyrko

2011

The Dissertation of Slaven Moro is approved, and it is acceptable in quality and form for publication on microfilm and electronically:

Chair

University of California San Diego

2011

DEDICATION

To my family

Table of Contents

Signature Page iii
Dedication iv
Table of Contents v
List of Figures vii
List of Tables xv
Acknowledgements xvi
Vita xvii
Abstract of the dissertation xviii
1. Introduction 1
    1.1 Optical remote sensing in the short-wave infrared frequency band 1
    1.2 Overview of existing SWIR technologies 3
    1.3 Porting NIR technology to SWIR via parametric amplification/conversion 7
    1.4 Thesis organization 9
2. Parametric amplification/conversion in $\chi^{(3)}$ nonlinear media 12
    2.1 Fundamental principles 13
    2.2 Degenerate and non-degenerate four-wave-mixing interaction 18
3. Noise in parametric processes 29
    3.1 Introduction 29
    3.2 Statistics of nonlinear phase noise 32
    3.3 Signal/idler phase noise 35
    3.4 Phase modulation noise 39
    3.5 Phase noise due to amplified quantum noise 41
    3.6 Experimental setup 43
    3.7 Experimental results and discussion 45
    3.8 Chapter summary 48
4. Nonlinear frequency chirping vs. nonlinear phase noise 50
    4.1 Introduction 50
    4.2 Statistics of nonlinear phase noise and nonlinear chirp 51
    4.3 Experimental setup 54
    4.4 Experimental results and discussion 56
    4.5 Conclusion 57

5. Parametric gain synthesis in the continuous-wave regime 59
    5.1 Introduction 59
    5.2 One-pump gain synthesis in the NIR 60
    5.3 Sensitivity studies of record high-gain two-pump FOPAs................................68
    5.4 NIR-to-SWIR wavelength conversion 78
    5.5 Chapter summary 81
6. Parametric gain synthesis in the pulsed regime 83
    6.1 Introduction 83
    6.2 Widely-tunable parametric transmitter for CO_2 LIDAR 83
    6.3 Parametrically-preamplifed SWIR receiver 89
    6.4 Chapter summary 94
7. Accessing mid-wave infrared: mixing in non-silica glass fibers 96
    7.1 Introduction 96
    7.2 MWIR-transmitting glass fibers 98
    7.3 Phase-matching via material dispersion 102
    7.4 Chapter summary 107
Appendix A 108
Appendix B 110
Appendix C 115
Appendix D 117
References..121

List of Figures

Figure 1.1: Typical LIDAR system architecture. 2

Figure 1.2: Absorption line strengths of CO_2 and CH_4 (black) with superimposed H_2O (blue). 3

Figure 1.3: Illustration of $\chi^{(3)}$ nonlinear media as a platform for bridging the gap between technologically-mature NIR band and spectroscopic SWIR band. 9

Figure 2.1: Schematic of a one-pump parametric process. 19

Figure 2.2: Schematic of a two-pump parametric process. 20

Figure 2.3: (a) Pump position for SWIR gain synthesis in positive- vs. negative-β_4 fibers; (b) Calculated conversion gain with parameters: P = 100 W, λ_{p+} = 1587.8 nm, λ_{p-} = 1575.0 nm, L = 8 m, γ = 13 $W^{-1}km^{-1}$, λ_0 = 1581 nm, S = 0.025 ps/nm^2-km, and $\beta_4 = \pm 2\times 10^{-56}$ s^4/m. 24

Figure 2.4: Normalized linear phase mismatch as a function of pump-signal (or equivalently pump-idler) separation. 25

Figure 3.1: FOPA model schematic used in the derivation of NPN statistics; Acronyms: OBPF - optical band-pass filter; the rest of the symbols are defined within the text. 33

Figure 3.2: (a) Nonlinear phase SNR vs. pump OSNR and optical Gaussian noise filter 3-dB bandwidth; (b) Signal and idler phase and amplitude SNR spectra due to NPN. 38

Figure 3.3: Spectral dependence of signal phase SNR when only PMN is present (a) for a range of RF noise bandwidths, (b) for 600MHz RF noise bandwidth........41

Figure 3.4: Schematic of parametric amplification of quantum noise in a one-pump FOPA. Acronyms: P_s – signal power, ν_s – signal frequency, ν_p – pump frequency, P_p – pump power, OBPF – optical band-pass filter, ν_i – idler frequency, G_s – signal gain, $\Delta\nu$ – optical filter bandwidth, AQN – amplified quantum noise........42

Figure 3.5: Analytical/numerical signal phase SNR (when only AQN is present): (a) spectrum for two different input signal powers; (b) dependence on input signal power at the signal wavelength of 1545.0nm........43

Figure 3.6: Experimental setup for measurement of phase noise of a FOPA; Inset: electrical waveforms observed after intra-dyne detection of the two output ports of the 90° hybrid. Acronyms: PM – phase modulator, LPF – low-pass (RF) filter, VOA – variable optical attenuator, EDFA – Erbium-doped fiber amplifier, CWDM – coarse wavelength-division multiplexer, HNLF – highly nonlinear fiber, OBPF – optical band-pass filter, LO – local oscillator, ADC – analog-to-digital converter........44

Figure 3.7: (a) Optical spectra for two different signal wavelengths, (b) Measured FOPA gain spectrum........46

Figure 3.8: (a) Optical spectra of pump/signal/idler after HNLF; (b) Signal spectrum before and after FOPA. The three disjoint spectral bands centered on the three characteristic wavelengths (signal - 1545.0nm, pump

- 1568.0nm, and idler - 1591.7nm) have been shifted for easier comparison. 47

Figure 3.9: Measured, simulated, and analytically predicted signal phase and amplitude SNR spectra for input pump OSNR of 40dB. 48

Figure 4.1: Schematic for analytical derivation of NPN/NC statistics; Acronyms: OBPF - optical band-pass filter 51

Figure 4.2: (a) Schematic illustrating the influence of ω^2 weighting factor on two different noise power spectral densities; Standard deviation of (b) NPN and (c) NC vs. pump OSNR and 3-dB optical Gaussian noise filter bandwidth. 54

Figure 4.3: Experimental setup for noise-induced NC measurement; Left inset: measured optical filter transfer functions; Right inset: optical spectrum after HNLF propagation; Acronyms: AM – amplitude modulator, EDFA – Erbium doped fiber amplifier, CWDM – coarse wavelength division multiplexer, OBPF – optical band-pass filter, VOA – variable optical attenuator, SMF – single-mode fiber, Rx – optical receiver. 55

Figure 4.4: (a) Measured pump SNR vs. optical filter bandwidth following PM-to-AM in SMF; (b) Standard deviation of NPN and NC vs. optical filter bandwidth. 57

Figure 5.1: Longitudinal ZDW variations for HNLF 2; dashed line – dispersion map obtained by destructive noise injection method; solid line – dispersion map obtained by non-destructive measurement. 62

Figure 5.2: (a) Numerically simulated gain for segment concatenation 1-2-3-4-5 at a fixed pump power of 36.5 dBm; (b) Simulated gain for several different segment concatenations at a fixed pump wavelength of 1560.4 nm. 63

Figure 5.3: (a) Numerically simulated gain for segment concatenation 1-2-3at a fixed pump power of 36.5 dBm; (b) Simulated gain for several different segment concatenation 1-2-3 at a fixed pump wavelength of 1561.1 nm. 64

Figure 5.4: Experimental setup for FOPA gain measurement. Acronyms: TLS – tunable laser source, PC – polarization controller, PM – phase modulator, EDFA – Erbium-doped fiber amplifier, OBPF – optical band-pass filter; C – combiner, OSA – optical spectrum analyzer. 65

Figure 5.5: Measured gain spectra for 175m long HNLF. 65

Figure 5.6: (a) Measured and simulated gain spectra for HNLF segments 1-2-3; pump wavelength was 1561.225 nm; (b) Measured and simulated gain spectra for HNLF segments 3-4-5; pump wavelength was 1560.290 nm.............67

Figure 5.7: Measured parametric gain for segments 1-2-3 with pump detuned in steps of 0.05 nm. 68

Figure 5.8: Experimental setup for dual-pumped FOPA gain and bit-error-rate measurement. Acronyms: EDFA – Erbium-doped fiber amplifier, LPF – low-pass (RF) filter, PM – phase modulator, AM – amplitude modulator, DWDM – dense wavelength division multiplexer, OBPF – optical band-pass filter, VOA – variable optical attenuator, BERT – bit-error-rate tester. 71

Figure 5.9: (a) Measured FOPA gain spectrum; (b) Measured FOPA gain vs. input signal power at signal wavelength of 1558nm. 73

Figure 5.10: Bit-error-rate performance of 50dB-gain EDFA and 65dB-gain two-pump FOPA for the two different PSK formats. The optical spectra belong to the RZ-DPSK two-pump FOPA at input signal power of -43dBm (left) and -32dBm (right). Acronyms: P1 – pump 1; P2 – pump 2; S – signal..............74

Figure 5.11: (a) Measured optical spectra for RZ-DPSK two-pump FOPA at input signal power of -35dBm; the optical spectrum analyzer resolution bandwidth was 0.2nm. Acronyms: P1 – C-band pump, P2 – L-band pump, S – signal; (b) Measured FOPA gain spectrum. 75

Figure 5.12: BER performance of the 50dB-gain two-pump FOPA and 50dB-gain EDFA for RZ-DPSK modulation format. 77

Figure 5.13: Experimental setup a distant continuous-wave wavelength converter; Inset: Optical spectrum following wavelength conversion of 1212nm-signal to 2210nm-idler using a pump positioned at 1566 nm; Acronyms: EDFA – Erbium-doped fiber amplifier, LPF – low-pass (RF) filter, PM – phase modulator, OBPF – optical band-pass filter. 78

Figure 5.14: Measured NIR-to-SWIR conversion gain spectrum with different pump wavelength positioning for an NIR signal tuned from 1260 to 1360 nm in steps of 0.2 nm. 80

Figure 5.15: (a) Measured NIR-to-SWIR conversion gain for different pump wavelength detuning and fixed signal wavelength of 1212 nm; (b) Optical spectra of the SWIR idler at several pump wavelength positions. 80

Figure 6.1: Carbon-dioxide and water absorption spectra taken from HITRAN2008 database...84

Figure 6.2: Experimental setup depicting (top) the parametric SWIR transmitter; (bottom left) the optical spectrum following NIR-to-SWIR conversion in HNLF; (bottom right) the optical spectrum following rejection of pump, signal, and excess AQN; Acronyms: AM – amplitude modulator, EDFA – Erbium doped fiber amplifier, DWDM – dense wavelength division multiplexer, VOA – variable optical attenuator, Rx – optical receiver. 86

Figure 6.3: (a) Measured conversion gain spectra for several different pump wavelength positions; (b) Measured conversion gain spectrum with pump wavelength optimized for peak conversion gain at 2051 nm. 87

Figure 6.4: (a) Measured idler optical spectra at four different positions; (b) CO_2 absorption data obtained from HITRAN2008 database; (c) Measured idler pulses corresponding to the four different idler wavelengths shown in (a). 88

Figure 6.5: Measured amplified quantum noise spectra for high-ZDW-fluctuation (HNLF-1) and low-ZDW-fluctuation (HNLF-2) 7m-long nonlinear fibers at two different pump power levels. 90

Figure 6.6: (a) Pump power dependence of AQN spectra of high-ZDW-variation HNLF (HNLF-1 in Figure 6.5); (b) Pump polarization dependence of AQN spectra due to HNLF-1’s inherent birefringence..91

Figure 6.7: Experimental setup depicting the parametric SWIR receiver; (top left) optical transfer function of the two 1310-nm fiber Bragg gratings (FBGs); (top right) converted/amplified 1310-nm pulse waveform; (bottom left)

optical spectrum of 2015-nm idler generated via a parametric transmitter described in Section 6.2; (bottom right) the optical spectrum following SWIR-to-NIR conversion in HNLF; Acronyms: AM – amplitude modulator, EDFA – Erbium doped fiber amplifier, DWDM – dense wavelength division multiplexer, VOA – variable optical attenuator. 92

Figure 6.8: Measured OSNR and ESNR of converted 1310-nm idler vs. input signal power of 2015-nm signal..93

Figure 7.1: HNLF attenuation vs. wavelength...97

Figure 7.2: Attenuation of single-mode ZBLAN fiber..99

Figure 7.3: Nonlinear vs. linear refractive index of selected MWIR transmitting glasses at the wavelength of 1550nm...100

Figure 7.4: Material dispersion of selected MWIR transmitting glasses and silica........102

Figure 7.5: Calculated (a) dispersion, and (b) effective modal area of a single-mode ZBLAN fiber with simple (SMF-type) doping profile. 104

Figure 7.6: (a) Phase-matched signal/idler wavelengths, and (b) pump/signal phase-matching contours for single-mode tellurite fiber....................................105

Figure 7.7: (a) Phase-matched signal/idler wavelengths, and (b) pump/signal phase-matching contours for single-mode ZBLAN fiber...................................105

Figure 7.8: Calculated signal-to-idler conversion efficiency in single-mode ZBLAN fiber for pump wavelength position of 1530 nm..................................106

Figure A.1: Schematic for semi-analytical model of PM-to-AM in optical fiber. 108

Figure B.1: Experimental setup for HNLF Raman gain/loss measurement; Acronyms: OSA – optical spectrum analyzer, PM – polarization-maintaining, PC – polarization controller. 111

Figure B.2: Measured Raman gain/loss. 112

Figure B.3: HNLF Raman gain/loss asymmetry..113

Figure B.4: Raman gain spectra of measured HNLF and scaled SMF. 114

List of Tables

Table 1.1: Performance comparison of selected SWIR transmitter technologies. 4

Table 1.2: Selected SWIR detector technologies. 6

Table 3.1: FOPA simulation/experimental parameters 37

Table 5.1: Simulation parameters for the two HNLF spools. 62

Table 7.1: Candidate non-silica glasses for MWIR light generation. 99

Acknowledgements

Chapter 3, in full, is a reprint of the material as it appears in “Phase noise in fiber-optic parametric amplifiers and converters and its impact on sensing and communication systems,” by S. Moro, A. Peric N. Alic, and S. Radic, Optics Express, Vol. 18, 2009. The dissertation author was the primary investigator and author of this paper.

Vita

2005	B.S. in Electrical Engineering, University of California – San Diego, Department of Electrical and Computer Engineering.
2007	M.S. in Applied Physics - Photonics, University of California – San Diego, Department of Electrical and Computer Engineering.
2011	Ph.D. in Applied Physics - Photonics, University of California – San Diego, Department of Electrical and Computer Engineering.

ABSTRACT OF THE DISSERTATION

Parametrically-aided sensing in the short-wave infrared frequency band and beyond

by

Slaven Moro

Doctor of Philosophy in Electrical Engineering (Photonics)

University of California, San Diego, 2011

Professor Stojan Radic, Chair

In this dissertation, wideband frequency-mixing parametric processes in nonlinear light guides are engineered to enable implementation of mature near-infrared wavelength band technology in the spectrally significant short-wave infrared band. An ultracompact, powerful, widely-tunable, all-fiber laser transmitter is demonstrated in silica-based mixer and used for spectral fingerprinting of carbon dioxide. Furthermore, highly-sensitive optically-preamplified receiver is demonstrated, providing high-gain and low-noise figure operation in arbitrary spectral windows of the short-wave infrared band. Lastly, candidate non-silica platforms for extending the mixer operation to the mid-infrared spectral regions are rigorously analyzed.

1. Introduction

1.1 Optical remote sensing in the short-wave infrared frequency band

Over the short-wave infrared (SWIR) spectrum, which is typically defined as spanning from 1700 to 2500 nm, a variety of molecular gases and environmental pollutants exhibit strong well-defined absorption features [1]. To detect their unique “fingerprints” requires remote sensing in the SWIR band via a LIght Detection And Ranging (LIDAR) technique which must itself rely on high-power, high-frequency-fidelity, tunable laser sources in conjunction with low-noise photodetectors [2, 3]. Figure 1.1 illustrates a typical LIDAR system architecture with separate receiver and transmitter sections. In the simplest transceiver implementation, the transmitting laser pulse is absorbed by the sensed molecule, causing a reduction in reflected pulse power measured by the receiver. The time-of-flight is an accurate indicator of the distance at which the sensed chemical is present, while the amount of reflected pulse attenuation is used to estimate the concentration of the molecular species.

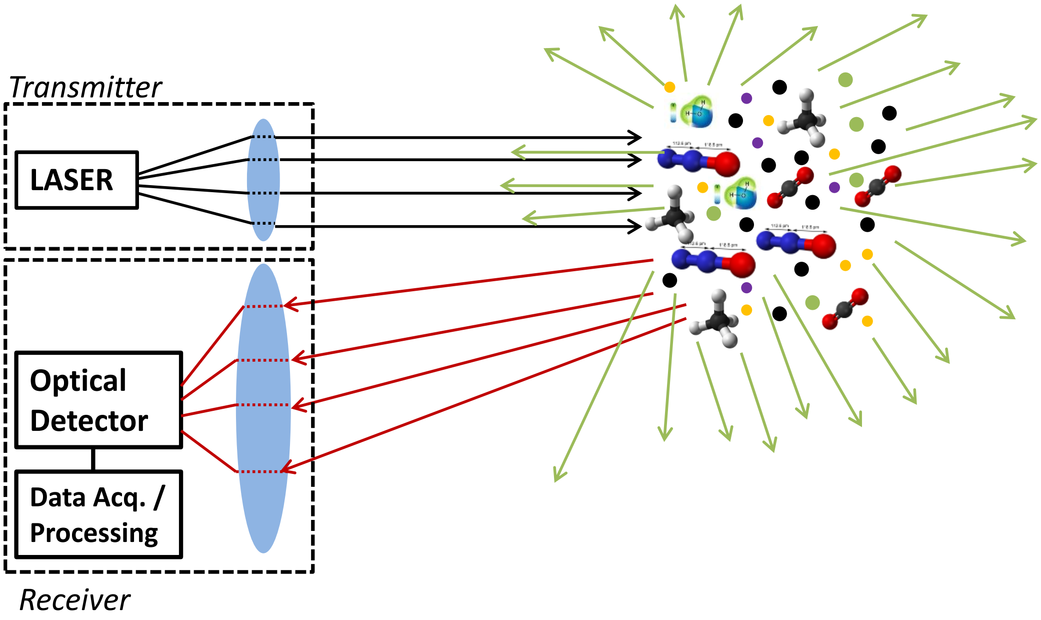

Figure 1.1: Typical LIDAR system architecture.

The accuracy and resolution of remote sensing measurements is strongly dependent upon absorption line strengths of the sensed chemical species. In addition, high contrast against the ubiquitous water vapor is desired in order to extend the sensing range. To exemplify, the absorption line strengths of two of the most common green house gases (carbon-dioxide and methane) are depicted in Figure 1.2. We note that the absorption in the SWIR band is several orders of magnitude higher compared to the near-infrared (NIR) wavelength band. The water contrast ratio is also higher, allowing for increased sensing range. Not surprisingly, the mid-wave infrared (MWIR) band is spectrally superior to both NIR and SWIR, with 3-5μm spectral band often being referred to as the “molecular fingerprint region [1].”

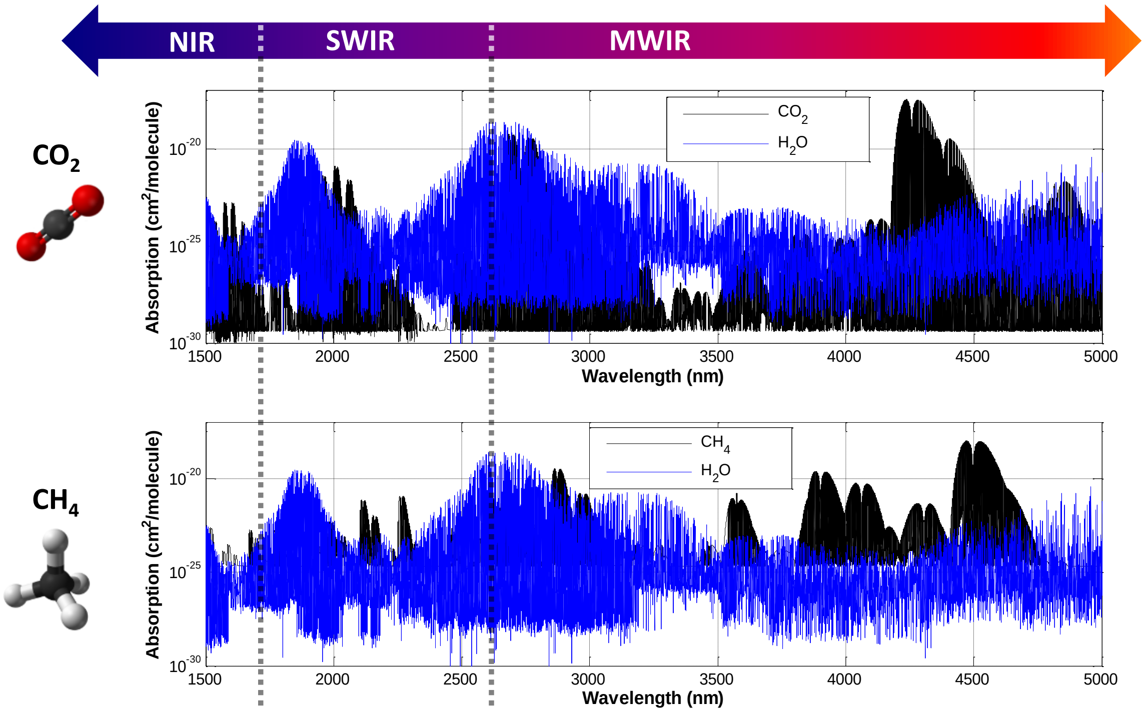

Figure 1.2: Absorption line strengths of CO_2 and CH_4 (black) with superimposed H_2O (blue).

1.2 Overview of existing SWIR technologies

In LIDAR systems, the amount of collected power at the receiver is inversely proportional to the square of the distance from the sensed target. The highly desirable extension of the sensing range therefore places great requirements on the transmitter power and/or receiver sensitivity. Remote sensing in the short-wave infrared band continues to be challenged by the lack of readily available sources and detectors that meet the general requirements for LIDAR systems in terms of performance, durability, size, weight, power consumption, and most perhaps importantly – affordability. The typical performance characteristics of current SWIR source technologies are summarized in Table 1.1. With exception of GaSb-based distributed feedback lasers (DFBs) and vertical cavity surface emitting lasers (VCSELs), the sources rely on external cavity (EC) tuning in order to achieve broadband wavelength tunability. As a result, they are subject to cavity stability issues that require frequent maintenance procedures. The mode-hop-free tuning range of such devices is inherently limited and tends to not be reported by the investigators (see Table 1.1).

Table 1.1: Performance comparison of selected SWIR transmitter technologies.

SWIR source	**Tuning range (μm)**	**Mode-hop-free**	**Power**	**Linewidth**	**Ref.**
OPO (MgO:PPLN)	2.2-2.5	100GHz	1-3W (CW)	1MHz	4, 5
	2.5-3.2		2-3W (CW)		
Cr^{2+}:ZnS	1.98-3.00	n/a	>100mW (CW)	<10GHz	6
Cr^{2+}:ZnSe	1.99-3.30	n/a	>70mW (CW)	<10GHz	6
	2.46	n/a	10mW (CW)	20MHz	7
Tm^{3+}:SiO$_2$	1.947-2.108	n/a	>2W (CW)	0.3nm	8
	1.9-2.0 (fixed)	n/a	<500W (pulsed)	<200MHz	9
GaSb-based VCSELs	2.35	10nm	600μW (CW)	100MHz	10, 11
GaSb-based ECLs	2.23-2.39	n/a	9mW (CW)	GHz (est)	12
	2.066-2.218	n/a	10mW (CW)		13
GaSb-based DFBs	2.05, 2.33	200GHz	3mW (CW)	10MHz (est)	14
Er^{3+}: ZBLAN	2.7, 3.45	n/a	8mW (CW), 8W (pul)	MHz	1
Tm^{3+}: ZBLAN	2.3	n/a	10mW (CW)		
Ho^{3+}: ZBLAN	2.90, 3.22	n/a	11mW (CW), 2.5W (pul)		

The DFBs and VCSELs typically allow a few nanometers of mode-hop-free thermal wavelength tuning combined with high spectral purity (narrow linewidth); however, their output powers are limited to a few miliwatts. In contrast, rare-earth-doped silica and ZBLAN fibers are capable of providing both power and linewidth but are spectrally limited by the energy structure of the doped medium. The external-cavity oscillators based on Chromium-doped ZnS and ZnSe provide superior tuning range while undesirably trading power for linewidth.

The state-of-the-art SWIR sources that have been utilized in LIDAR systems to date are custom-made crystal-based optical parametric oscillators (OPOs), providing multiple Watts of output power, wideband tunability, and typical linewidths of several MHz [15, 16]. To their credit, these OPOs allow broadband tunability (hundreds of nanometers); however, their mode-hop-free tuning range is limited to approximately 100 GHz (order of 1 nm) [4], which precludes their use in sensitive spectroscopy applications. Another practical limitation to the widespread use of traditional OPOs for this application is their construction. OPOs rely on free-space optical elements and as such they are highly sensitive to thermal and vibration perturbations; their performance when fielded is depreciated over that which can be demonstrated in a laboratory environment.

In addition to issues associated with optical sources, SWIR-band LIDAR is impaired by unavailability of sensitive, high-bandwidth photodetectors. Table 1.2 summarizes the current SWIR detector platforms in terms of wavelength coverage, detector responsivity, bandwidth, noise-equivalent power (NEP), and dark current. When operating at room temperatures, the most promising detector technology in the SWIR band has been shown to be extended-band InGaAs [18]. Thermoelectric cooling (-20ºC typically) drastically improves the performance of AlGaAsSb/InGaAsSb quaternary hybrid phototransistors (HPTs), outperforming extended-band InGaAs under such operating conditions [19]. Still the performance of devices based on both aforementioned technologies is frustrated by high thermal and dark current noise due to the reduced semiconductor bandgap at these wavelengths as well as high impurity and defect concentrations.

Table 1.2: Selected SWIR detector technologies.

SWIR detector	**Manuf.**	**Wav. range (µm)**	**Resp.**	**Band-width**	**NEP (pW/ √Hz)**	**Dark current**	**Ref.**
InGaAs p-i-n	EOT	0.83-2.10	1.60A/W	10GHz	<2	<10µA	17
InGaAs p-i-n	Hamamatsu	0.90-2.30	1.00A/W	100MHz	0.73	200nA	18
InGaAs + TIA	Discovery	1.20-2.20	670V/W	6GHz	9.9	n/a	20
AlGaAsSb/InGaAsSb HPTs	NASA	1.00-2.40	1000A/W	100MHz	0.13	n/a	21
InGaAs p-i-n (NIR)	EOT	1.00-1.65	0.88A/W	10GHz	<0.04	<3nA	22

The technologically advanced NIR photodetector technology is not subject to fundamental material issues that plague its SWIR counterpart. The last row in Table 1.2 depicts typical performance for an InGaAs p-i-n photodiode. The NEP and dark current are at least two orders of magnitude lower than the extended-band SWIR version of the same material platform (first row in Table 1.2). One method of negating the influence of dark current noise and increasing the photodetector sensitivity includes integration of a trans-impedance amplifier (TIA) with the SWIR photodiode [20]; the noise performance in that case is limited by the amplifier thermal noise. The less noisy (and therefore preferred) approach involves avalanche multiplication of electrons as in the AlGaAsSb/InGaAsSb HPTs [21]. While both approaches improve detection sensitivity over the simple p-i-n photodetector by approximately 10 dB, they are penalized by poor linearity, small dynamic range, and reduced bandwidth, as well as high susceptibility to electrical damage at high input powers [23].

1.3 Porting NIR technology to SWIR via parametric amplification/conversion

Sources and detectors available in the SWIR band contrast sharply with their near-infrared (NIR) (800-1700 nm) counterparts which have benefited from years of intense commercial development predominantly driven by the optical telecommunications industry. As a result, mode-hop-free, widely-tunable, narrow-linewidth NIR sources are readily available and relatively inexpensive. Furthermore, the photodetection sensitivity in the NIR band can be improved by an order of magnitude over avalanche photodiode (APD) platform via optical pre-amplification [23]. Here the combination of rare-earth doped fiber amplifiers (EDFAs & YDFAs) and semiconductor optical amplifiers (SOAs) provides for more than 30 dB of optical gain over the entire NIR spectrum with routinely reproducible low noise figures in the 3-5 dB range [24, 25].

From the above discussion, it is clear that a significant gap exists between the technologically developed NIR band and the spectrally important SWIR band. It is also questionable whether heavy investment in research and development of SWIR technology could ever result in NIR-like performance as this endeavor is challenged not only by difficult engineering problems but also fundamental physics. Hence, rather than insisting on costly technological advancement in the SWIR band, developing a platform capable of porting the existing NIR technology to the SWIR band is perhaps a far more sensible solution. The required nonlinear optical platform would need to provide an efficient, cavity-less approach to mixing of NIR frequencies that would generate the SWIR source free of the aforementioned cavity-related issues discussed in the previous section. On the receiving end, the ability to convert from SWIR to NIR in essentially noise-free manner with at least transparency (0 dB conversion gains) is required in order to take advantage of the superior NIR detectors. However, it is much more desirable to have the conversion accompanied by low-noise optical gain (30 dB or larger), which would result in detection sensitivities comparable to optically-preamplified NIR receivers.

The single-pass transmitter assembly and high-gain SWIR receiver construction require long nonlinear interaction lengths. Thus, the guided-wave nature of parametric amplification/conversion in $\chi^{(3)}$ (Kerr) nonlinear media [26] enables this platform as an excellent candidate for porting the NIR technology to the poorly-developed SWIR band, as illustrated in Figure 1.3. The main area of research to be presented in this dissertation is concerned with engineering of the parametric gain, as well as understanding and mitigation of encountered impairments, necessary for the construction of the parametric transmitter and the parametrically-preamplified receiver for SWIR-band LIDAR. All of the discussed experimental work was performed utilizing the silica-based dispersion-engineered highly-nonlinear fiber (HNLF) devices [27] due to their technological maturity. Nonetheless, the presented theoretical investigations are applicable to parametric processes taking place in any third-order nonlinear media (e.g. Silicon waveguides, chalcogenide glass fibers, photonic crystal fibers, etc.).

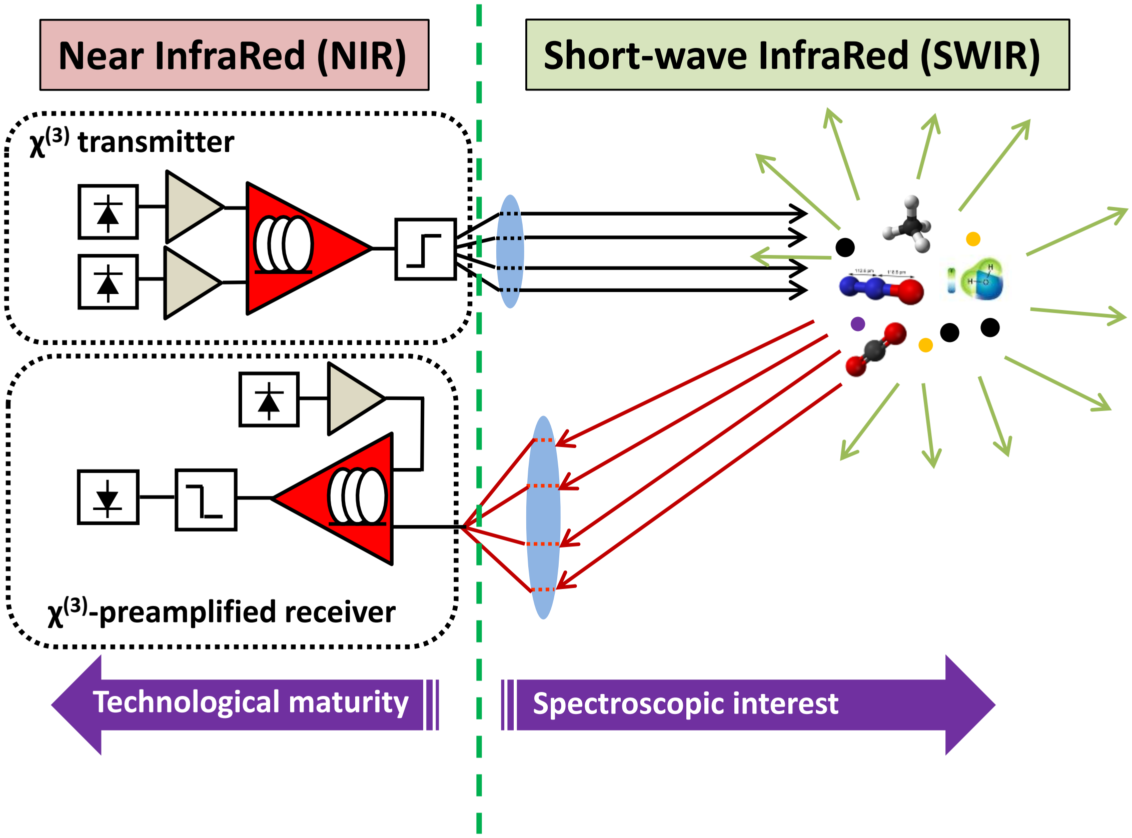

Figure 1.3: Illustration of $\chi^{(3)}$ nonlinear media as a platform for bridging the gap between technologically-mature NIR band and spectroscopic SWIR band.

1.4 Thesis organization

The dissertation is organized as follows: The physical basis of parametric amplification/conversion Kerr nonlinear media is examined in Chapter 2. Simple expressions for phase matching conditions and parametric gain are presented for both one-pump and two-pump parametric amplifiers/converters. Further, candidate Kerr nonlinear platforms for parametric gain synthesis in the SWIR band are discussed. The benefits and shortcomings of platforms exhibiting positive/negative fourth-order dispersion coefficients are also examined. The noise associated with parametric processes is theoretically and experimentally investigated in Chapter 3. In particular, all phase noise sources and their relative contributions are presented and rigorously analyzed. In Chapter 4, the distinction between nonlinear phase noise and nonlinear frequency chirping is theoretically investigated and experimentally verified, leading to interesting conclusions regarding the influence of spectral content of pump amplitude noise on the frequency noise of amplified and newly-generated (converted) optical waves.

Chapter 5 is primarily concerned with parametric gain synthesis in the continuous-wave regime. The impact of waveguide dispersion fluctuations and presence of Raman gain on engineering of high and spectrally flat parametric gain in the NIR wavelength band is investigated in both one-pump and two-pump experimental architectures. The challenging NIR-to-SWIR conversion is presented and practical limitations of distant continuous-wave conversion are discussed. Chapter 6, on the other hand, focuses on parametric gain synthesis in the pulsed regime. The construction and characterization of widely-tunable parametric transmitter in the SWIR band used to detect the presence of trace carbon-dioxide will be introduced. The assembly and performance evaluation of highly-sensitive parametrically-preamplified SWIR receiver will also be presented in this Chapter.

In Chapter 7, mixing in non-silica glass fibers as a platform for accessing MWIR frequency band is investigated semi-analytically and via numerical simulation. More specifically, parametric mixing in waveguides dominated by material dispersion will be proposed as a method of nullifying the detrimental effects caused by spatially fluctuating waveguide dispersion. The potential of Telluride-based material-dispersion-dominated single-mode fiber platform for mixing of wavelength bands associated with Erbium- (1530-1620 nm) and Thulium-doped (1870-2050 nm) silica will be investigated. Finally, widely-tunable MWIR parametric source synthesis utilizing ZBLAN (fluoride-based) single-mode fiber for highly-desirable mixing of Ytterbium (1020-1100 nm) and Erbium (1530-1620 nm) bands will be proposed.

2. Parametric amplification/conversion in $\chi^{(3)}$ nonlinear media

Over the last decade or so, parametric amplification and wavelength conversion in waveguides characterized by third-order optical nonlinearity has been witnessing a growing interest from the research community [26, 28-30]. Some of the applications and record demonstrations that have emerged include: real-time processing of arbitrary optical signals via Multicast Parametric Synchronous Sampling (MPASS) technique at 320 Gb/s data rates [31, 32], equivalent-time sampling of optical waveforms with 100s of GHz bandwidth [33], continuously-tunable wavelength transparent optical delay in the microsecond range [34], ultra-low-power all-optical switching [35, 36], optical pulse compression [37], ultrafast wideband laser source tuning [38], octave-spanning coherent supercontinuum generation [39], all-optical amplitude and phase regeneration [40, 41], translation of amplitude- and phase-modulated signals from near-infrared to visible band [42, 43], all-fiber optical parametric oscillator in the short-wave infrared [44, 45], wavelength conversion from near-infrared to short-wave infrared band [46], etc.

The fundamental principles of parametric processes in $\chi^{(3)}$ nonlinear media will be reviewed in Sec. 2.1. The one-pump and two-pump parametric architectures will be introduced in Sec 2.2. Furthermore, various platforms for wide-band nonlinear frequency conversion will be reviewed. The intent is to justify the silica HNLF as a platform of choice for NIR-to-SWIR wavelength conversion and SWIR gain synthesis. Lastly, the phase matching considerations for frequency mixing in nonlinear fibers with positive/negative fourth-order dispersion coefficients will be discussed.

2.1 Fundamental principles

Nonlinear optical phenomena occur when the response of the material system to an applied optical field is nonlinear with respect to the strength of the field. Physically, the material response is characterized by perturbation of valence electrons by the electric-field component of the radiation. The dielectric response, for both amorphous and crystalline insulators and semiconductors, is dominated by either resonant or nonresonant processes. The resonant processes involve electronic transitions between occupied and vacant energy levels. The nonresonant processes, on the other hand, physically involve only distortions of occupied electronic orbitals and are theoretically described as “virtual” transitions between energy levels. According to Heisenberg’s uncertainty principle, the excited electrons can reside in a virtual level only for the time duration proportional to $\hbar/\Delta \mathrm{E}$, where $\Delta \mathrm{E}$ is the energy difference between the virtual level and the closest real level. The processes that do transfer population from one real level to another, such as the resonant nonlinear processes, are known as *nonparametric processes*. Conversely, the processes in which the initial and final quantum-mechanical states of the system are identical, as in nonresonant nonlinear processes, have come to be known as *parametric processes*. In parametric processes the photon energy is conserved, whereas it is transferred to the medium in their nonparametric counterpart. Hence, parametric processes are always described by the real part of dielectric susceptibility and affect the real part of the refractive index. Some examples of nonparametric processes are two-photon absorption (2PA), three-photon absorption (3PA), saturable absorption, stimulated Raman scattering (SRS), and stimulated Brillouin scattering (SBS). The second-harmonic generation (SHG), third-harmonic generation (THG), sum-frequency generation (SFG), difference-frequency generation (DFG), four-wave mixing (FWM), phase conjugation (PC), parametric amplification (PA), wavelength conversion (WC), and modulation instability (MI) are all examples of parametric processes.

Shortly after the demonstration of the first working laser by Maiman in 1960, Franken, et al. experimentally observed the first nonlinear frequency conversion (SHG) in crystalline quartz [47]. Immediately following, the theory of light wave interaction in second- and third-order nonlinear media was developed [48]. As it was pointed out, the material response to the applied electric field is confined to electrons as the nuclei are too massive to respond to the high optical frequencies. The field causes a displacement of valence electrons with respect to their anionic cores. The resulting dipole per unit volume (i.e. polarization) of the material system is given by [49]

$$P = \varepsilon_0 \left(\chi^{(1)} E + \chi^{(2)} EE + \chi^{(3)} EEE + ... \right) \tag{3.1}$$

where ε_0 is the dielectric constant, *E* is the optical frequency electric field, $\chi^{(1)}$ is the linear susceptibility, and $\chi^{(2)}$, $\chi^{(3)}$, and so on are the nonlinear susceptibilities. The first term is linear in *E* and defines the linear index of refraction n_0. The higher order terms physically reveal the degree of aharmonicity possessed by the natural motion of electrons about the nuclei. Therefore, one can expect materials with a large number of loosely bound valence electrons to have a large nonlinear susceptibility, which in turn would be accompanied by a large linear index of refraction. The correlation between linear and nonlinear index of refraction is further discussed in Chapter 7.

In quasi-isotropic materials considered in this work, such as optical glasses used for fibers, the spatial inversion symmetry limits the nonlinear response to only odd orders in *E* [49]. We restrict ourselves to third-order susceptibility and express the refractive index in the presence of this type of nonlinearity as $n = n_0 + n_2 I$, where $n_2 = 3\chi_{\mathrm{Re}}{}^{(3)} \big/ (4c\varepsilon_0 n_0{}^2)$ is the third-order (Kerr) nonlinear index, *I* is the optical intensity, and $\chi^{(3)} = \chi_{\mathrm{Re}}{}^{(3)} + j\chi_{\mathrm{Im}}{}^{(3)}$ is the complex third-order susceptibility with $\chi_{\mathrm{Im}}{}^{(3)}$ describing the Raman response. The imaginary part of the susceptibility is frequency-dependent as it describes the frequency dependent Raman gain and the associated Raman phase shift. However, we consider $\chi_{\mathrm{Re}}{}^{(3)}$ being independent of frequency, because we are operating the nonlinear mixer away from the natural material resonances.

Before proceeding to more detailed analysis, we want to develop an understanding of the fundamental physics governing the nonlinear interaction. When two weak optical fields at two different frequencies are applied to the nonlinear dielectric, an oscillating dipole (consisting of the massive nucleus and perturbed valance electron) at the beat frequency will be created at every atomic site. As the power of one or both fields is increased, the oscillating dipole will stop responding to the beat field in a linear fashion. As the dipole's motion is "clamped" in the time domain, new spectral components of the radiation are naturally created in the frequency domain. Since any material sample will contain a vast number of atomic dipoles, the relative phasing of the dipoles will determine what amount of energy will be converted to the newly generated optical field component. If the so-called *phase-matching condition* is met, the system will act as a phased array of dipoles and hence an efficient frequency converter. The phase-matching condition is closely tied to the dispersive properties of the nonlinear mixing platform.

In third-order nonlinear media, the process responsible for creation of new frequencies is often referred to as four-photon-mixing (FPM) or four-wave-mixing (FPM). It was first observed by Stolen et al. in multimode silica waveguides [50]. One year later, the same group observed the FPM process accompanied by gain, as the effective phase-matching lengths were for different modes of the guide were improved from centimeters to meters [51]. The FPM process accompanied by gain was subsequently termed *parametric amplification* and expressions for gain were rigorously derived [52]. The authors in [52] considered a powerful pump wave and a weak signal wave at the input of the nonlinear silica fiber. Mediated by the Kerr nonlinearity, the two pump photons are annihilated and donated to the amplified signal wave and the newly generated “idler” wave. Since the two pump photons are identical (or very nearly identical) in frequency, this above process is termed degenerate four-wave-mixing (DFWM). The created photon with frequency lower than the pump wave contributes to the so-called Stokes wave, while the high frequency photon adds to the anti-Stokes wave.

The amplification/generation of Stokes and anti-Stokes wave can also be intuitively explained as a diffraction-like process. The powerful pump wave and weak frequency-detuned signal wave interfere and modulate the light intensity with the beat frequency. This in turn modulates the refractive index via the Kerr nonlinear effect, generating an index grating which moves at the velocity equal to the difference of the group velocities of the two waves [53]. The index grating diffracts pump light to the idler frequency. The pump-idler beating, subsequently creates another grating which diffracts pump light to the signal frequency and results in signal amplification. The idler generation and signal amplification are therefore strongly coupled processes. Any excess loss (e.g. material absorption) at the idler frequency, for example, would also affect the amount of signal amplification and vice versa. This is an important consideration in designing $\chi^{(3)}$-based wideband wavelength converters and amplifiers.

The FWM process in Kerr nonlinear media need not involve the weak coherent signal wave. The inherently present zero-point vacuum field fluctuations can also seed the parametric amplification/conversion process. If the group dispersion and nonlinear frequency shift have opposite signs, the modulation of amplitude and frequency of the pump wave grows exponentially and the process is referred to as modulation instability (MI) [54]. Hasegawa and Brinkman suggested using MI to create tunable coherent sources in 1980 [55]; MI in optical fibers was first observed by Tai, et al. in 1986 [56]. In the frequency domain, MI manifests itself as amplification of broadband quantum noise (QN) which is phase-matched to the pump. Intuitively however, MI is easier to understand in the time domain. Namely, the intensity of a noiseless pump wave is still modulated (in the time domain) by the presence of wideband quantum noise. As a result, the ultrafast intensity fluctuations are converted into phase fluctuations in an instantaneous manner; the Kerr nonlinearity in fused silica is characterized by sub-10fs response time for electronically-dominated nonlinearity subject to a non-resonant light field [57]. During propagation, the dispersion can either enhance or suppress the nonlinear phase fluctuations [58]. In case of MI, the dispersion converts the noise-induced chirp into intensity fluctuations of the pump wave. The increased intensity fluctuations of the pump wave cause further degradation of the pump phase via Kerr nonlinearity and therefore further increase in intensity fluctuations, and so on. This positive-feedback-type effect is thus responsible for the exponential increase of the pump amplitude and frequency instability.

2.2 Degenerate and non-degenerate four-wave-mixing interaction

The nonlinear mixing interaction of optical waves in third-order nonlinear media need not involve four distinct optical waves. Two pump waves of the same frequency may interact with a frequency-detuned signal to produce the new (idler) wave. This process is referred to as degenerate four-wave-mixing (DFWM) or three-wave-mixing (TWM) as it involves only three distinct waves [59]. In the case when all four interacting waves have distinct frequencies, the process is referred to as non-degenerate four-wave-mixing (NDFWM).

2.2.1 One-pump parametric amplifier/converter

The one-pump parametric amplifier/converter, illustrated in Figure 2.1, is a perfect example of DFWM process. Two pump photons of frequency ω_1 are annihilated via MI and a Stokes and anti-Stokes photon are created at ω_{1-} and ω_{1+} respectively. Since the signal can be injected at either the Stokes or the anti-Stokes side of the pump, we will use ω_s for signal frequency, ω_i for idler frequency, and ω_p for pump frequency from this point on.

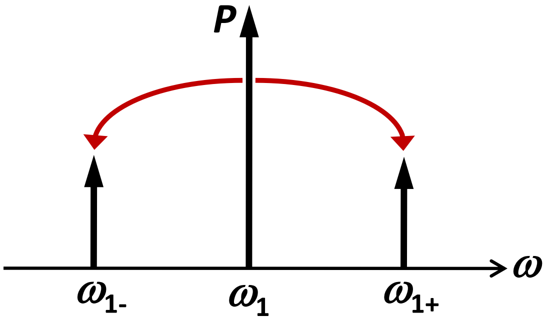

Figure 2.1: Schematic of a one-pump parametric process.

The amplification/conversion efficiency depends critically on the linear phase mismatch among the propagating waves given by

$$\Delta k_L = 2k_p - k_s - k_i = \beta_2 \left(\omega_s - \omega_p\right)^2 + \frac{\beta_4}{12}\left(\omega_s - \omega_p\right)^4 + \ldots \tag{3.2}$$

In the last equality, Taylor series expansion of the pump wave vector k_p about the pump frequency ω_p was performed. We note that only even orders of dispersion coefficients affect the phase-matching condition. The total phase mismatch includes both the linear and nonlinear part and is expressed as

$$\kappa = \Delta k_L + \Delta k_{NL} = \Delta k_L + 2\gamma P, \tag{3.3}$$

where $\gamma = \omega_p n_2 / cA_{eff}$, A_{eff} is the pump effective modal area, and P is the pump power. In order to arrive at a simple expression for parametric gain, we choose to neglect: polarization effects (i.e. we consider all interacting waves to be co-polarized), Raman response, pump depletion (i.e. small-signal behavior of the amplifier is of interest) and guiding loss. Defining the exponential gain constant as

$$g = \sqrt{(\gamma P)^2 - (\kappa/2)^2}, \tag{3.4}$$

the signal parametric gain is given by [52]

$$G_s = 1 + \left(\frac{\gamma P}{g}\right)^2 \sinh^2(gL). \tag{3.5}$$

In the case of perfect phase-matching ($\kappa = 0$), the expression for signal gain simplifies to $G_s = 1 + (1/4)e^{2\gamma PL}$. Meanwhile, the idler conversion gain is $G_i = G_s - 1$.

2.2.2 **Two-pump parametric amplifier/converter**

By introducing an additional pump wave to the parametric process, the FPM results in coupled interaction of four spectrally-distinct sidebands [60], as illustrated in Figure 2.2. First, each pump generates near sidebands via a DFWM process of MI: $2\omega_{1,2} \rightarrow \omega_{1-,2-} + \omega_{1+,2+}$. Second, the NDFWM process of phase conjugation (PC) further transfers power from the pumps to the four sidebands: $\omega_1 + \omega_2 \rightarrow \omega_{1-} + \omega_{2+}$ and $\omega_1 + \omega_2 \rightarrow \omega_{1+} + \omega_{2-}$. Finally, the NDFWM process of Bragg scattering (BS) enables stable photon exchanges: $\omega_1 + \omega_{2+} \rightarrow \omega_{1+} + \omega_2$ and $\omega_{1-} + \omega_2 \rightarrow \omega_1 + \omega_{2-}$.

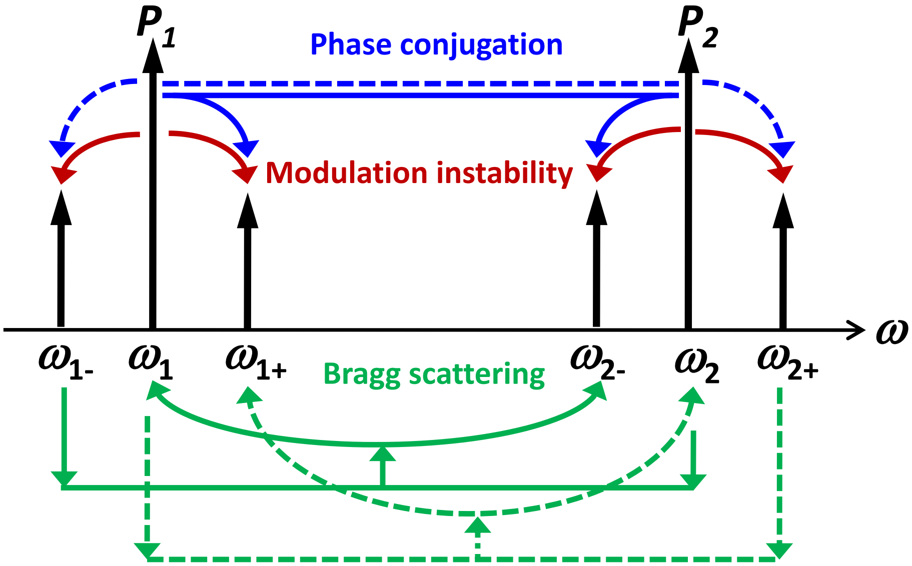

Figure 2.2: Schematic of a two-pump parametric process.

In order to synthesize wideband parametric gain in the two-pump architecture, the two pump waves are positioned nearly symmetrically about the zero-dispersion wavelength (ZDW) of the nonlinear medium. As a result, the MI process is spectrally limited to the vicinity of the pump wave. Since the BS interaction is at most unity [60], the two-pump parametric gain is dominated by the PC process. The linear phase mismatch due to the phase conjugation process is given by [60]

$$\Delta k_L = 2\sum_{m=1}^{\infty}\frac{\beta_{2n,c}}{(2n)!}\left[(\omega_s-\omega_c)^{2n}-{\omega_d}^{2n}\right], \tag{3.6}$$

where $\beta_{2n,c}$ is evaluated at $\omega_c=(\omega_1+\omega_2)/2$, and $\omega_d=(\omega_1-\omega_2)/2$. The total phase mismatch is then expressed as

$$\kappa=\frac{-{\lambda_c}^2}{2\pi c}S\left(\lambda_c-\lambda_o\right)\left[(\omega_s-\omega_c)^2-{\omega_d}^2\right]+\frac{\beta_4}{12}\left[(\omega_s-\omega_c)^4-{\omega_d}^4\right]+\gamma(P_1+P_2), \tag{3.7}$$

where $\lambda_c=2\pi c/\omega_c$, S is the dispersion slope, λ_0 is the zero-dispersion wavelength (ZDW), and β_4 is the fourth-order dispersion coefficient. Similar to the one-pump architecture, the exponential gain constant can be defined as

$$g=\sqrt{\left(2\gamma\sqrt{P_1P_2}\right)^2-\left(\frac{\kappa}{2}\right)^2}, \tag{3.8}$$

leading to a simple expression for the signal gain:

$$G_s=1+\left(\frac{2\gamma}{g}\right)^2 P_1P_2\sinh^2(gL). \tag{3.9}$$

As was the case in one-pump FOPAs, the signal-to-idler conversion gain is smaller than the signal gain by exactly unity.

The two-pump parametric architecture offers a number of advantages over its single-pumped counterpart. For example, a signal can be placed in any of the four interaction sidebands, resulting in creation of one spectrally-translated and two spectrally-mirrored (conjugated) idler bands [30]. MI, on the other hand, results in creation of only a single conjugated idler band. Next, the two-pump process can be used to eliminate the potentially detrimental idler spectral broadening, which is a consequence of pump phase modulation necessary for pump SBS suppression [61-63]. A polarization-insensitive parametric gain is also simply synthesized by utilizing cross-polarized pump waves [64], whereas more complicated techniques (e.g. ‘polarization diversity loop’) need to be employed in one-pump architectures [65]. Lastly, record equalized parametric gain response and signal multicasting bandwidths have been achieved via careful optimization of the two-pump parametric process [66-68].

2.2.3 **Overview of parametric mixing platforms**

The construction of high performance parametric devices requires a judicious choice of a material platform. Ideally, the material platform would provide both high nonlinearity and very precise control over dispersion properties, which would allow for synthesis of nearly arbitrary parametric gain profiles suited for particular application needs. To date, the most commonly investigated Kerr waveguide platforms include i) silica-based highly-nonlinear fiber (HNLF) [30], ii) Silicon waveguides [69], and iii) chalcogenide glass fibers [70].

Silicon and chalcogenide glasses have 2-3 orders of magnitude higher nonlinear refractive index (n_2) than silica; however, both platforms have significant practical drawbacks. In the case of Si, two-photon absorption of the NIR pump wave results in generation of free carriers which further absorb radiation via so-called ‘free carrier absorption’ [71]. As a result, it is impossible to synthesize CW or quasi-CW (ns or longer pulses) parametric gain necessary for parametric SWIR transmitter and receiver. Chalcogenide glasses, on the other hand, do not suffer from two-photon absorption in the NIR band. However, their high nonlinearity is fundamentally accompanied by very high dispersion (see Chapter 1 for further discussion), requiring utilization of complicated PCF-like structures for placement of ZDW in the NIR regime. The chalcogenide glasses are very brittle and fabrication of PCF-like structures with acceptable structural control continues to be a challenge [72].

Unlike chalcogenide glass fiber fabrication technology, the silica-based optical fiber platform has benefited from years of investment from the telecom industry in much the same way as the NIR source and detector technology. Increasing the core-cladding index contrast and reducing the core size (in comparison to standard single-mode fibers) provide for enhancement of nonlinearity as well as dispersion engineering via shaping of the doping profile [27].

2.2.4 Positive- vs. negative-β_4 highly-nonlinear fibers

Having chosen the silica-based highly nonlinear fiber (HNLF) platform in the one-pump architecture for synthesis of parametric gain in the SWIR band, we proceed by taking a closer look into the phase-matching considerations. The developed manufacturing process of silica fiber platform allows for fabrication of uniform, low-dispersion waveguide with both positive and negative fourth-order dispersion coefficients

[27]. In order to synthesize parametric gain in the SWIR band, the pump wave must be positioned in the *normal* dispersion regime ($D < 0$) for negative-β_4 HNLFs and in the *anomalous* dispersion regime ($D > 0$) for positive-β_4 HNLFs, as illustrated in Figure 2.3(a). Figure 2.3(b) shows the conversion gain as a function of wavelength for the two cases calculated using Equation (3.5) and some typical HNLF parameters. Note that the negative-β_4 HNLF provides exponential gain only in the SWIR band while its positive-β_4 counterpart possesses two phase-matched ($\kappa = 0$) regions. For our purposes, the presence of broadband parametric amplification in the NIR band is undesirable as the broadband amplified quantum noise (AQN) eventually depletes the pump wave and limits the amount of obtainable gain.

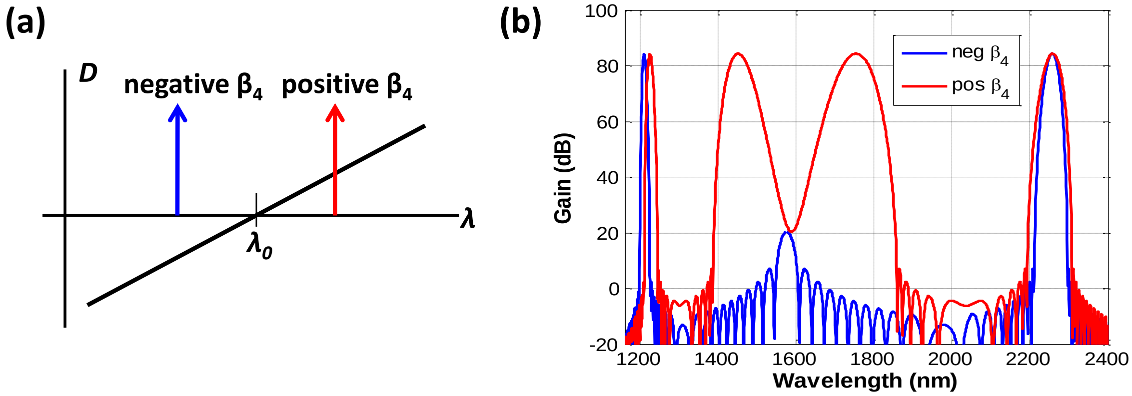

Figure 2.3: (a) Pump position for SWIR gain synthesis in positive- vs. negative-β_4 fibers; (b) Calculated conversion gain with parameters: $P = 100$ W, $\lambda_{p+} = 1587.8$ nm, $\lambda_{p-} = 1575.0$ nm, $L = 8$ m, $\gamma = 13\ \mathrm{W}^{-1}\mathrm{km}^{-1}$, $\lambda_0 = 1581$ nm, $S = 0.025\ \mathrm{ps/nm}^2$-km, and $\beta_4 = \pm 2\times 10^{-56}\ \mathrm{s}^4/\mathrm{m}$.

The spectral shape of parametric conversion gain depicted in Figure 2.3(b) can be seen from the plot of normalized linear phase mismatch, $\Delta k_L/2\gamma P$, versus the pump-signal separation, $\Delta\omega = \omega_s - \omega_p$ (see Figure 2.4). We consider significant parametric gain to exist in the range of $-4\gamma P < \Delta k_L < 0$, with $\Delta\omega_c$ representing the pump-signal frequency separation for the case of perfect phase matching ($\Delta k_L = -2\gamma P$) in the SWIR band and $\Delta\omega_1$ and $\Delta\omega_2$ defining the edges of the phase-matched region. Utilizing the Taylor series expansion for Δk_L from Equation (3.2), we arrive at the following expressions:

$$\Delta\omega_1 = \left(\frac{-12\beta_2}{\beta_4}\right)^{1/2}, \tag{3.10}$$

$$\Delta\omega_c = \left[\frac{-6\beta_2}{\beta_4}\left(1+\sqrt{1-\frac{2\gamma P}{3}\frac{\beta_4}{\beta_2^{\,2}}}\right)\right]^{1/2}, \tag{3.11}$$

$$\Delta\omega_2 = \left[\frac{-6\beta_2}{\beta_4}\left(1+\sqrt{1-\frac{4\gamma P}{3}\frac{\beta_4}{\beta_2^{\,2}}}\right)\right]^{1/2}. \tag{3.12}$$

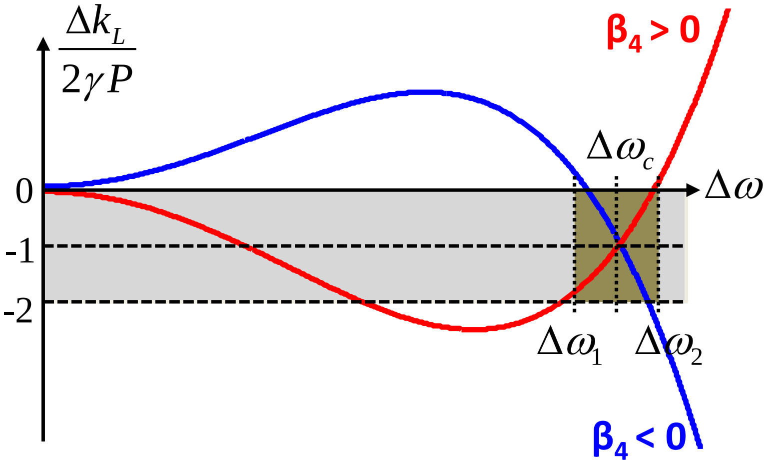

Figure 2.4: Normalized linear phase mismatch as a function of pump-signal (or equivalently pump-idler) separation.

Since $\Delta\omega_2 - \Delta\omega_1 \ll \Delta\omega_c$, it follows that $4\gamma P|\beta_4|/3\beta_2^{\,2} \ll 1$ and the binomial approximation can be used to get:

$$\Delta\omega_c = \left(\frac{-12\beta_2}{\beta_4}\right)^{1/2}\left(1-\frac{\gamma P}{12}\frac{\beta_4}{\beta_2^{\,2}}\right), \tag{3.13}$$

$$\Delta\omega_2 = \left(\frac{-12\beta_2}{\beta_4}\right)^{1/2}\left(1-\frac{\gamma P}{6}\frac{\beta_4}{\beta_2^{\,2}}\right). \tag{3.14}$$

Then, the width of the phase-matched SWIR band can be expressed as

$$\Delta\omega_{pm} = \left|\Delta\omega_1 - \Delta\omega_2\right| \simeq \left(\frac{-12\beta_2}{\beta_4}\right)^{1/2}\frac{\gamma P\left|\beta_4\right|}{6\beta_2^{\,2}} = \frac{\sqrt{3}\gamma P\left|\beta_4\right|^{1/2}}{3\left|\beta_2\right|^{3/2}}. \tag{3.15}$$

Equations (3.13) and (3.15) can further be combined to yield

$$\Delta\omega_{pm} \simeq \frac{2\left|\beta_4\right|}{\frac{12\beta_2^{\,2}}{\gamma P}-\beta_4}\Delta\omega_c, \tag{3.16}$$

where the explicit dependence of $\Delta\omega_{pm}$ on the sign of β_4 is evident. Namely, the SWIR phase-matched bandwidth is expected to be slightly larger for positive-β_4 HNLFs than their negative-β_4 counterparts; this is also shown graphically in Figure 2.3(b).

The width of the phase-matched SWIR region is critically dependent not only on the value of the fourth-order dispersion coefficient but also on the pump-signal detuning [73]. Making the approximation $\gamma P\left|\beta_4\right|/3\beta_2^{\,2} \approx 0$ in Equation (3.11), the second-order dispersion coefficient can be expressed in terms of the perfectly phase-matched pump-signal detuning:

$$\beta_2 \approx \frac{\Delta\omega_c^{\,2}\beta_4}{-12}. \tag{3.17}$$

Substituting (3.17) into (3.15) yields

$$\Delta\omega_{pm} \simeq \frac{24\gamma P}{\Delta\omega_c^{\,3}\left|\beta_4\right|}. \tag{3.18}$$

As the phase-matched bandwidth is inversely proportional to the cube of the pump-signal frequency separation, the synthesis of distant and wideband SWIR gain demands for very-low-β_4 mixing media, with high nonlinear coefficient γ, high pump powers P, and consequently shorter mixer lengths. To date, silica HNLF fabrication platform has been more successful in achieving low β_4 values in positive-β_4 fibers [27], making them the platform of choice for SWIR gain synthesis in this dissertation.

In addition to low fourth-order dispersion coefficient, SWIR gain synthesis is significantly affected by ZDW fluctuations of the HNLF. Assuming β_4 to be constant over a small pump detuning range of interest in our case, the phase-matched pump-signal detuning (Equation (3.11)) is a strong function of the second-order dispersion coefficient:

$$\beta_2(z) = \frac{-\lambda_p^{\ 2}}{2\pi c} S\left(\lambda_p - \lambda_0(z)\right). \tag{3.19}$$

The longitudinal dependence of ZDW of HNLF results in longitudinal fluctuations of pump/signal/idler phase mismatch, which lead to reduction in both peak gain and gain bandwidth achievable in the SWIR band. Employing typical experimental parameters such as those used in Figure 2.3(b), we calculate that 1 nm of ZDW fluctuation results in SWIR gain peak shift of over 80 nm! Assuring the ZDW fluctuations below 1nm is quite difficult in practice as it requires sub-molecular control of HNLF core radius [113]. In the SWIR gain synthesis described in this dissertation, the ZDW fluctuation limited the achievable SWIR gain to approximately 30 dB. This was sufficient for demonstration of widely-tunable parametric transmitter described in Section 6.2. However, the parametrically-preamplified receiver requires as much as 50 dB of gain, which is achievable in high-ZDW-fluctuation HNLF albeit with sacrificed performance (Section 6.3).

3. Noise in parametric processes

3.1 Introduction

The four-photon-mixing process is subject to inherent quantum-mechanical fluctuations (vacuum noise), which are coupled among the propagating waves via Kerr nonlinearity [74]. In the high gain limit, the resulting photon-number and field-quadrature fluctuations (in case of phase-insensitive parametric amplifiers) have been shown to be equivalent to those of $\chi^{(2)}$-based parametric processes (e.g. sum- and difference-frequency generation) as well as inverted-population (linear) optical amplifiers such as Erbium-doped fiber amplifiers (EDFAs) [74, 75]. In addition to the inherent quantum noise, the ultrafast nature of third-order (Kerr) optical nonlinearity in silica is responsible for transferring pump amplitude and phase fluctuations to the signal and idler wave in a near instantaneous manner.

The pump amplitude fluctuations are typically a combination of pump laser relative intensity noise (RIN), and amplifier noise added during pump wave amplification, with the latter being dominant in most practical situations [76]. The spectral dependence of the signal and the idler amplitude noise in a one-pump FOPAs has been analyzed recently and shown to include predictable contributions from processes such as the amplified quantum noise (AQN), pump transferred noise (PTN), and Raman phonon seeded excess noise [77]. It was found that AQN dominates the noise performance at input signal levels below -30dBm, whereas PTN tends to limit the signal and idler amplitude fidelity at higher input powers. The PTN originates from the FOPA's inherent gain sensitivity to instantaneous pump power, causing the amplitudes of the signals positioned at the edges of the gain region to be affected more adversely than those centered closer to the pump. It must be noted that PTN is *not* an *additive* but rather a *multiplicative* noise process, making the standard noise figure definition dependent on the input signal power. Consequently, the standard technique used to calculate the equivalent noise figure in links containing a cascade of amplifiers [24] is not applicable in FOPA-amplified systems.

Mediated by Kerr nonlinearity, pump amplitude fluctuations are nearly instantaneously converted to pump phase fluctuations. This amplitude-to-phase noise conversion was recognized early in transmission systems and dubbed nonlinear phase noise (NPN) by Gordon and Mollenauer [78]. The NPN is a major limitation in narrow linewidth frequency comb synthesis [79], high-fidelity supercontinuum generation [80, 81], very high power (>100W) amplification [82], and long-haul coherent communication systems [83]. Owing to nearly perfect phase matching among the propagating waves in HNLF, the NPN is transferred from the pump to the signal and the idler via highly efficient processes of cross-phase modulation (CPM) and four-wave-mixing (FWM). The influence of the NPN has been experimentally observed in saturated parametric amplifiers, where noise-loaded phase-shift-keyed (PSK) signal was partially regenerated using a saturated one-pump FOPA [84, 85]. The parametric amplitude limiter added NPN to the amplitude-regenerated signal. The amount of NPN increased with reduced pump optical signal-to-noise ratio (OSNR) and was also numerically shown to increase with increased pump power [86]. Finally, an expression for the variance of nonlinear phase noise in two-pump parametric amplifiers has been derived, accompanied by numerical calculations of SNR penalty for various PSK formats [87]. Not surprisingly, the formats whose closest symbols are the least distant in the phase plane were shown to suffer the largest penalty due to NPN. .

Entering the HNLF, the phase fluctuations of the pump wave are dominated by the necessity for pump phase modulation in order to suppress the stimulated Brillouin scattering (SBS). In this dissertation, we refer to this phase noise as phase modulation noise (PMN) of the signal and idler wave. The pump phase modulation results in severe spectral broadening of the idler wave that cannot be avoided in single-pumped FOPAs but can be mitigated in the dual-pumped case [61-63]. Pulsed-pump FOPAs and wavelength converters do not require pump phase modulation, provided that the pulse spectrum is significantly wider than the Brillouin bandwidth (approximately 20MHz in HNLFs). The impact of pump phase modulation on the amplitude fluctuations for on-off-keyed (OOK) signals [88, 89] and idler phase fluctuations for phase-shift-keyed (PSK) signals [90] have been studied previously.

In addition to pump-induced sources of phase noise (such as NPN and PMN), the FOPA is also subject to inherent amplified quantum noise (AQN). The AQN arises from parametric amplification of vacuum fluctuations at the signal wavelength as well as parametric conversion of AQN from idler to signal frequency [74]. Unlike the NPN and PMN, the variance of AQN-induced phase noise is dependent on input signal power level.

In Sec. 3.2, the statistics of the nonlinear phase will be derived and the impact of pump optical noise filtering, necessary in all practical systems employing amplified pumps, on the statistics of the nonlinear phase noise will be discussed. The expressions for signal and idler phase in one-pump FOPA will be derived in Sec 3.3, with particular attention given to the spectral dependence of NPN. In Sec 3.4, we will investigate pump phase modulation by radio-frequency (RF) noise as a means for spectrally-efficient SBS suppression, and quantify its effects on signal PMN. A simple expression for the variance of signal phase noise due to AQN in a one-pump FOPA will be derived in Sec. 3.5 and its validity confirmed using a rigorous numerical solver. Experimental setup for validation of theory and simulation in the preceding sections will be shown in Sec. 3.6, followed by results and discussion in Sec. 3.7.

3.2 Statistics of nonlinear phase noise

We begin the phase impairment analysis by considering the FOPA model illustrated in Figure 3.1. A pump wave with optical power P_p and carrier frequency ν_p is amplified in a high-power Erbium-doped fiber amplifier (EDFA), thereby accumulating white Gaussian optical noise. The original pump RIN and laser phase noise are considered to be negligible. The optical amplifier noise, $n(t)=n_r(t)+jn_i(t)$, is a complex white Gaussian random process [91]. The in-phase and quadrature components of the noise have zero mean and variance of $N_0\Delta\nu/2$, where N_0 is the noise power spectral density in one polarization and $\Delta\nu$ is the optical bandwidth of interest. The optical signal-to-noise ratio of the pump wave (measured within 0.1nm optical bandwidth) is given by

$OSNR_{0.1nm}=P_p/(2N_0\,\Delta\nu_{0.1nm})$, where $\Delta\nu_{0.1nm}$ is the frequency bandwidth corresponding to 0.1nm at the wavelength of c/ν_p

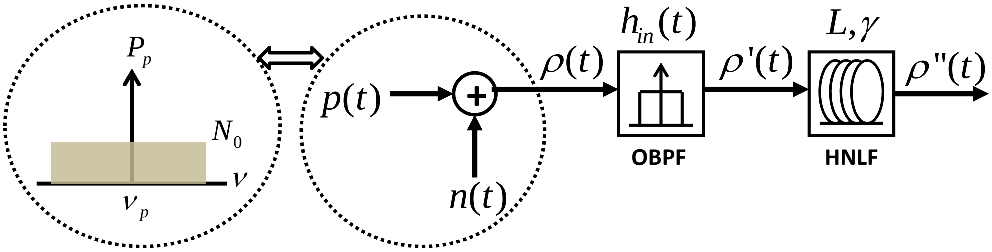

Figure 3.1: FOPA model schematic used in the derivation of NPN statistics; Acronyms: OBPF - optical band-pass filter; the rest of the symbols are defined within the text.

The optical band-pass filter is introduced to remove excess amplified spontaneous emission (ASE) and the complex pump field after the filter stage can be expressed as

$$\rho'(t)=\sqrt{P_p}+n(t)\otimes h_{in}(t)=\sqrt{P_p}+n'(t), \tag{3.20}$$

where $h_{in}(t)$ is the optical filter impulse response, and $n'(t)$ is the complex field of the filtered optical noise. The noisy complex pump field then enters HNLF characterized by fiber length L, nonlinear coefficient γ, and negligible intra-channel dispersion. While the assumption that HNLF has no intra-channel dispersion allows derivation of closed-form expressions, it is also justified in most practical cases as the pump positioning in the proximity of the zero-dispersion HNLF frequency is used to maximize the FOPA gain bandwidth [26]. Next, after the propagation through HNLF, neglecting the depletion and transmission loss, the pump complex field becomes:

$$\rho''(t)=\left(\sqrt{P_p}+n'(t)\right)e^{j\gamma L\left|\sqrt{P_p}+n'(t)\right|^2}=\left(\sqrt{P_p}+n'(t)\right)e^{j\phi_{NL}(t)}. \tag{3.21}$$

The nonlinear phase shift can further be rewritten as

$$\phi_{NL}(t) = \gamma P_p L + 2\gamma\sqrt{P_p} L n'_r(t) + \gamma L \,|\, n'(t)|^2 \; . \tag{3.22}$$

The second term in Eq. (3.3), the pump-noise beat term, dominates the noise performance since practical FOPAs require high pump OSNR. Neglecting the last (noise-noise beat) term, it is clear that the nonlinear phase noise remains a Gaussian-distributed process with zero mean. If we define N_0' to be the total single-polarization filtered noise power and note that the post-filtering variances of the $n_r'(t)$ and $n_i'(t)$ equal $N_0'/2$, then the variance of NPN is $2\gamma^2 L^2 P_p N_0'$.

Furthermore, it can be shown that the total nonlinear phase, $\phi_{NL}(t)$, is non-central χ^2-distributed with probability distribution function:

$$p_{\Phi_{NL}}(\phi_{NL}) = \frac{1}{\gamma L N_0'} e^{-\frac{\phi_{NL}+\gamma P_p L}{\gamma L N_0'}} I_0\left(\sqrt{\frac{4P_p}{\gamma L N_0'^2}}\sqrt{\phi_{NL}}\right). \tag{3.23}$$

The mean nonlinear phase shift is $\gamma L(P_p+N_0')$, while the variance is $\gamma^2 L^2 (2P_p N_0' + N_0'^2)$. Equation (4) is an approximation since a closed form analytical solution for the probability density function (PDF) of nonlinear phase exists only for rectangular and Lorentzian optical filter transfer functions [92].

At this juncture, it is important to point out an important difference between nonlinear phase induced in coherent communication systems and nonlinear phase in FOPAs. Firstly, optical filter bandwidths in communication systems typically exceed the signal bandwidths in order to avoid waveform distortions by the filter transfer function. Secondly, optical filters are not commonly used following the amplification process but only prior to final reception of the signal. Finally, any filtering is constrained by the fact that the NPN is distributed uniformly across the spectrum of the modulated signal. In contrast, optical pumps in FOPAs can be very narrowly filtered with bandwidths that must only be large enough to prevent the filter transfer function from converting any pump phase modulation into pump amplitude modulation. Consequently, it is reasonable to insist on spectrally efficient pump phase dithering for any SBS suppression. Following this motivation, we show in Sec. 3.4 that pump phase modulation driven by RF noise source occupying only 1.2GHz of optical bandwidth is sufficient to efficiently suppress SBS and enable more than 30dB of parametric gain. Therefore, the NPN (transferred from the pump to the signal via cross-phase modulation) bandwidth can be smaller than that of the amplified signal – a situation never encountered in coherent communication systems. In practical terms, narrow (sub-10GHz) and high-power-handling optical filters necessary for excess noise filtering of high-power FOPA pumps are not commercially available yet, dictating pump filtering with bandwidths typically exceeding 80GHz. As a consequence, the measurement of NPN becomes directly dependent upon the frequency response of the receiving photodiode and the subsequent electronics. The lower the bandwidth of the receiver, the higher the apparent phase fidelity will be, and vice versa.

3.3 Signal/idler phase noise

As the nonlinear phase noise is added to the pump wave during propagation in HNLF, it is also simultaneously transferred to the signal and idler. The signal and idler phase can be derived analytically by generalizing the analysis reported in [52], where several assumptions are made: (a) HNLF is lossless, (b) polarization effects are ignored (i.e., the propagating waves are perfectly aligned in polarization at all times), (c) no pump depletion by either the signal or the amplified quantum noise takes place, (d) the nonlinear coefficient γ is frequency-independent, and (e) Raman scattering is neglected. By incorporating these assumptions, the total phase mismatch is time-dependent and given by

$$\kappa(t) = \Delta\beta(t) + 2\gamma\left|\sqrt{P_p} + n'(t)\right|^2, \tag{3.24}$$

where the first term represents the linear phase mismatch, and the second term is the nonlinear phase shift due to the noisy pump power. The linear phase mismatch, $\Delta\beta(t)$, owes its time dependence to the phase modulation of the pump wave, as is often the case in continuous-wave FOPAs. The signal and idler amplitudes are affected by NPN and PMN via modulation of the exponential gain constant:

$$g(t) = \sqrt{\left(\gamma\left|\sqrt{P_p} + n'(t)\right|^2\right)^2 - \left(\frac{\kappa(t)}{2}\right)^2}. \tag{3.25}$$

The signal and idler phases at the output of HNLF can now be written as:

$$\phi_s(t,L) = \phi_s(t,0) + \tan^{-1}\left(\frac{\kappa(t)\sinh[g(t)L]}{2g(t)\cosh[g(t)L]}\right) + \gamma\left|\sqrt{P_p} + n'(t)\right|^2 L - \frac{\Delta\beta(t)L}{2} + \Delta\phi_{s,AQN}, \tag{3.26}$$

$$\phi_i(t,L) = \left[2\phi_p(t,0) - \phi_s(t,0)\right] + \frac{\pi}{2} + \gamma\left|\sqrt{P_p} + n'(t)\right|^2 L - \frac{\Delta\beta(t)L}{2} + \Delta\phi_{i,AQN}. \tag{3.27}$$

$\phi_s(t,0)$ and $\phi_p(t,0)$ represent the time-dependent phases of the signal and pump lasers before entering HNLF. Since narrow linewidth (<1MHz) lasers are practically available, the initial phase noises tend to be small in comparison to the third and fourth term, which represent NPN and PMN, respectively. The last term represents the AQN contribution to the signal and idler phase noise.

Table 3.1: FOPA simulation/experimental parameters

Symbol	**Description**	**Value**
L	HNLF length	175.0 m
γ	Nonlinear coefficient	15.0 $W^{-1}km^{-1}$
λ_0	Zero-dispersion wavelength	1562.15 nm
S	Dispersion slope	0.02 ps/nm^2-km
λ_p	Pump wavelength	1568.0 nm
P_p	Pump power	1.67 W

Figure 3.2(a) shows simulated SNR of nonlinear phase (third term in Eqs. (3.7-8)) as a function of pump OSNR and optical Gaussian filter 3-dB bandwidth. Consistent with Ref. [84], the phase SNR is defined as: $SNR_{phase}=1/Var\{\phi_{NL}(t)\}$. The simulation parameters used are specified in Table 3.1; they correspond to the constructed FOPA used in the experimental section of this work (Sec. 3.6). As expected from analysis in Sec. 3.2, the phase is corrupted by increased pump optical noise filter's bandwidth and reduced pump OSNR. The second term in Eq. (3.7) shows an additional noise source that is present in the signal phase and absent in the idler phase. The inverse tangent term is responsible for wavelength dependence of signal NPN contribution and will be termed *chromatic NPN* (CNPN) in subsequent discussion. Figure 3.2(b) depicts the analytically predicted and simulated spectral dependence of signal and idler phase and amplitude fidelity for pump OSNR of 40dB and a fixed optical Gaussian 3-dB bandwidth of 40GHz. The amplitude SNR in this calculation is defined as $(Mean\{A_{s,i}(t)\})^2/Var\{ A_{s,i}(t)\}$, where $A_{s,i}(t)$ is the time-varying signal/idler amplitude. All simulations were performed using a commercially available full Generalized Nonlinear Schrodinger Equation (GNLSE) solver (*VPItransmissionMaker*^{TM}). The linear phase mismatch, $\Delta\beta=$-

$\lambda_p^2/(2\pi c)S(\lambda_p-\lambda_0)(2\pi c/\lambda_s-2\pi c/\lambda_p)^2$ [93], is considered to be constant (i.e., no pump phase modulation), so that the CNPN term is only a function of pump amplitude noise, *n'(t)*. The signal phase exhibits strong variations at the edge of the parametric gain, significantly impairing the amplifier performance in this spectral region. In continuous-wave-pumped FOPAs, the idler phase is dominated by pump phase modulation and the first term in Eq. (3.8) dominates the noise properties of the idler phase. However, when pump phase modulation can be avoided, as in the case of pulsed-pump FOPAs, the signal phase still exhibits wavelength dependence, whereas the idler phase possesses purely achromatic properties. The increased stability of the idler's phase is accompanied by a significant increase in amplitude fluctuations, as can be seen in Figure 3.2(b). The noise induced by pump amplitude fluctuations, therefore, is distributed differently (in the two quadratures) for the amplified (signal) and converted (idler) wave. Interestingly, the only spectrally independent quadrature noise component is the phase noise of the idler wave.

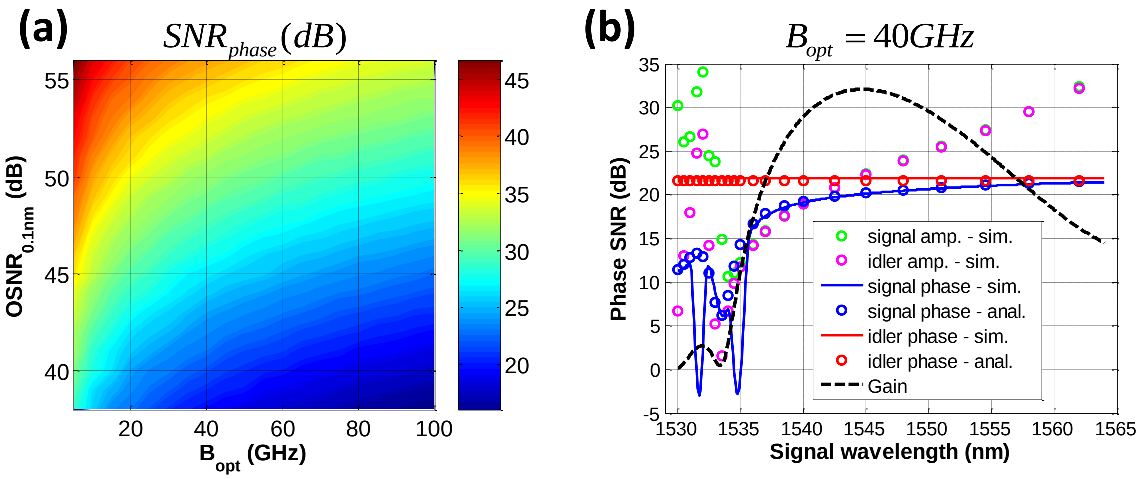

Figure 3.2: (a) Nonlinear phase SNR vs. pump OSNR and optical Gaussian noise filter 3-dB bandwidth; (b) Signal and idler phase and amplitude SNR spectra due to NPN.

3.4 Phase modulation noise

Pump phase modulation for SBS suppression in FOPAs has traditionally been implemented by means of one or more RF tones. Unfortunately, this method of phase modulation is bandwidth inefficient, since the frequency space between the original RF tones and their multiples is not utilized. In addition, effective SBS suppression dictates spectral equalization of the tones and the modulation 3-dB bandwidth can easily exceed 10 GHz [94]. Recognizing this limitation, we phase-modulate the pump by means of a filtered RF noise source, which provides for significantly narrower pump modulation bandwidths without sacrificing the SBS threshold increase [95]. The use of RF noise source as a phase modulator driver poses specific practical requirement. For a modulator characterized by a specific voltage necessary to induce π-retardation (V_π), the variance of the driving time-varying voltage, $\sigma^2_{V(t)}$, must equal V_π^2 in order to optimally suppress the optical carrier. Then, the required RF noise power spectral density is given by $S_{n,rf} = (V_\pi^2/R_L)/\Delta f_{n,rf}$, where R_L is the load impedance, and $\Delta f_{n,rf}$ is the electrical bandwidth of RF noise. The pump instantaneous frequency, $\nu_p(t)=c/\lambda_p+(1/2\pi)d\phi_p(t)/dt$, is a function of the instantaneous pump phase, $\phi_p(t)=\pi V(t)/V_\pi$, defining the linear phase mismatch as

$$\Delta\beta(t)=\frac{-2\pi c}{\nu_p^{\,2}(t)}S\left(\frac{c}{\nu_p(t)}-\lambda_o\right)\left(c/\lambda_s-\nu_p(t)\right)^2. \tag{3.28}$$

The higher order dispersion coefficients (β_4, β_6, etc.) have purposely been omitted since their contributions to the linear phase mismatch are negligible in the bandwidth of interest (100 nm). A distant spectral conversion [46] or wide-band parametric amplification and frequency generation would require the inclusion of higher-order dispersive terms. Figure 3.3(a) shows a contour plot of signal phase SNR as a function of signal wavelength and the electrical noise 3-dB Gaussian bandwidth in the absence of NPN (i.e., $n'(t)=0$) and using parameters in Table 3.1. Figure 3.3(b) depicts the signal phase SNR spectrum for a 600MHz electrical noise bandwidth. As expected from Eq. (3.9), the phase SNR reduces as the pump-signal wavelength separation is increased. At the edge of the gain spectrum, the interaction between the $\Delta\beta(t)L/2$ term and the CNPN term in Eq. (3.7) results in sharp spectral features. These spectral features are smoothed when some amount of pump amplitude noise (and hence NPN) is present, as is always the case in practical FOPA devices. By comparing Figure 3.2(b) and Figure 3.3(b), we come to expect the PMN to make at least an order of magnitude smaller contribution to the total phase noise than NPN. The two noise variances become comparable when the pump OSNR exceeds 55 dB and pump noise is narrowly (i.e. sub-20GHz) filtered in order to reduce NPN. It is interesting to note that PMN increases with increased HNLF length (see Eqs. (3.7-8)). Hence, we expect FOPAs employing the combination of longer fiber lengths and reduced pump powers to have a larger contribution of PMN to the total phase noise, thus posing another challenge in devising cost-effective FOPA devices.

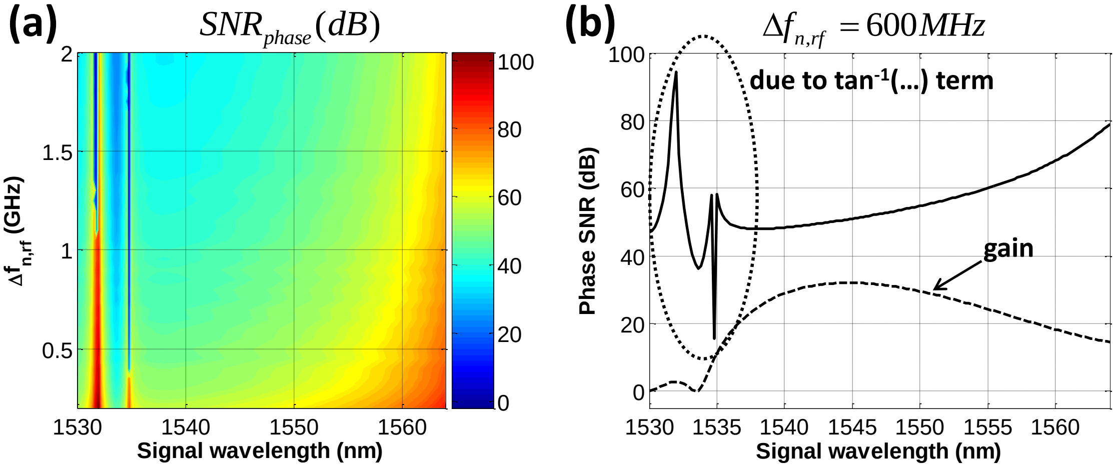

Figure 3.3: Spectral dependence of signal phase SNR when only PMN is present (a) for a range of RF noise bandwidths, (b) for 600MHz RF noise bandwidth.

3.5 Phase noise due to amplified quantum noise

The exact statistics of phase noise in phase-insensitive inverted-population optical amplifiers (often referred to as *linear* optical amplifier), where *equal* amount of Gaussian-distributed noise is added by the amplifier to both quadrature components of the signal, are well known [96]. In case of high (>10 dB) signal-to-noise ratio at the output of the amplifier, the phase variations are dominated by the imaginary part of complex white Gaussian noise and the phase variance is inversely proportional to the SNR [96]. The SNR is given by GP_s/P_n, where G is the amplifier gain, P_s is the input signal power, and P_n is the total noise power in one quadrature and one polarization. For EDFAs, $P_n=\frac{1}{2}h\nu_s\Delta\nu n_{sp}(G-1)$, where h is the Planck's constant, ν_s is the signal frequency, $\Delta\nu$ is the optical bandwidth, and n_{sp} is the spontaneous emission factor [24]. Thus, in the limit of high gain (i.e. G >> 1), the phase SNR due to ASE becomes $2P_s/(h\nu_s\Delta\nu n_{sp})$.

The parametric amplifier is seeded by zero-point ‘vacuum’ fluctuations with power spectral density of $h\nu/2$ in one polarization, as illustrated in Figure 3.4. The vacuum fluctuations at the signal wavelength are amplified by parametric gain $G_s=1+(\gamma P_p/g)^2\sinh^2(gL)$ [93]. In addition, the signal is coupled to the AQN associated with the idler, which is amplified by gain of G_s-1. Adding the two noise contributions, the total power of AQN in one polarization and both quadratures is given by

$$P_{AQN}=\frac{h\nu}{2}(G_s+G_s-1)\Delta\nu=\frac{h\nu}{2}(2G_s-1)\Delta\nu. \tag{3.29}$$

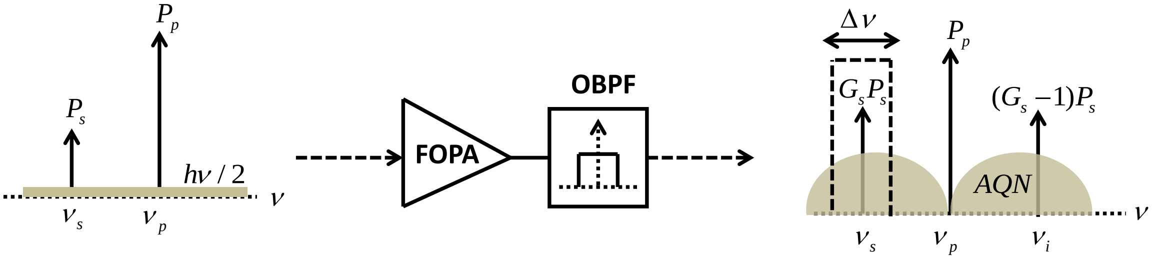

Figure 3.4: Schematic of parametric amplification of quantum noise in a one-pump FOPA. Acronyms: P_s – signal power, ν_s – signal frequency, ν_p – pump frequency, P_p – pump power, OBPF – optical band-pass filter, ν_i – idler frequency, G_s – signal gain, $\Delta\nu$ – optical filter bandwidth, AQN – amplified quantum noise.

The photon number and field-quadrature fluctuations of the phase-insensitive parametric amplifier have been shown to be equivalent to those of the zero-noise-input inverted-population amplifier (e.g. EDFA), provided that complete population inversion is achieved in the case of the latter [74, 97, 98, 99]. In other words, the phase-insensitive parametric amplifier adds a circular (in the complex plane) noise cloud to the amplified signal, analogous to its inverted-population counterpart. Consequently, owing to the statistical similarities of the two noise processes (ASE and AQN), it can straightforwardly be concluded that the variance of signal phase noise due to AQN is identical to that of a perfectly inverted EDFA, with signal phase SNR given by

$$SNR_{phase} = \frac{1}{\sigma^2_{\Delta\phi_{AQN}}} = \frac{4G_s P_s}{h\nu(2G_s - 1)\Delta\nu}. \tag{3.30}$$

The validity of simple theory leading to Eq. (3.11) was confirmed via simulation employing a full GNLSE solver for FOPA with parameters listed in Table 3.1. An excellent agreement was found and the results are depicted in Figure 3.5. The analytical approach works even when FOPA is operating near the transparency regime (i.e. at left edge of the gain region in Figure 3.5(a)), where the phase fidelity of the input signal(s) is not impaired by the parametric amplifier.

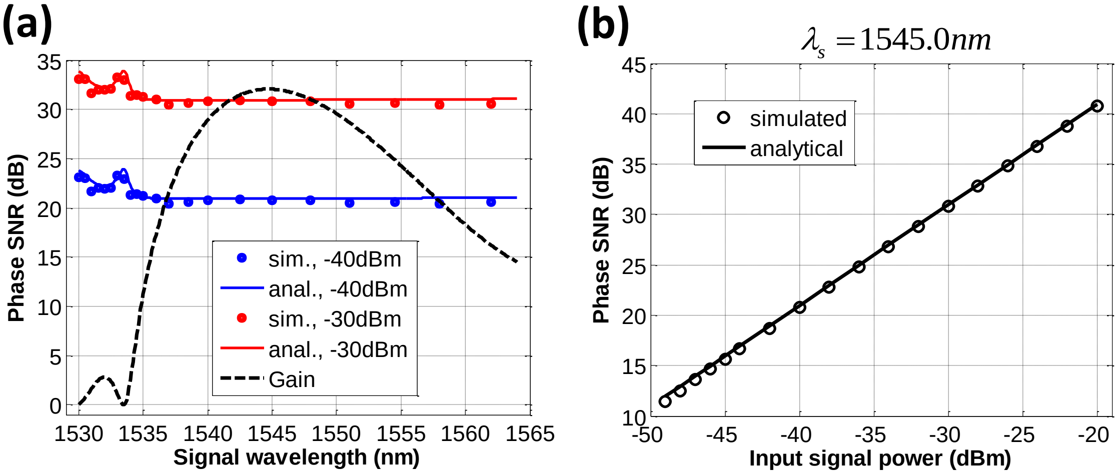

Figure 3.5: Analytical/numerical signal phase SNR (when only AQN is present): (a) spectrum for two different input signal powers; (b) dependence on input signal power at the signal wavelength of 1545.0nm.

3.6 Experimental setup

An experimental setup for phase noise characterization in a one-pump FOPA was constructed as shown in Figure 3.6. HNLF and pump parameters are given in Table 3.1.

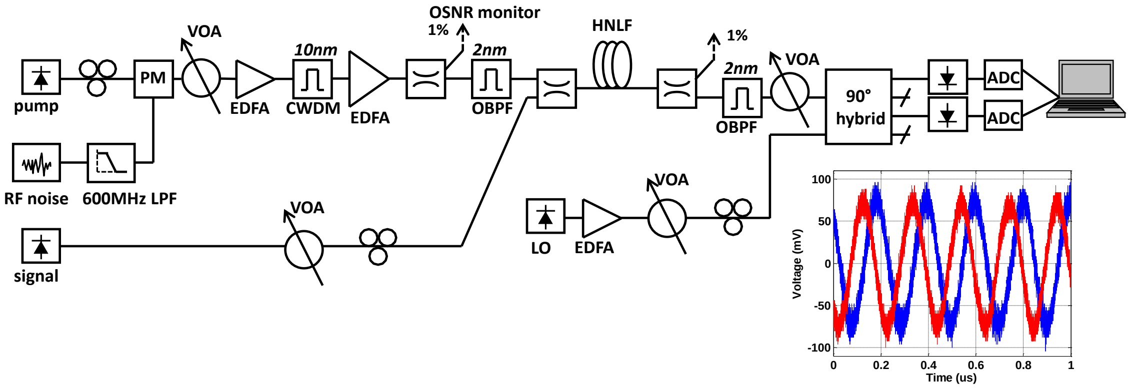

Figure 3.6: Experimental setup for measurement of phase noise of a FOPA; Inset: electrical waveforms observed after intra-dyne detection of the two output ports of the 90° hybrid. Acronyms: PM – phase modulator, LPF – low-pass (RF) filter, VOA – variable optical attenuator, EDFA – Erbium-doped fiber amplifier, CWDM – coarse wavelength-division multiplexer, HNLF – highly nonlinear fiber, OBPF – optical band-pass filter, LO – local oscillator, ADC – analog-to-digital converter.

The pump, signal, and local oscillator (LO) were standard external cavity lasers and all had 100kHz linewidths. The pump phase was dithered using a 3GHz-bandwidth RF noise source constructed for spectrally efficient SBS suppression and filtered with a 600 MHz low-pass electrical filter. The filtered noise bandwidth provided approximately 14 dB of SBS threshold increase, which was more than sufficient to fully suppress SBS in the constructed amplifier. A variable optical attenuator, preceding a cascade of low-power and high power EDFAs, was used to vary the OSNR of the pump wave. The pump optical noise was filtered with a combination of a coarse-wavelength-division-mutiplexer (CWDM) filter and a 2 nm 3-dB bandwidth band-pass filter with approximately Lorentzian optical power transfer function. The CWDM possessed high extinction, in excess of 45 dB, required to guarantee that the filtered amplifier noise at the signal frequency had lower power spectral density than the inherently present quantum noise. The authors in [77] refer to the poorly-suppressed (and subsequently amplified by

FOPA) amplifier noise as *pump residual noise*; the experimental setup constructed in this work aimed to control such contribution. Input signal power into the FOPA was kept constant at -20 dBm. Following amplification in HNLF, the signal wave was filtered out and combined with an amplified local oscillator (LO) wave in a 90° optical hybrid. Two of the hybrid's outputs ($S+LO$ and $S+jLO$) were detected using matched 20GHz linear *p-i-n* photodiodes with responsivity of 0.95A/W. Incident on the photodiodes, the signal power was kept constant at -20 dBm and the LO power at 10 dBm. The two beat currents, depicted in the inset of Figure 3.6 were measured on a 50 Gs/s real-time oscilloscope (Tektronix DPO71604B) characterized by 16dB-bandwidth 4th-order Butterworth frequency response.

3.7 Experimental results and discussion

Optical spectra after the FOPA for two different signal wavelengths are shown in Figure 3.7(a) and measured gain spectra are shown in Figure 3.7(b). While the gain for the two signal wavelengths in Figure 3.7(a) is nearly the same, the OSNR of the farther signal is approximately 6 dB lower than the OSNR of the signal closer to the pump. We therefore expect the farther signal to have higher phase noise. It is also interesting to note that pump's OSNR has reduced by about 15 dB following propagation in HNLF, which is equal to the parametric gain in the vicinity of the pump. Indeed, the reduced OSNR is a consequence of added nonlinear phase noise. However, the pump amplitude SNR is unchanged since we know that the pump only acquires a nonlinear phase shift [52].

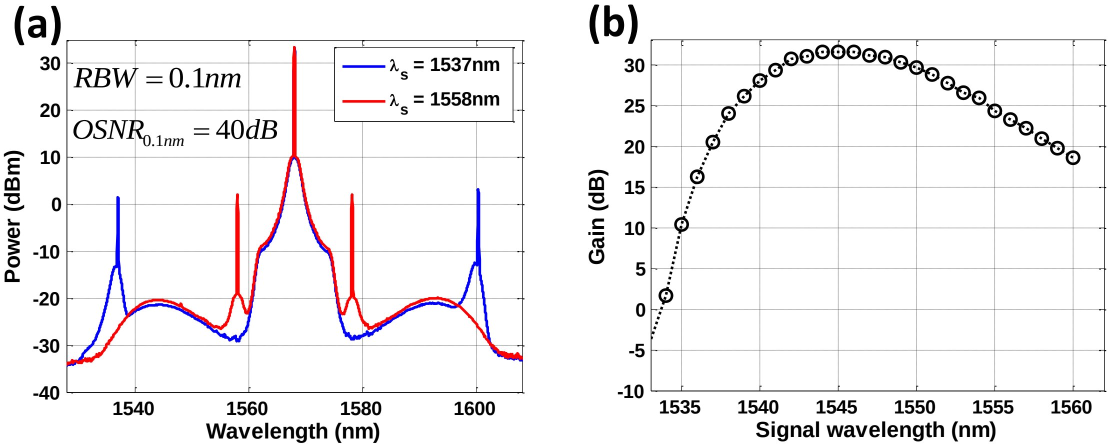

Figure 3.7: (a) Optical spectra for two different signal wavelengths, (b) Measured FOPA gain spectrum

High-resolution optical spectra of pump/signal/idler waves were taken after the FOPA and are depicted in Figure 3.8(a). As expected, the pump and idler frequencies are significantly broadened. The idler spectral broadening is approximately twice as large as that of the pump because two pump photons are involved in the four-photon interaction ($2f_p \rightarrow f_s + f_i$). Looking closely at the high-resolution optical spectrum of the signal wave at different pump OSNRs (Figure 3.8(b)), we clearly see the spectral contribution of the narrowband PMN and broadband NPN. Since the measured phase noise will be integrated over 16 GHz of electrical bandwidth, we expect the NPN-induced phase noise to dominate the signal phase SNR. The two sharp peaks located 170MHz away from the signal center frequency are the laser cavity sidemodes; they are suppressed by approximately 50 dB with respect to the carrier.

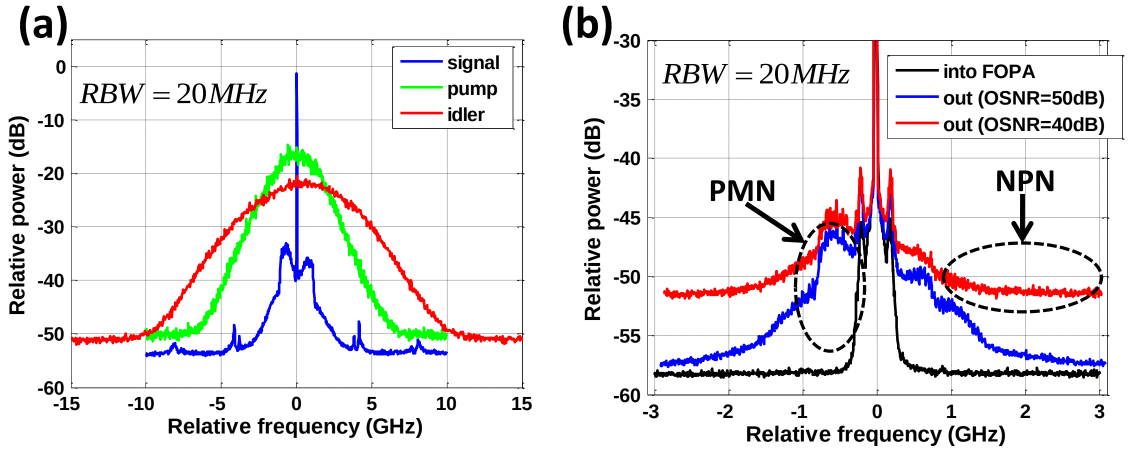

Figure 3.8: (a) Optical spectra of pump/signal/idler after HNLF; (b) Signal spectrum before and after FOPA. The three disjoint spectral bands centered on the three characteristic wavelengths (signal - 1545.0nm, pump - 1568.0nm, and idler - 1591.7nm) have been shifted for easier comparison.

The waveforms captured by the real-time oscilloscope were processed off-line (as outlined in [84]), and the wavelength-dependent signal phase SNR and amplitude SNR are plotted in Figure 3.9. The pump OSNR of 40 dB was used in order to allow the NPN to dominate the signal phase noise and measure the predicted spectral dependence. As expected from the analysis in Sec. 3.3, the measured phase SNR is lower at the edges of the parametric gain and increases as the signal wavelength approaches that of the pump. An excellent agreement is found among the analytically predicted, the numerically simulated and the experimentally measured signal phase SNR spectra. The signal amplitude SNR is wavelength-dependent owing to wavelength-dependent gain sensitivity to pump power [77]. The gain sensitivity increases with increased pump-signal separation and the signal suffers larger amplitude noise as evident in Figure 3.9.

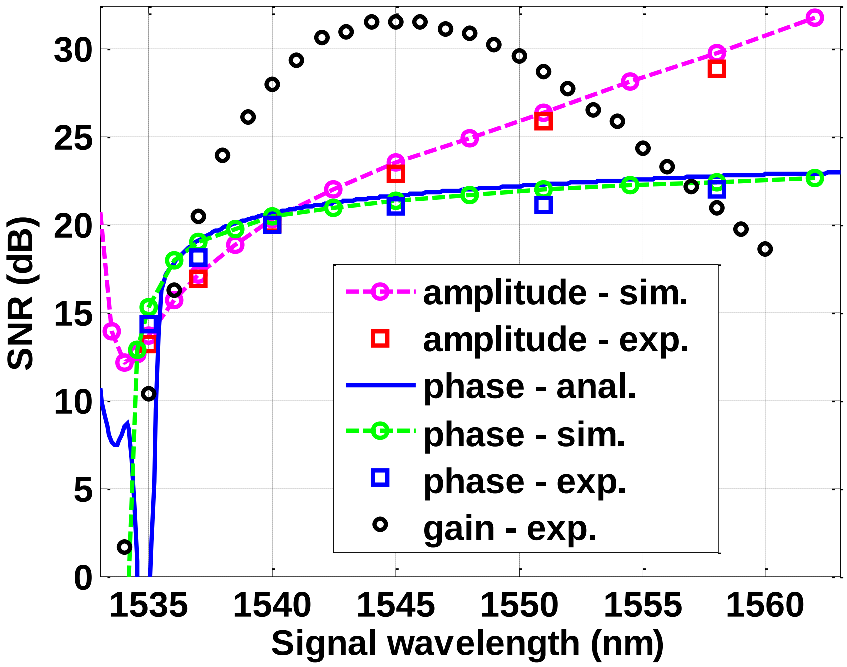

Figure 3.9: Measured, simulated, and analytically predicted signal phase and amplitude SNR spectra for input pump OSNR of 40dB.

3.8 Chapter summary

In this Chapter, we have analytically predicted and experimentally verified the spectral dependence of amplified signal and converted idler phase noise in a one-pump fiber-optic parametric amplifier. We demonstrated that, when the pump phase is modulated in a bandwidth efficient manner, the nonlinear phase noise dominates over other parametric amplifier's noise contributions. This finding has a basic implication as it dictates use of specific means for pump dithering that are similar to RF noise driven modulation used in this work.

Furthermore, it was shown that the phase fidelity exhibits a strong spectral dependence and is significantly degraded at the edges of the gain region. More importantly, the derived analytical theory implies that the idler phase noise exhibits no spectral dependence in the absence of pump phase modulation. However, the idler's superior phase fidelity is accompanied by an increase in field amplitude fluctuations and casts qualitative new light on the construction of spectrally mapped systems. The main conclusions of this work thus bear significant implications on the design and construction of parametric amplifiers/converters, where frequency and amplitude stability of the newly generated wave(s) is of utmost importance.

Chapter 3, in full, is a reprint of the material as it appears in "Phase noise in fiber-optic parametric amplifiers and converters and its impact on sensing and communication systems," by S. Moro, A. Peric N. Alic, and S. Radic, Optics Express, Vol. 18, 2009. The dissertation author was the primary investigator and author of this paper.

4. Nonlinear frequency chirping vs. nonlinear phase noise

4.1 Introduction

All of the aforementioned nonlinear phase noise (NPN) studies have assumed the impairment source to be the white Gaussian optical noise. In the case of coherent communication systems, the amplitude noise is accumulated during signal wave amplification and converted to phase noise via either self-phase or cross-phase modulation [100]. In either case, it is well understood that only the noise present within the signal bandwidth is relevant for the correct prediction of the NPN statistics. In FOPA, however, a possibility of very narrow optical filtering of the amplified pump wave exists and does not have an equivalent in conventional communications systems in which the filter bandwidth is limited by the channel rate. Thus, the filtered noise bandwidth can be smaller than or larger than the amplified signal bandwidth. In this Chapter, we will demonstrate for the first time that the variance of NPN remains unchanged, whereas the variance of the nonlinear chirp (NC) increases with increased optical noise bandwidth (accompanied by decreased noise power spectral density such that the total noise power is constant). The results bear significant practical ramification on the construction and performance of parametric amplifiers and converters.

In Sec. 4.2, the statistics of nonlinear phase noise and nonlinear chirp will be derived and contrasted. The experimental setup constructed to validate the theoretical findings will be described in Sec. 4.3, followed by experimental results and discussion in Sec. 4.4.

4.2 Statistics of nonlinear phase noise and nonlinear chirp

We begin the analysis by considering the simplest $\chi^{(3)}$ parametric amplification architecture shown in Figure 4.1. A pump wave with optical power P_p and carrier frequency v_p is amplified in an optical amplifier (e.g. EDFA), thereby accumulating white Gaussian optical noise. The pump RIN and laser phase noise are considered to be negligible. The optical amplifier noise, $n(t)=n_r(t)+jn_i(t)$, is a complex white Gaussian random process [101]. The in-phase and quadrature components of the noise have zero mean and variance of $N_0\Delta v/2$, where N_0 is the noise power spectral density in one polarization and Δv is the optical bandwidth of interest. The optical signal-to-noise ratio of the pump wave (measured in 0.1nm optical bandwidth) is given by $OSNR_{0.1nm}=P_p/(2N_0 \Delta v_{0.1nm})$, where $\Delta v_{0.1nm}$ is the frequency bandwidth corresponding to 0.1nm at the wavelength of c/v_p.

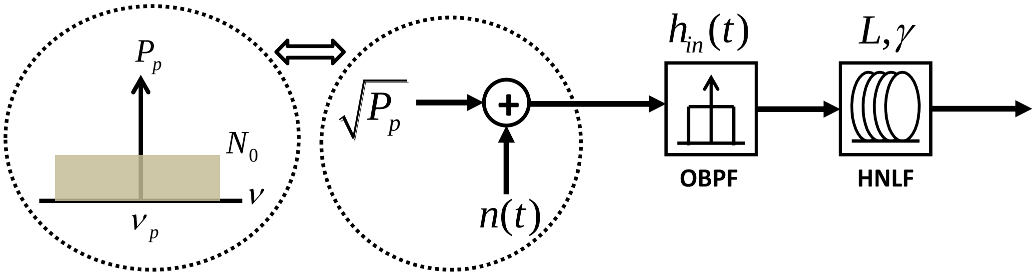

Figure 4.1: Schematic for analytical derivation of NPN/NC statistics; Acronyms: OBPF - optical band-pass filter.

The complex pump field is subsequently band-pass filtered before entering the nonlinear waveguide (e.g. HNLF) characterized by fiber length L, and nonlinear coefficient γ. We consider intra-channel dispersion of the HNLF at the pump frequency to be negligible in order to allow a closed form derivation. This assumption is justified in most practical cases, where the pump is placed very close to the zero-dispersion wavelength of the HNLF in order to maximize the gain (and/or conversion efficiency) bandwidth. After propagation through HNLF, and neglecting HNLF loss and pump depletion, the pump acquires nonlinear phase noise

$$\Delta\phi_{NL}(t) = 2\gamma\sqrt{P_p}Ln'_r(t) + \gamma L|n'(t)|^2, \tag{4.1}$$

where $n'(t)=n(t)\otimes h_{in}(t)$ is the complex field of the filtered optical noise and $h_{in}(t)$ is the optical filter impulse response. The signal and idler acquire the same nonlinear phase shift ($\gamma P_p L$) as the pump [52], and they are thus subject to the same NPN. The last term in Eq. (4.1), the *noise-noise beat* term, can be neglected since practical parametric amplifiers/converters require high pump OSNRs in order to minimize the *pump-transferred noise* [77]. Accordingly, the variance of NPN can be expressed as

$$\sigma^2_{\Delta\phi_{NL}} = 2\gamma^2 L^2 P_p \int_{-\infty}^{\infty} S_{n'}(\omega)d\omega \tag{4.2}$$

where $S_n(\omega)$ is the power spectral density of $n'(t)$.

On the other hand, the noise-induced nonlinear frequency chirp is given by

$$\Delta f_{NL}(t) = \frac{1}{2\pi}\frac{d[\Delta\phi_{NL}(t)]}{dt} = \frac{\gamma\sqrt{P_p}L}{\pi}\frac{dn'_r(t)}{dt} \tag{4.3}$$

As asserted by Eq. (4.3), the nonlinear chirp (NC) is proportional to the time derivative of the nonlinear phase and is, therefore, significantly influenced by the time scale on which the pump amplitude varies. In order to calculate the second-order statistics of the NC, we use the fact that *n'(t)* is a second-order wide-sense-stationary (WSS) random process [102]. Then, it can be shown that [104]

$$E\left\{\left|\frac{dn'(t)}{dt}\right|^2\right\} = \frac{\partial^2}{\partial t \partial s} R(t,s)\,|_{t=s} = -R^{(2)}(0) = \int_{-\infty}^{\infty} \omega^2 S_{n'}(\omega) d\omega, \tag{4.4}$$

where *E{…}* is the statistical expectation operator and $R(\tau)=E\{n'(t)n'(t+\tau)\}$ is the autocorrelation of the optically filtered noise *n'(t)*. Consequently, the variance of NC is

$$\sigma^2_{\Delta f_{NL}} = \frac{\gamma^2 L^2 P_p}{2\pi^2} \int_{-\infty}^{\infty} \omega^2 S_{n'}(\omega) d\omega. \tag{4.5}$$

It is important to reflect on the implications of Eqs. (4.2) and (4.5). As would be expected, the variances of both NPN and NC depend on the nonlinear parameters (γ, P_p, and L). From Eq. (4.2), it is evident that the variance of NPN, a commonly considered quantity in NPN investigation, depends solely on the *total noise power* (i.e. the noise power integrated over the optical filtered bandwidth). In sharp contrast, in the expression for the variance of NC (Eq. (4.5)), the noise power spectral density is weighted by the ω^2 term. The angular frequency weighting is a consequence of the temporal change of the statistical properties, mediated by propagation in Kerr media. As a result, *the noise spectral width plays a crucial role in the NC statistics*, as illustrated in Figure 4.2. The impact of low-power high-frequency noise components of $S_{n,1}(\omega)$ is exacerbated via multiplication byω^2 weighting factor. To illustrate this feature, Figure 4.2(b) and Figure 4.2(c) show the contour plots of standard deviation of NPN and NC, respectively, for a fixed nonlinear phase shift of $\gamma P_p L=5$. The most important feature of plots 4.2(b) and 4.2(c) is that the steeper NC contour slope suggests that even when the total noise power is kept constant, the spectrally broader pump optical noise (with appropriately reduced noise power spectral density) will induce a larger spectral broadening than it's spectrally narrower counterpart. As a direct consequence of Eq. (4.5), *the narrow pump filtering is critical in construction of high-signal-integrity parametric amplifiers and converters*.

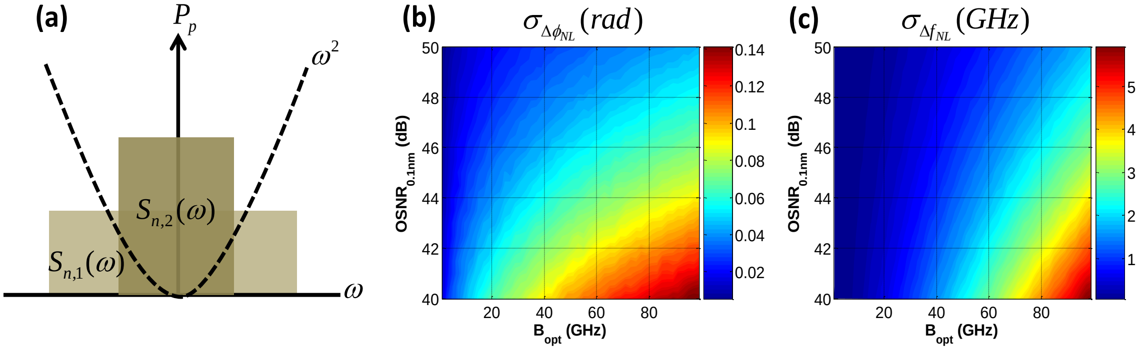

Figure 4.2: (a) Schematic illustrating the influence of ω^2 weighting factor on two different noise power spectral densities; Standard deviation of (b) NPN and (c) NC vs. pump OSNR and 3-dB optical Gaussian noise filter bandwidth.

4.3 Experimental setup

An experimental setup was constructed in order to characterize the noise-induced NC and validate the analytical findings, as shown in Figure 4.3. The pump wave, centered at 1589.0 nm, was amplitude modulated to produce 1ns pulses with 30 dB duty cycle. The pump OSNR was varied by varying the input power into the optical amplifier cascade. The optical noise bandwidth was controlled via a flat-top variable-bandwidth OBPF with power transfer functions shown in the left inset of Figure 4.3. The amplified pump wave and the surrounding filtered noise were passed through 180m-long HNLF with nonlinear coefficient of 13 W^{-1}km^{-1} and a global zero-dispersion wavelength (ZDW) of 1589.0 nm (which is exactly equal to the pump wavelength). The right inset in Figure 4.3 shows the optical spectrum after HNLF. The broadband amplified quantum noise

(AQN) is attributed to parametric gain's high sensitivity to ZDW fluctuations, especially when the pump is placed at the global ZDW [104]. The pump power entering HNLF was 5.2 W, resulting in a total nonlinear phase shift of 12.168 radians. In order to quantify the noise-induced NC, 300m-long standard single-mode fiber (SMF) was inserted to convert pump phase fluctuations into amplitude fluctuations (PM-to-AM) via dispersion (19.239 ps/nm-km at 1589.0 nm). The VOA preceding the fiber was used to attenuate the pump wave to peak power of 10 mW in order to avoid nonlinear effects in SMF. The amplitude fidelity of the pump wave was characterized using an optical sampling oscilloscope with an electrical bandwidth of 500 GHz. The oscilloscope bandwidth was much larger than the widest optical noise bandwidth (144 GHz), ensuring that no smoothing of the noisy optical waveform by the receiver took place.

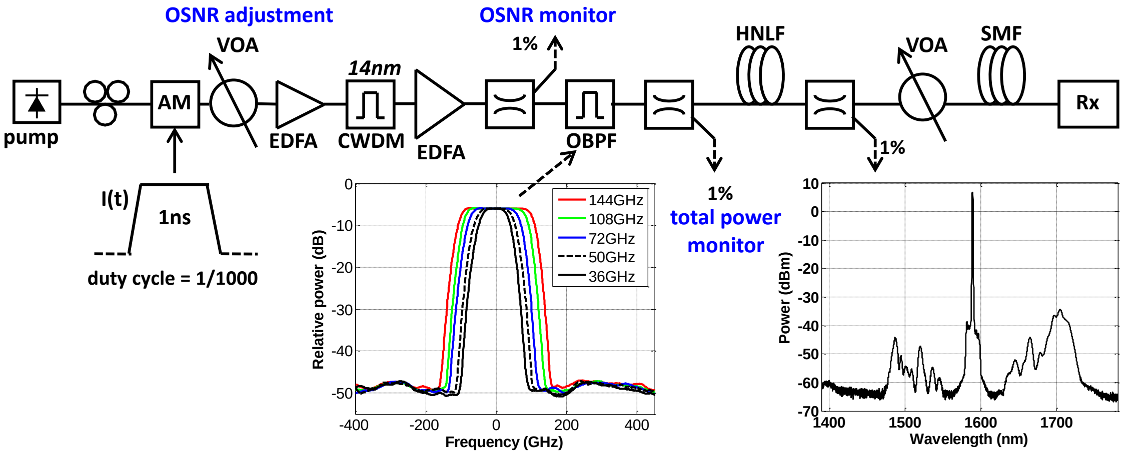

Figure 4.3: Experimental setup for noise-induced NC measurement; Left inset: measured optical filter transfer functions; Right inset: optical spectrum after HNLF propagation; Acronyms: AM – amplitude modulator, EDFA – Erbium doped fiber amplifier, CWDM – coarse wavelength division multiplexer, OBPF – optical band-pass filter, VOA – variable optical attenuator, SMF – single-mode fiber, Rx – optical receiver.

4.4 Experimental results and discussion

Figure 4.4(a) shows the measured electrical SNR as a function of the optical filter bandwidth. The OSNR required to keep the total optical noise power constant is shown on the right vertical axis. The total noise power at OSNR of 50 dB and optical filter bandwidth of 144 GHz was used as a reference and kept constant as the filter bandwidth and OSNR were varied for the remaining four data points. An excellent agreement between the semi-analytical model outlined in the Appendix and the measured SNR is recognized in Figure 4.4(a). We note that the introduced semi-analytical model enables complete inference of the statistical properties of NPN and NC, shown in Figure 4.4(b). As stated previously, the results unambiguously demonstrate that the standard deviation of NPN is unchanged as the filter bandwidth and pump OSNR are varied. In sharp contrast, the standard deviation of NC approximately doubles when the filter bandwidth is quadrupled (e.g. from 36 GHz to 144 GHz). Thus, the findings are in perfect accord with the analysis in Sec. 4.2.

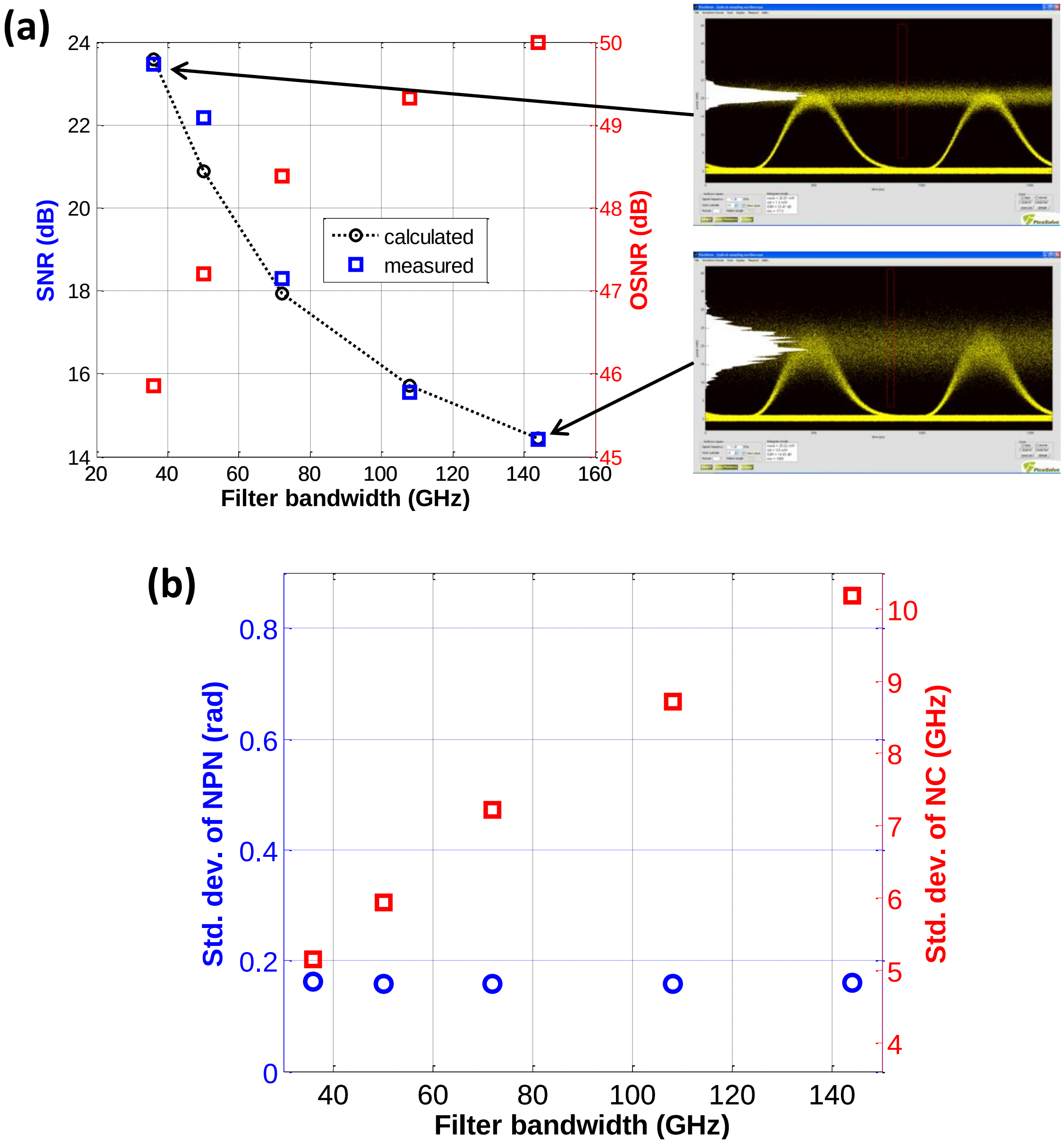

Figure 4.4: (a) Measured pump SNR vs. optical filter bandwidth following PM-to-AM in SMF; (b) Standard deviation of NPN and NC vs. optical filter bandwidth.

4.5 Conclusion

In this Chapter, the statistics of nonlinear phase noise and nonlinear frequency chirp arising from amplitude noise to phase noise conversion in a $\chi^{(3)}$ nonlinear medium are experimentally and analytically studied and quantified. The study reveals the relative importance of noise power spectral density and noise optical bandwidth. It is found that narrow optical noise filtering, rather than low noise power spectral density, plays the dominant role in successful management of noise-induced nonlinear frequency chirping. The result represents an important step towards the understanding of the impairments associated with spectral broadening of the amplified and the newly-generated waves in fiber parametric mixers. Specifically, the quantified NPN and NC impairments lead to new FOPA(C) construction rules not implemented in the past.

Most importantly, the results of this study state that the statistics of noise-induced nonlinear chirp, rather than those of the nonlinear phase noise, correctly describe the phase degradation of the interacting mixer waves. This conclusion is quite general and not necessarily limited to fiber devices, applying to all processes plagued by the nonlinear phase noise.

5. Parametric gain synthesis in the continuous-wave regime

5.1 Introduction

Parametric interaction in highly-nonlinear fiber has been regarded as one of the most efficient means of increasing the bandwidth available to fiber-optic communications and signal-processing systems [26, 105]. The need to cascade either lumped (e.g. EDFAs) or distributed (e.g. Raman) amplifiers in long-haul optical communications systems demands high, spectrally flat, and wideband amplification [106]. Although the low complexity and cost of mature erbium-doped fiber amplifier (EDFA) technology are difficult to match, the spectroscopic properties of the Erbium ion place a heavy constraint on significantly extending the gain bandwidth. The best reported EDFA performance, without the use of external spectral equalization, shows 15 dB average gain over 105 nm bandwidth with 2.7 dB spectral ripple [107]. The Raman amplifier technology is more difficult to spectrally equalize; the highest reported performance is characterized by 160nm-bandwidth with gain in the 10-20 dB range [108].

Contrary to ion-based amplification techniques, fiber-optic parametric amplifier (FOPA) technology is restricted only by the phase-matching conditions which can be controlled via dispersion engineering of HNLF. However, microscopic variations in HNLF transverse geometry inherent in the fabrication process lead to spatially localized zero-dispersion wavelength (ZDW) fluctuations. Consequently, the pump-probe phase matching varies along the fiber length and the FOPA spectral response drastically varies for HNLF segments possessing identical global characteristics [109, 110]. Recently, a record one-pump FOPA having 11.5 dB of average gain over a 100 nm 4-dB equalized bandwidth was demonstrated [112]. In addition to the effects of the Raman response and higher order dispersion, the ZDW fluctuation presents a fundamental constraint in the synthesis of more broadband equalized parametric gain. Even though utilization of longer HNLF segments increases the achievable gain, it equally incurs additional dispersive fluctuations, compromising the equalized gain bandwidth. In recognition of the physical limitations imposed by already remarkable HNLF fabrication tolerances, a new method for localized dispersion mapping of low-dispersion waveguides such as HNLF was developed [111, 113].

Aided by localized ZDW maps for candidate HNLFs, record parametric gain response will be synthesized for one-pump and two-pump FOPAs in Sec. 5.2 and 5.3, respectively. The importance of ZDW fluctuation map will be further emphasized in Sec. 5.2, where parametric response of two different (and neighbouring) segments from the identical HNLF spool is contrasted. In Sec. 5.4, continuous-wave SWIR conversion gain to beyond 2.2μm will be presented.

5.2 One-pump gain synthesis in the NIR

5.2.1 Numerical gain synthesis

The spectral response of a one-pump FOPA, subject to ZDW variations, can be calculated by solving the following set of coupled-mode equations [109]:

$$\begin{aligned}\frac{dA_{s,i}}{dz} &= -\frac{\alpha}{2}A_{s.i} + j\gamma\left[\left(\left|A_{s.i}\right|^2 + 2\left(\left|A_{i,s}\right|^2 + \left|A_p\right|^2\right)\right)A_{s,i} + A_p^2 A_{i,s}^* e^{-j\int \Delta\beta_L(z)dz}\right] \\ &+ j\gamma\left[f_R A_{s,i}\int_0^{\infty} h(\tau)\,|A_p(t-\tau)|^2 d\tau\right],\end{aligned} \tag{5.1}$$

$$\begin{aligned}\frac{dA_p}{dz} &= -\frac{\alpha}{2}A_p + j\gamma\left[\left(\left|A_p\right|^2 + 2\left(\left|A_s\right|^2 + \left|A_i\right|^2\right)\right)A_p + 2A_sA_iA_p^* e^{j\int \Delta\beta_L(z)dz}\right] \\ &+ j\gamma\left[f_R A_p\int_0^{\infty} h(\tau)\,|A_p(t-\tau)|^2 d\tau\right].\end{aligned} \tag{5.2}$$

where A_p, A_s, and A_i, are the amplitudes of the pump, signal, and idler waves, respectively, α is the fiber attenuation coefficient, γ is the nonlinear coefficient, and f_R is the fractional Raman contribution (equal to 0.18 in silica fibers). The linear phase mismatch between the interacting waves is given by

$$\Delta\beta_L(z) \simeq \frac{-\lambda_p^2}{2\pi c}S(\lambda_p - \lambda_0(z))(\omega_s - \omega_p)^2 + \frac{\beta_4}{12}(\omega_s - \omega_p)^4, \tag{5.3}$$

where λ_p is the pump wavelength, c is the speed of light in vacuum, S is the dispersion slope, λ_0 is the zero-dispersion wavelength (ZDW) of the fiber, β_4 is the fourth-order dispersion coefficient, and $\omega_{s,p}$ are the angular frequencies of the signal and pump waves, respectively.

First, the Raman response of HNLF1, having parameters as listed in Table 5.1, was characterized with details of the measurement described in Appendix B. The Raman impulse response, *h(τ)*, was calculated and subsequently used in numerical simulations of the expected parametric response. A one-pump continuous-wave FOPA was constructed using a 175m long HNLF spool possessing the parameters contained in Table 5.1 and an average ZDW of 1562.7 nm. The target gain level (>20dB) and 3-dB equalized bandwidth (>110nm) could not be reached. Next, the 245m HNLF spool was scanned using the non-destructive localized dispersion measurement technique reported in [113]. The spool was then segmented into four 50m sections and a single 45m section (‘section 1’ in Fig. 1). The global ZDW of each section was measured by noise injection method [114] and agreed well with the 1.6m-resolution map as shown in Figure 5.1.

Table 5.1: Simulation parameters for the two HNLF spools.

Symbol	**Description**	**HNLF 1**	**HNLF 2**
L	Length	175 m	245 m
β_4	Fourth-order dispersion coefficient	2 x 10^{-56} s^4/m	2 x 10^{-56} s^4/m
S	Dispersion slope	0.026 ps/nm^2/km	0.026 ps/nm^2/km
γ	Nonlinear coefficient	16 $W^{-1}km^{-1}$	14 $W^{-1}km^{-1}$
$\alpha_{HNLF\text{-}HNLF}$	HNLF-to-HNLF splice loss	0.05 dB	n/a
α	HNLF guiding loss	1.0 dB/km	1.0 dB/km

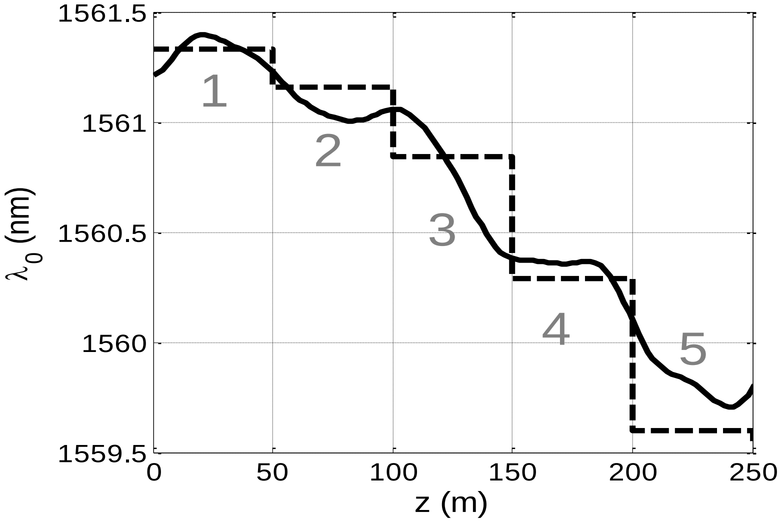

Figure 5.1: Longitudinal ZDW variations for HNLF 2; dashed line – dispersion map obtained by destructive noise injection method; solid line – dispersion map obtained by non-destructive measurement.

The parametric response of all possible combinations of the five HNLF sections was simulated using the HNLF parameters in Table 5.1 and the continuous dispersion map in Figure 5.1. The parametric gain was numerically simulated for all possible permutations for the five segments (10!/2 permutations) and some of the results are shown in Figure 5.2. None of the possible permutations could reach the target performance. The same concatenation search was performed on any four of the five segments and the target performance could not be reached. Finally, the concatenation search on any three segments revealed that the segment concatenation 1-2-3 (in that exact order and orientation) would meet the targeted gain and bandwidth performance. The simulation results are plotted in Figure 5.3.

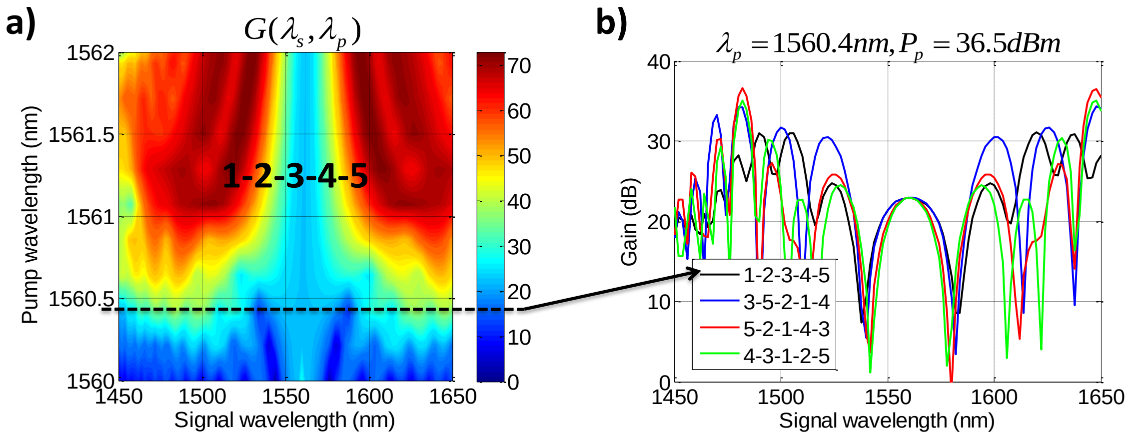

Figure 5.2: (a) Numerically simulated gain for segment concatenation 1-2-3-4-5 at a fixed pump power of 36.5 dBm; (b) Simulated gain for several different segment concatenations at a fixed pump wavelength of 1560.4 nm.

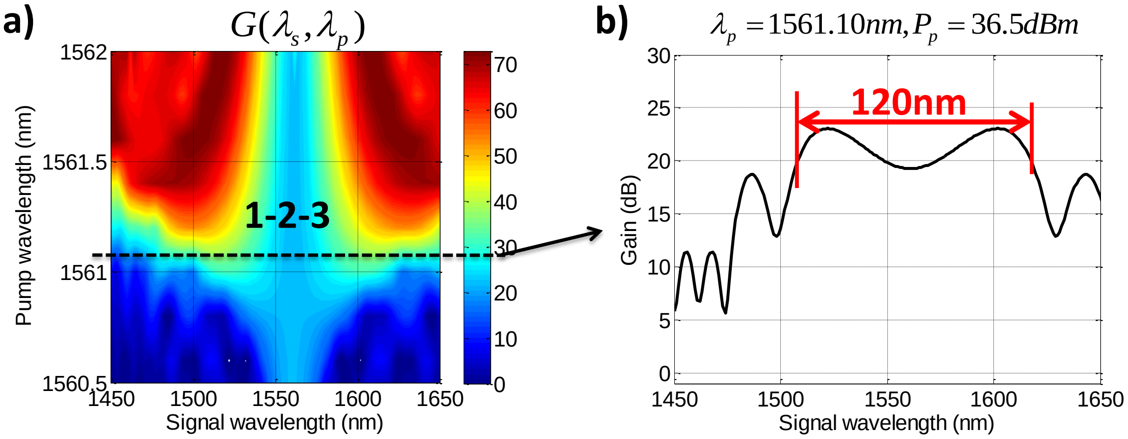

Figure 5.3: (a) Numerically simulated gain for segment concatenation 1-2-3at a fixed pump power of 36.5 dBm; (b) Simulated gain for several different segment concatenation 1-2-3 at a fixed pump wavelength of 1561.1 nm.

5.2.2 **Experimental results and discussion**

A one-pump parametric experimental setup was constructed as shown in Figure 5.4. The pump laser (TLS1) was dithered by two cascaded phase modulators driven by a pseudo-random bit sequence (PRBS) in order to suppress stimulated Brillouin scattering (SBS) in the given HNLF sample. The pump and signal waves were combined and inserted into HNLF. The pump power into HNLF was 36.5dBm, while the signal power was maintained at -30dBm level over the entire wavelength scanning range, ensuring unsaturated amplifier operation. Gain measurement was automated, with observed repeatability of less than 0.1dB. Each measurement swept signal lasers (TLS2 & TLS3) in 2nm increments, and was combined with precise polarization control in order to compensate for signal-pump polarization misalignment during the procedure.

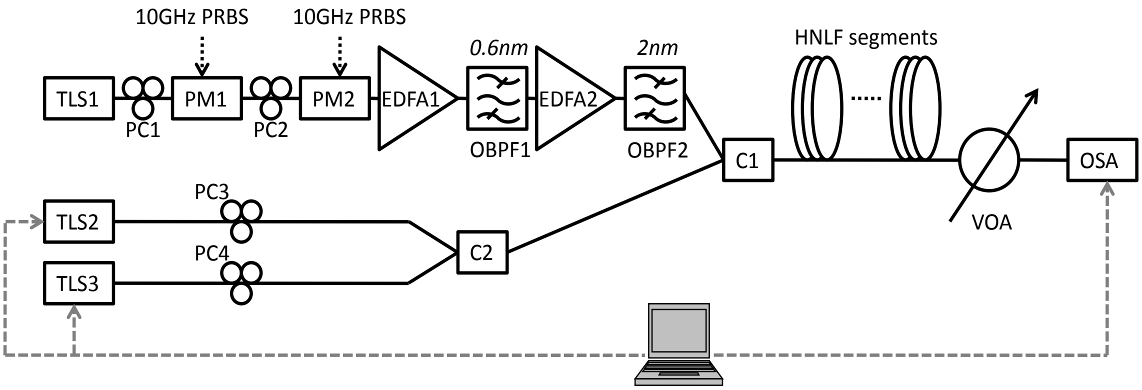

Figure 5.4: Experimental setup for FOPA gain measurement. Acronyms: TLS – tunable laser source, PC – polarization controller, PM – phase modulator, EDFA – Erbium-doped fiber amplifier, OBPF – optical band-pass filter; C – combiner, OSA – optical spectrum analyzer.

The parametric gain response of the 175m HNLF spool was measured at several pump wavelengths as shown in Figure 5.5. The spectral response did not meet the target performance for 3-dB equalized bandwidth. However, the spectra in the middle (shown as black circles in Figure 5.5) show 20 dB average gain with 4-dB equalized bandwidth of 140nm, which represents a record result for 4-dB equalized bandwidth.

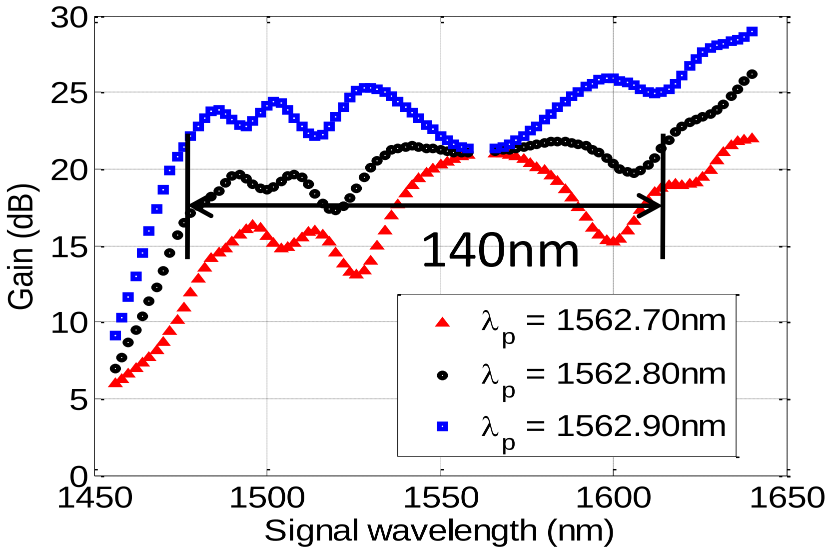

Figure 5.5: Measured gain spectra for 175m long HNLF.

As stated above, HNLF2 was subsequently substituted by a shorter spool which was subject to the dispersion mapping measurement and was purposely parted into five segments. As predicted by the simulations, the widest equalized parametric gain was indeed obtained for segment concatenation 1-2-3 and is shown in Figure 5.6(a). The pump wavelength was optimized to provide the widest 3-dB equalized bandwidth. The solid line shows the predicted gain spectrum using the dispersion map in Figure 5.1, while the dashed line indicates the predicted spectrum with the assumption of constant average ZDW. Due to a low ZDW variation of the 1-2-3 segments' combination, an excellent agreement is observed between the measurement and both simulation curves. In order to illustrate the importance of an accurate dispersion fluctuation map, the parametric gain response of the segments 3-4-5 was measured (Figure 5.6(b)). For this segment concatenation, the assumption of constant ZDW predicts a gain response identical to the 1-2-3 sectioning. Meanwhile, the dispersion fluctuation map predicts that the latter segment combination will not be useful for 3-dB equalized gain synthesis (solid line in Figure 5.6(b)) and is in very good agreement with the experimental curve.

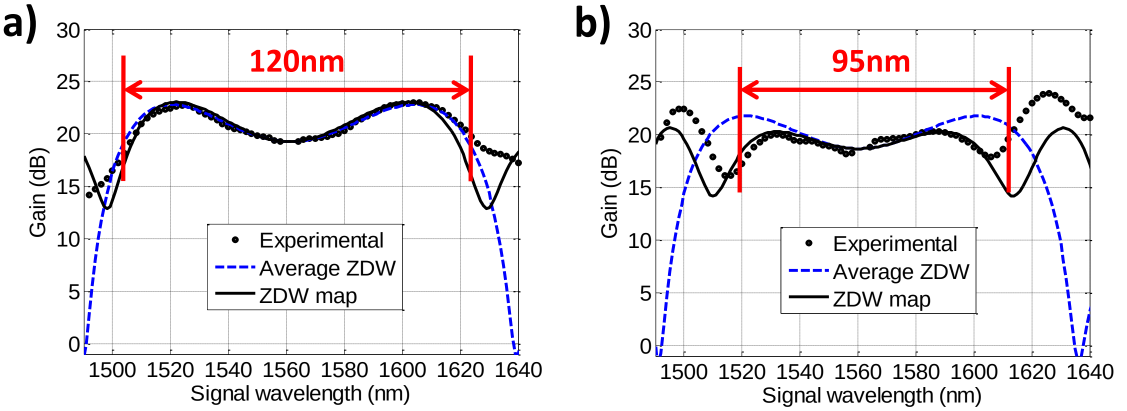

Figure 5.6: (a) Measured and simulated gain spectra for HNLF segments 1-2-3; pump wavelength was 1561.225 nm; (b) Measured and simulated gain spectra for HNLF segments 3-4-5; pump wavelength was 1560.290 nm.

The results presented above provide the first strict experimental demonstration of the importance of accurate dispersion variation measurements along a given HNLF spool as an enabling method for the precise selection of appropriate HNLF segments in the construction of parametric amplifiers with desired spectral characteristics. Of even more practical importance is the fact that the optimal re-ordering of single HNLF subsections can result in parametric devices of superior characteristics, thus representing an additional degree of freedom in gain synthesis previously unavailable to the designer.

5.2.3 **Gain sensitivity to pump wavelength positioning**

It is well-known that chromatic dispersion in optical fiber exhibits temperature dependence [115]. The ZDW temperature dependence of 0.062nm/°C was measured for HNLF [116] and it has important consequence for one-pump device operation. Indeed, synthesis of high and flat parametric gain in one-pump parametric process requires that the pump be positioned very close to the average ZDW, where the gain is very sensitive to pump wavelength detuning [117]. Figure 5.7 shows the effect of the detuning of the pump wavelength on the measured parametric gain spectrum – a 0.05nm shift results in nearly 40% of bandwidth reduction. The sensitivity to pump wavelength positioning in one-pump devices is simply addressed by temperature stabilization of the HNLF coil. It should be noted, however, that the gain thermal stability can be inherently resolved by employing a two-pump parametric architecture [60].

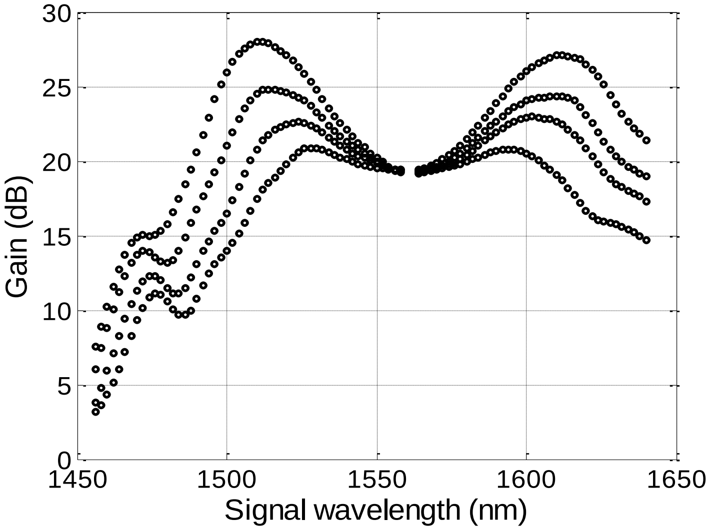

Figure 5.7: Measured parametric gain for segments 1-2-3 with pump detuned in steps of 0.05 nm.

5.3 Sensitivity studies of record high-gain two-pump FOPAs

Due to the ultrafast nature of Kerr nonlinearity and parametric gain's inherent sensitivity to instantaneous pump power, minute pump amplitude fluctuations can cause large amplitude and phase fluctuations of the amplified signal and the converted idler waves in fiber-optic parametric amplifiers (FOPAs) [77]. Necessarily, in a well-designed FOPA, low relative-intensity-noise (RIN) pump lasers are employed in order to minimize the effect of the pump transferred noise, which tends to dominate the noise performance at high input signal powers. At low input signal powers (less than -30dBm), the amplified quantum noise (AQN) is the dominant source of impairments [77]. Since AQN shares the same origin as amplified spontaneous emission (ASE) in Erbium-doped fiber amplifiers (EDFAs), FOPA noise properties are expected to be very similar, if not identical, to those of EDFA's at low input signal levels.

As amplified signal(s)/idler(s) powers in FOPAs approach those of the pump(s), significant amount of pump depletion can take place with strong dependence on the phase mismatch among the propagating waves [118, 119]. The impact of pump depletion on error performance of amplitude- and phase-modulated signals at high (greater than -30dBm) input signal powers has been studied previously [120]. The pattern-dependent pump depletion was found to drastically deteriorate the performance of amplitude-shift-keyed (ASK) signals, whereas non-return-to-zero phase-shift-keyed (NRZ-DPSK) modulation format was found to deteriorate considerably less. Owing to finite modulation extinction ratio, the pump depletion in ASK signaling causes the logical zeros to experience higher gain than the ones, resulting in the inevitable eye closure. It is not surprising, therefore, that the uniform power envelope signals will exhibit higher resilience to pump depletion effects.

At low input signal powers, the pump depletion by AQN makes for an additional source of amplitude and phase noise in the parametric device. To the best of authors' knowledge, no comprehensive study of this phenomenon has been published to date. In effect, the beginning of pump depletion by AQN is considered to be the onset of the supercontinuum generation and complete loss of amplifier functionality.

A one-pump FOPA with 70dB gain has been experimentally demonstrated previously [121]. However the signal integrity in [121] was not addressed due to the inefficient pump phase modulation impeding the retention of the information fidelity. To the best of our knowledge, the highest FOPA gain that was accompanied by performance characterization was 37dB in a single-pumped architecture [122].

In this work, we will report experimental investigations into the sensitivity of very-high-gain two-pump FOPAs. In Sec 5.4.1, the experimental setup for the constructed high-performance parametric amplifier will be shown. The bit-error-rate (BER) performance of a FOPA with small-signal gain in excess of 65 dB (with gain exceeding 60 dB over 21nm) will be characterized for 10.7-Gb/s NRZ-DPSK and RZ-DPSK modulation formats [123] in Sec. 5.4.2, in order to demonstrate the effect of signal envelope variation on the performance in an extreme amplification regime. Lastly, in Sec. 5.4.3, we will demonstrate superior performance of a two-pump amplifier with respect to the state-of-the-art EDFA in a low-input-power regime for the first time. A parametric amplifier with 50dB gain will be shown to outperform the EDFA by 1.5dB at FEC threshold level for a 10.7-Gb/s RZ-DPSK format.

5.3.1 **Experimental setup**

The two-pump parametric apparatus was constructed as shown in Figure 5.8. The external cavity lasers used for the two pumps were tuned to 1535.8 nm and 1589.1 nm and amplified to 5.1 W and 1.8 W, respectively. The optical signal-to-noise ratio (OSNR) of the amplified pump waves was measured to be 50.1dB and 50.2dB, respectively. The pump lasers were spectrally broadened via phase modulation driven by a 1.4GHz- bandwidth RF noise source in order to suppress stimulated Brillouin scattering (SBS). The amplifier noise was filtered using a cascade of high-extinction optical band-pass filters. The role of the filters was to ensure that the amplifier was seeded by quantum noise and not by unfiltered amplifier noise (sometimes referred to as 'pump residual noise' [77]) that would have undoubtedly compromised its performance, and the achievable gain. The amplified pump waves were combined with the signal path and launched into a 175m-long HNLF coil. The HNLF had a zero-dispersion wavelength of 1562.7 nm, a dispersion slope of 0.026 ps/nm^2-km, and nonlinear coefficient, γ, of 16 W^{-1}km^{-1}. An external cavity laser with a 50kHz linewidth was tuned to 1558 nm and modulated to create the signal. Two modulation formats were tested: (i) NRZ-DPSK employing a single phase modulator, and (ii) RZ-DPSK employing a phase modulator and an amplitude modulator carver, both at 10.7Gb/s data-rate.

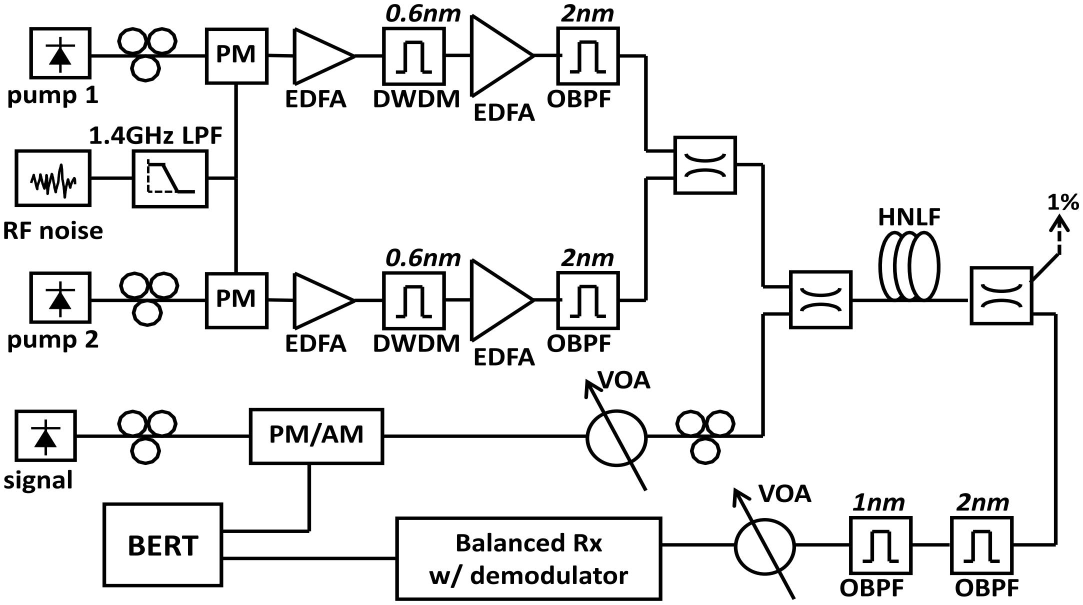

Figure 5.8: Experimental setup for dual-pumped FOPA gain and bit-error-rate measurement. Acronyms: EDFA – Erbium-doped fiber amplifier, LPF – low-pass (RF) filter, PM – phase modulator, AM – amplitude modulator, DWDM – dense wavelength division multiplexer, OBPF – optical band-pass filter, VOA – variable optical attenuator, BERT – bit-error-rate tester.

The amplified phase-modulated signal was filtered, demodulated, and detected using a balanced receiver before being passed onto the bit-error-rate tester (BERT). The input power into the balanced receiver was kept constant in order to decouple the amplifier performance from the clock-recovery circuits and the detector characteristics, whose input power response/requirements are known to affect BER measurements. We believe that the authors in [122] were able to measure improved performance of their particular parametric amplification scheme simply by increasing the input power level into the optical receiver, thereby mistakenly attributing the performance improvement to the parametric amplifier rather than their particular detection scheme.

In addition to the FOPA, a three-stage EDFA was constructed for purposes of performance comparison versus the parametric amplifier. The EDFA had a small signal gain of 50 dB and noise figure of 4 dB. The EDFA gain and noise figure were measured by the ‘optical source-subtraction method’ outlined in [124].

5.3.2 BER performance of a 66dB-gain two-pump FOPA

The spectrum of the small-signal gain of the constructed two-pump FOPA was measured and is shown in Figure 5.9(a). The peak gain was measured at 1560nm, whereas the gain exceeded 60 dB over 21 nm, resulting in a record 6.9 EHz ($6.9\text{x}10^{18}$ Hz) average gain-bandwidth product in a lumped phase-insensitive fiber optic amplifier reported to date. Next, the input signal power into the amplifier was varied, and the parametric gain measured as depicted in Figure 5.9 (b). We note that the parametric gain was partially saturated throughout the signal power tuning range.

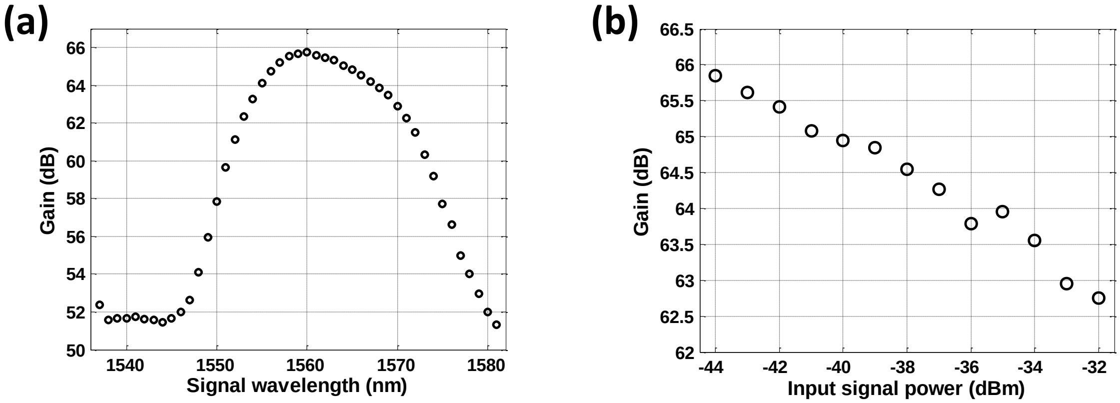

Figure 5.9: (a) Measured FOPA gain spectrum; (b) Measured FOPA gain vs. input signal power at signal wavelength of 1558nm.

BER performance of the 65dB-gain two-pump FOPA and the 50dB-gain state-of-art EDFA were measured and the results are shown in Figure 5.10. In case of the EDFA, the RZ-DPSK modulation format shows a sensitivity improvement of approximately 2dB at the BER of 10^{-9} over the NRZ-DPSK. We note that these findings are consisted with those reported in [123].

The very-high-gain two-pump FOPA was able to reach errorless performance for the NRZ-DPSK modulation format. The sensitivity penalty of 4.5dB, with respect to the benchmark EDFA measurement, was measured at the reference BER level of 10^{-9}. It should be noted, however, that the slope of the NRZ-DPSK FOPA performance curve suggests an onset of an error floor formation at higher input signal powers. The measured phenomenon is therefore consistent with the dominant role of pump transferred noise at increased input signal powers [77].

In sharp contrast, the RZ-DPSK modulation format was unable to reach errorless performance in the same parametric amplifier, the superior performance (at a lower gain) notwithstanding. As demonstrated in Figure 5.10, at low input signal powers, the RZ-

DPSK format outperforms its NRZ counterpart in both FOPA and EDFA. However, at higher input signal powers, the RZ-DPSK performance in FOPA is deteriorated by both the pump transferred noise and the pump depletion noise. The pump depletion noise originates in the format's inherent non-constant power envelope due to the RZ carving.

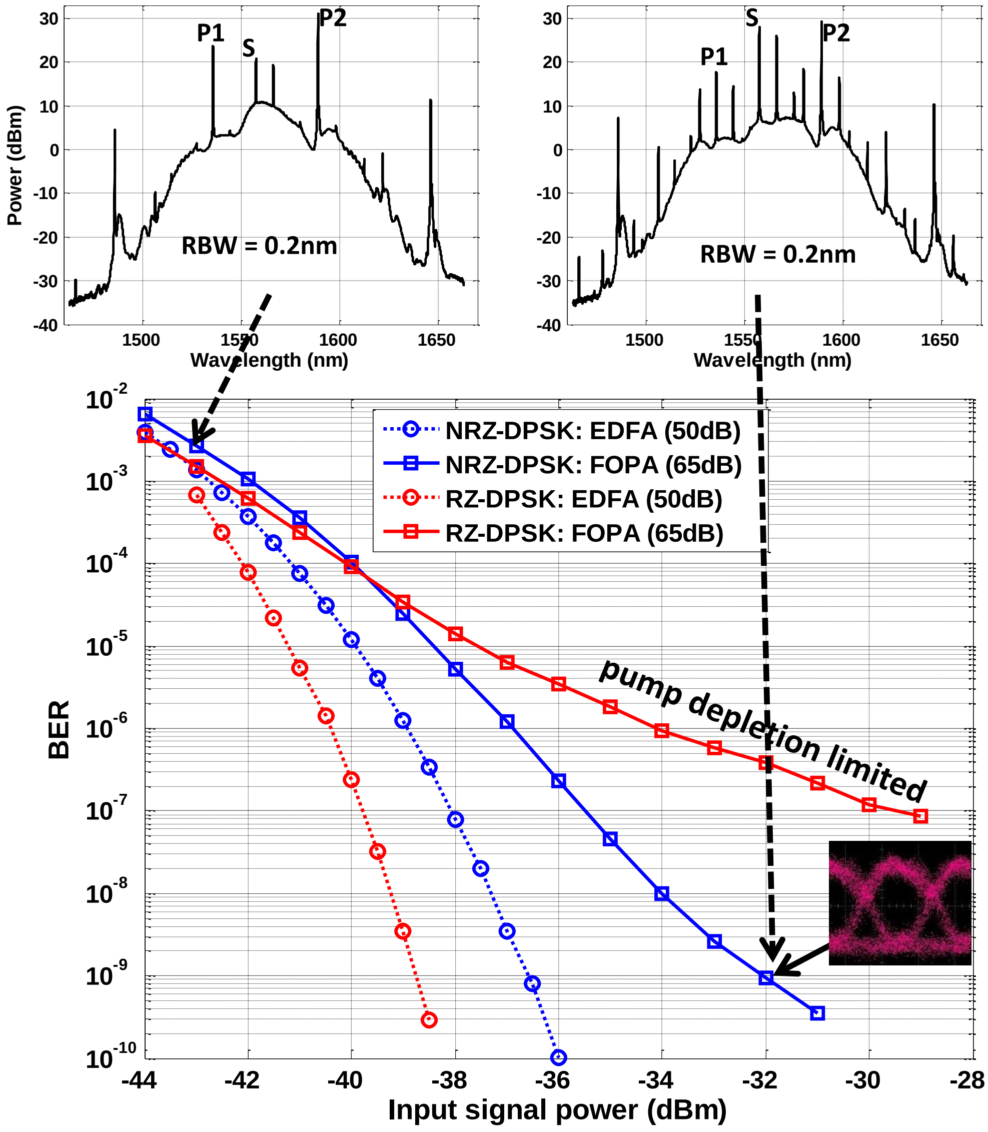

Figure 5.10: Bit-error-rate performance of 50dB-gain EDFA and 65dB-gain two-pump FOPA for the two different PSK formats. The optical spectra belong to the RZ-DPSK two-pump FOPA at input signal power of -43dBm (left) and -32dBm (right). Acronyms: P1 – pump 1; P2 – pump 2; S – signal.

We note that pump depletion can also occur due to the constant signal power envelope (as in the case of NRZ-DPSK format in this work) as well as due to energy transfer from the short-wavelength pump to the long-wavelength pump via stimulated Raman scattering. As a result, the depleted pump becomes susceptible to further depletion by AQN. Note, however that in the experiment reported in this work, the two PSK formats performed quite differently. Hence, it is reasonable to conclude that the BER performance was not dominated by AQN-induced pump depletion but rather by signal power dependent pump depletion.

5.3.3 **Low-noise-figure phase-insensitive two-pump FOPA**

The two-pump FOPA having small-signal gain of 50 dB was constructed by employing the same experimental setup as described in Sec. 5.4.1 and reducing the C- and L-band pump powers to 5.0 W and 1.0 W, respectively. An example spectrum following optical amplification is shown in Figure 5.11(a), while the spectrally-dependent measured small-signal gain is depicted in Figure 5.11(b).

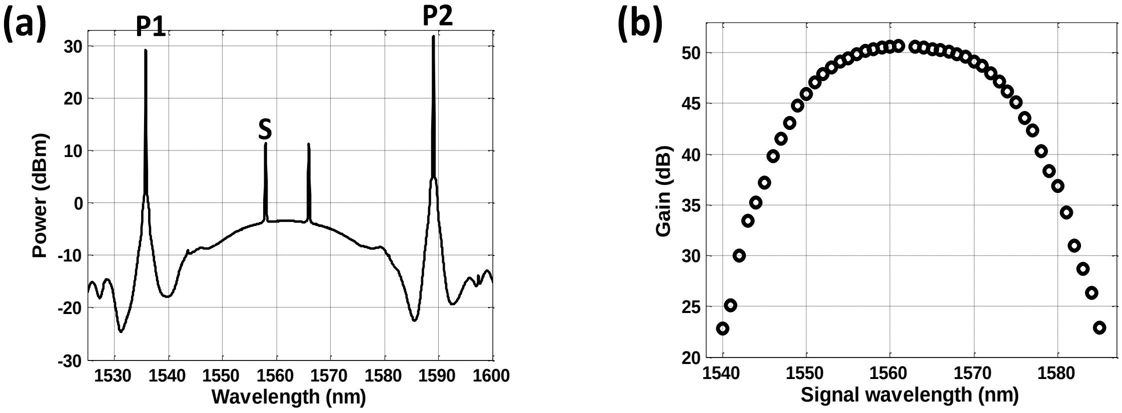

Figure 5.11: (a) Measured optical spectra for RZ-DPSK two-pump FOPA at input signal power of -35dBm; the optical spectrum analyzer resolution bandwidth was 0.2nm. Acronyms: P1 – C-band pump, P2 – L-band pump, S – signal; (b) Measured FOPA gain spectrum.

The BER performance of the 50dB-gain two-pump FOPA as well as the 50dB-gain EDFA for 10.7-Gb/s RZ-DPSK modulation format is shown in Figure 5.12. As pointed out in [77], FOPA performance is ultimately limited by the pump relative intensity noise (RIN) transfer onto the signal (the converted idler properties were not considered in this investigation). Hence, there exists a different slope of the FOPA BER curve (ultimately leading to error floor formation). As observed from the results displayed in Figure 5.12, FOPA showed 3.1 dB of sensitivity penalty at BER of 10^{-9} (with respect to the EDFA). Of particular interest for transmission applications, however, at BER of 10^{-3}, the FOPA exhibited 1.5 dB of sensitivity improvement over its inverted-population counterpart.

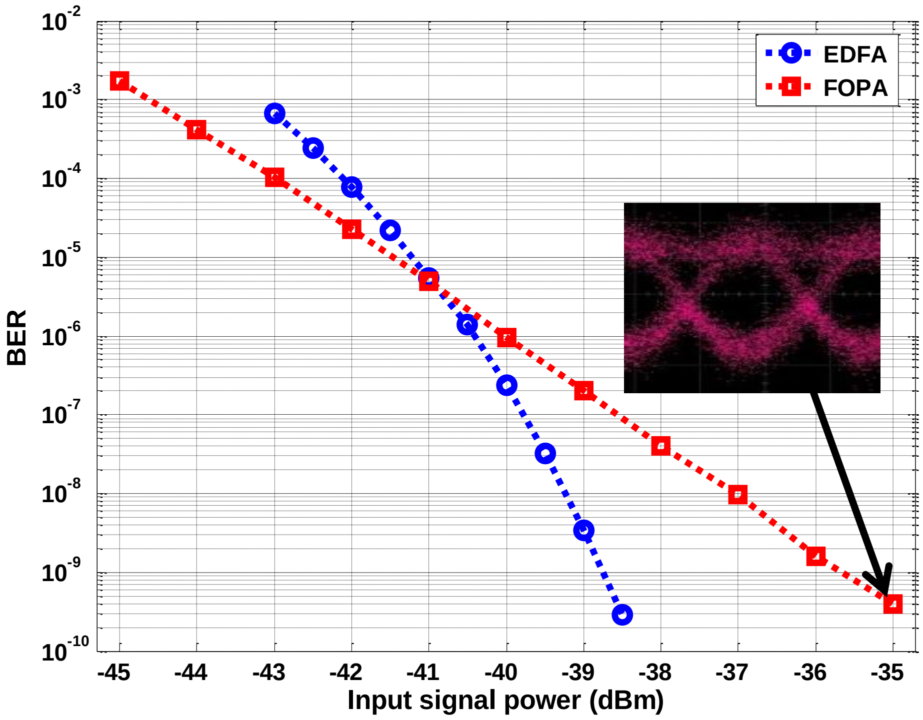

Figure 5.12: BER performance of the 50dB-gain two-pump FOPA and 50dB-gain EDFA for RZ-DPSK modulation format.

Although theoretically predicted long ago, to the best of our knowledge, this result represents the first experimental demonstration of a superior phase insensitive FOPA performance at high BERs with respect to the EDFA. Although in the current work, the FOPA is polarization sensitive, high gains can easily be reached in a polarization-insensitive architecture [125]. Most importantly, however, this demonstration clearly states FOPA's applicability to low signal amplification and/or the extended amplifier spaced links. The superior FOPA performance is achieved though at the expense of approximately 5 times higher pump power dissipation.

5.4 NIR-to-SWIR wavelength conversion

The distant wavelength conversion relies on the second phase matching region in positive-β_4 nonlinear fiber used in this work, with phase matching bandwidth that is directly proportional to the product $\gamma \times P$ and inversely proportional to β_4 as well as the cube of the pump-signal separation (see Equation (3.18)). The already narrow phase-matching region is highly sensitive to spatially localized dispersion fluctuations, which can be detrimental in the synthesis of CW conversion gain in the SWIR band even for relatively small (less than 0.2 nm) amounts of ZDW variations. To illustrate this, we constructed a one-pump parametric wavelength converter as shown in Figure 5.13.

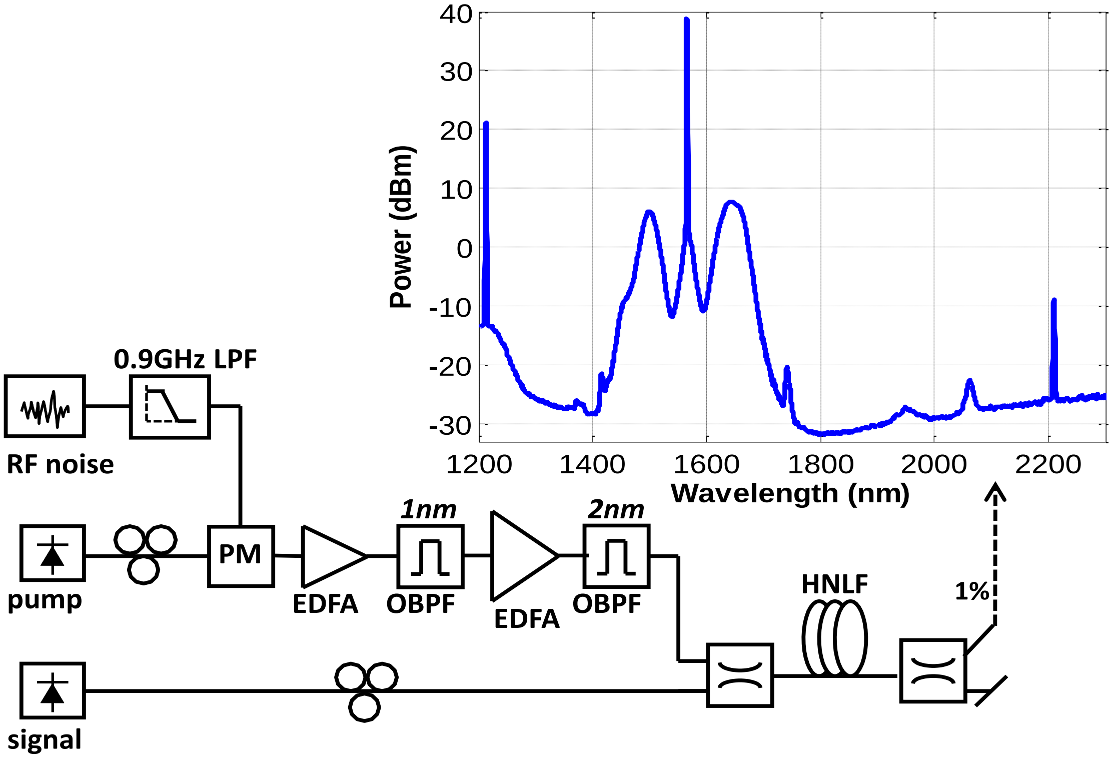

Figure 5.13: Experimental setup a distant continuous-wave wavelength converter; Inset: Optical spectrum following wavelength conversion of 1212nm-signal to 2210nm-idler using a pump positioned at 1566 nm; Acronyms: EDFA – Erbium-doped fiber amplifier, LPF – low-pass (RF) filter, PM – phase modulator, OBPF – optical band-pass filter.

The pump optical wave was an external-cavity laser (ECL), tuned from 1564 to 1567 nm, which was amplified to 7 W in two EDFAs. For the signal, an ECL tunable from 1260 to 1360 nm, as well as Raman fiber laser with fixed wavelength of 1212 nm were used. The pump and signal waves were combined and sent into the first 45 m of HNLF2 (see Table 5.1). As illustrated in Figure 5.1, the nonlinear fiber had measured ZDW fluctuation of less than 0.2 nm, which was the lowest variation per unit length available in our laboratory.

The measured NIR-to-SWIR conversion gain, defined as the ratio of the input NIR signal power to the output SWIR idler power, for different pump wavelength detuning is depicted in Figure 5.14. The signal wave was tuned from 1260 to 1360 nm in steps of 0.2 nm. In the absence of ZDW fluctuations, the expected peak conversion gain is $1/4 e^{2\gamma P_p L} \simeq 32dB$. However, in the experiment, the conversion efficiency failed to reach even transparency (0 dB). The dips observed in the conversion spectrum, particularly pronounced in the 1840 – 1940 nm wavelength regime, are due to both intrinsic and impurity absorption in the doped silica fiber [126]. The conversion gain for 1212nm-signal was subsequently measured and is plotted in Figure 5.15(a), with the corresponding 2210nm-idler spectra depicted in Figure 5.15(b). The maximum conversion gain of -29.8 dB was observed at 1566 nm pump wavelength. While being undesirably low, the measured conversion efficiency is, to the best of our knowledge, still the best reported in the continuous-wave regime over such wide bandwidths on any $\chi^{(3)}$ platform.

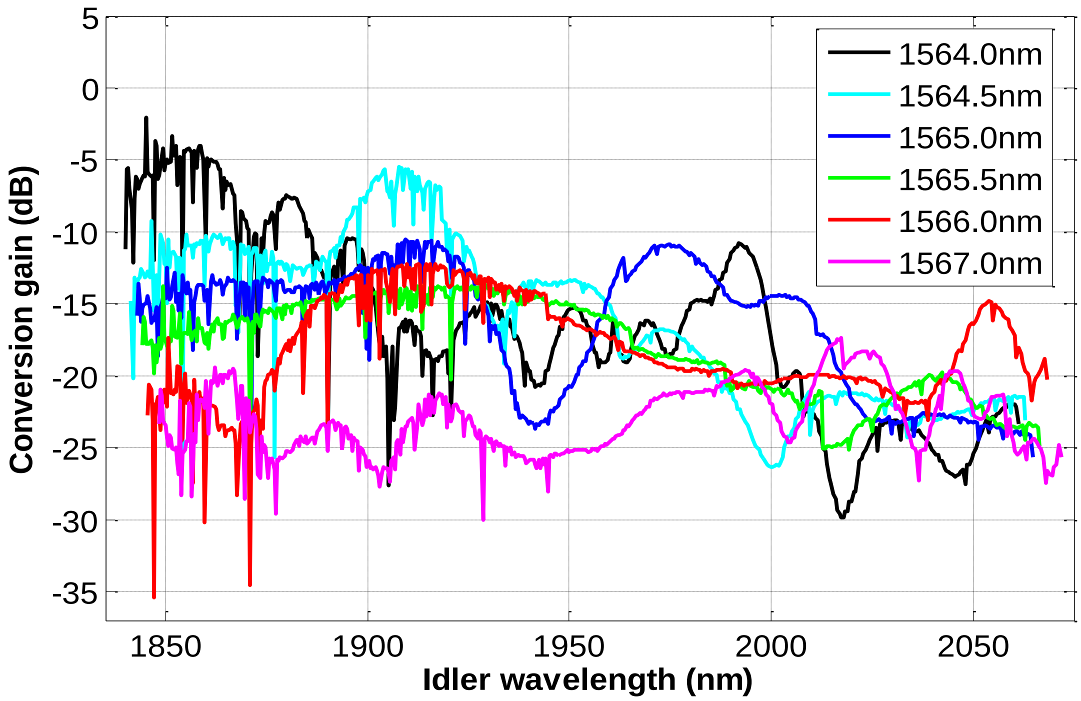

Figure 5.14: Measured NIR-to-SWIR conversion gain spectrum with different pump wavelength positioning for an NIR signal tuned from 1260 to 1360 nm in steps of 0.2 nm.

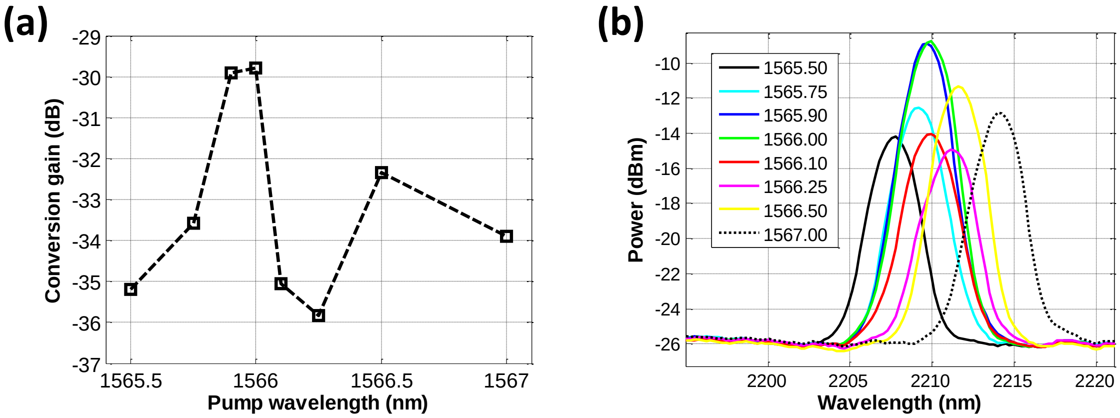

Figure 5.15: (a) Measured NIR-to-SWIR conversion gain for different pump wavelength detuning and fixed signal wavelength of 1212 nm; (b) Optical spectra of the SWIR idler at several pump wavelength positions.

5.5 Chapter summary

We have reported a record continuous-wave one-pump fiber-optic parametric amplifier with a 4-dB equalized gain bandwidth of 140nm. A new, high-resolution dispersion mapping technique enabled synthesis of target gain of 20dB with maximum ripple of 3dB over 120nm bandwidth. The design strategy included: 1) precise ZDW variation map of a long HNLF spool, 2) division of the HNLF spool into a finite segment set, and 3) identification of optimal segment ordering and its concatenation. The suboptimal choice of segmentation from identical fiber spool failed to meet targeted gain performance.

A continuous-wave two-pump fiber-optic parametric amplifier characterized by a 6.9EHz gain-bandwidth product, having a small signal gain in excess of 65dB and a gain exceeding 60 dB over 21 nm, was constructed. The construction of the very-high-gain device was followed by a rigorous performance analysis at low input signal powers (i.e. below -30dBm). The bit-error-rate measurements incorporating two different DPSK formats at 10.7 Gb/s data rate were performed and contrasted with a benchmark state-of-the art EDFA. At high BERs, the FOPA and EDFA exhibited very similar performance. As the input signal power was increased, the sensitivity penalty escalated, resulting in 4.5 dB of sensitivity penalty at BER of 10^{-9} for NRZ-DPSK modulation format. We attribute the penalty to the input signal power dependent pump transferred noise. In contrast, the FOPA amplified RZ-DPSK signal could not reach errorless performance due to pattern-dependent pump depletion owing to the format's inherent non-constant power envelope.

The presented results validate the utilization of FOPA for ultra-low signal amplification in the parameter space non-attainable by alternative amplification platforms.

The bit-error-rate performance of a 50dB-gain two-pump FOPA and a 50dB-gain EDFA were contrasted for a 10.7-Gb/s return-to-zero differential phase-shift-keyed signal. The FOPA exhibited a sensitivity penalty of 3.1dB at the BER level of 10^{-9} with respect to the EDFA. However, at the BER levels below 10^{-5}, the FOPA outperformed the EDFA with a sensitivity improvement of 1.5dB measured at the BER level of 10^{-3}, of particular interest for ASE limited links and low input power signals' amplification. In practical applications, however, the superior FOPA performance should be properly weighted/justified by its amplification efficiency.

Lastly, we have reported an experimental study of NIR-to-SWIR conversion efficiency in the continuous-wave regime. As expected from discussions in Section 2.2.4, ZDW fluctuations significantly reduce the amount of practically attainable conversion gains by orders of magnitude with respect to the performance expected for HNLFs with no dispersion variations. Conscious of these practical limitations, we pursue gain synthesis in the pulsed regime, aided by higher attainable pump powers and shorter mixer lengths.

6. Parametric gain synthesis in the pulsed regime

6.1 Introduction

As discussed in Sec. 5.4, efficient continuous-wave conversion gain synthesis in the SWIR is practically unattainable in currently available HNLF devices due to relatively small (*but still detrimental*) dispersion fluctuations. By operating in the pulsed-pump regime, shorter nonlinear mixer lengths can be used to achieve the same nonlinear phase shifts (γPL), and therefore the same amounts of parametric (conversion) gains. The decrease of the dispersive mixer length provides for increased phase-matching bandwidth and reduced sensitivity to ZDW fluctuations. To this end, a parametric transmitter and parametrically-preamplified receiver were constructed and characterized with results reported in Sec. 6.2 and Sec. 6.3, respectively.

6.2 Widely-tunable parametric transmitter for CO_2 LIDAR

In this work, a widely-tunable, cavity-less parametric transmitter operating in the SWIR wavelength range was constructed and used to detect the presence of carbon dioxide. An important aspect of this transmitter, one that cannot be overemphasized, is that it is constructed entirely of NIR components and, as a consequence, benefits from the high-quality performance and low cost of these constituent elements. The ability to remotely sense carbon dioxide is not only a good proof-of-principal experiment but is of critical importance in climate change studies, long-term weather forecasting, early forest fire detection, and global fossil-fuel combustion monitoring [127-135]. We specifically chose to probe the R30 absorption line of CO_2, centered at 2050.967 nm, because of the high contrast it exhibits with respect to problematic water vapor (see Figure 6.1) and its inherently low temperature sensitivity [136]. The results obtained in this work are in excellent agreement with absorption data obtained from the high-resolution transmission molecular absorption database (HITRAN2008) [137].

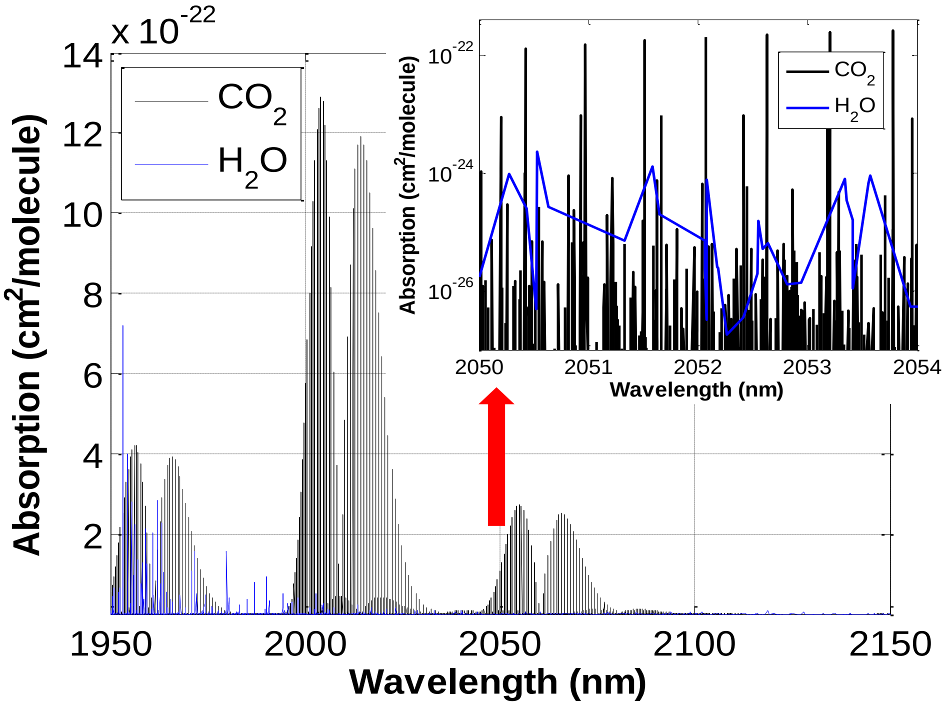

Figure 6.1: Carbon-dioxide and water absorption spectra taken from HITRAN2008 database.

6.2.1 Experimental setup

The SWIR parametric transmitter used in this work is depicted at the top of Figure 6.2. The pump source was a tunable external-cavity laser (ECL), which was amplitude modulated to produce 500-ps pulses with a 0.05% duty cycle to avoid saturation effects in the EDFAs. The modulated pump was subsequently amplified and excess amplified spontaneous emission (ASE) noise was rejected using a pair of band-pass optical filters. Another ECL, tunable from 1260 to 1360 nm, was chosen as the signal source to enable precision tuning of the signal and, as a consequence, idler wavelengths. The amplified pump pulse and continuous-wave signal seed were combined and sent into a 7-m-long HNLF with a nonlinear coefficient of 15 $W^{-1}km^{-1}$ measured using the method reported in [138]. The HNLF's zero-dispersion wavelength (ZDW) of 1583.0 nm and the dispersion slope of 0.027 ps/nm^2-km were measured using a commercial lightwave analyzer (Advantest Q7750), while the fourth-order dispersion coefficient was measured at 1.4×10^{-5} ps^4/km via the method reported in [139]. The HNLF coil used in this work was chosen because it provided the lowest available positive fourth-order dispersion. This parameter negatively affects phase-matching when the signal-to-idler's spectral separation becomes large and we therefore seek to minimize its contribution in order to permit broadband parametric gain synthesis. The left inset in Figure 6.2 depicts the optical spectrum following parametric amplification and conversion in HNLF. The pump wavelength was set to 1587.9 nm and the signal wavelength to 1295.4 nm, resulting in the 2051.0-nm idler wave at the output of the FOPC. The broadband amplified quantum noise (AQN) is present in approximately a 600-nm bandwidth around the optical pump, due to the high degree of phase matching that exists at these wavelengths. The broadband AQN can be completely done away with by employing HNLFs with negative fourth-order dispersion coefficient. However, as discussed in Chapter 1, such HNLFs are characterized by increased dispersion slopes and therefore very high sensitivity of phase-matching to local ZDW fluctuations [27]. For this reason, broadband conversion (beyond

2 μm) in these devices has not yet been reported to the best of the authors' knowledge. The pump, signal, and excess AQN were filtered out using several wavelength-division multiplexers (WDMs) and the resulting parametric SWIR source spectrum is shown in the bottom right inset of Figure 6.2.

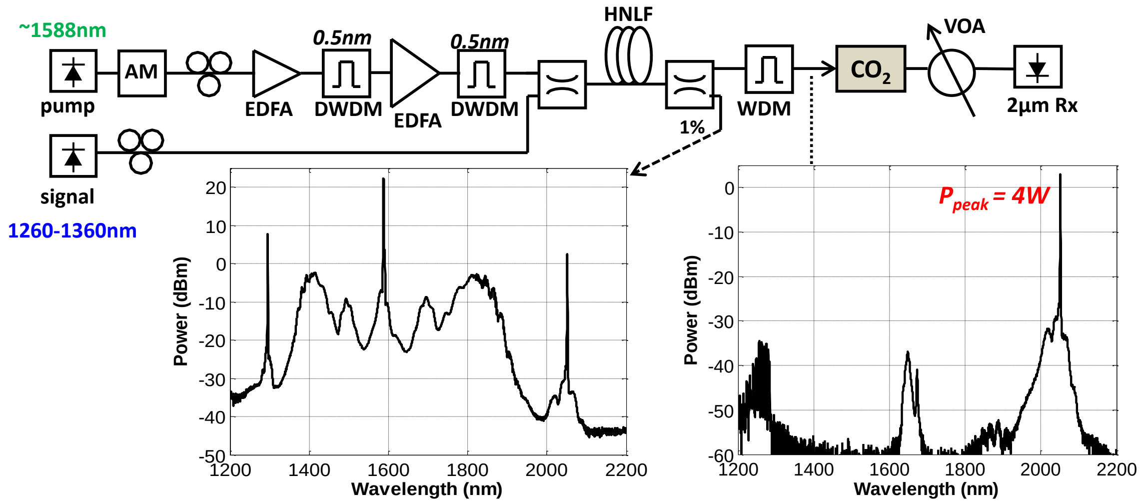

Figure 6.2: Experimental setup depicting (top) the parametric SWIR transmitter; (bottom left) the optical spectrum following NIR-to-SWIR conversion in HNLF; (bottom right) the optical spectrum following rejection of pump, signal, and excess AQN; Acronyms: AM – amplitude modulator, EDFA – Erbium doped fiber amplifier, DWDM – dense wavelength division multiplexer, VOA – variable optical attenuator, Rx – optical receiver.

6.2.2 **Results and discussion**

The measured conversion gain spectrum shown in Figure 6.3(a) for several different pump wavelength positions indicates the spectral tunability available to this source while simultaneously hinting that the spectral stability of the pump is critical for this application. The conversion gain is defined as the ratio of the output idler power to the input signal power. The pump power was set to 54.6 dBm and the wavelength detuned over approximately 4 nm in the L band, resulting in a conversion gain peak shift across a 150-nm bandwidth. The conversion gain peak can therefore be positioned arbitrarily in the SWIR band via a small detuning of the pump wavelength. In order to place the FWM peak at the R30 line of CO_2, the pump wavelength was detuned to 1587.9 nm which produced the conversion gain spectrum shown in Figure 6.3(b). The peak conversion gain of 31dB resulted in 4 W of measured idler peak power at the wavelength of 2051 nm as previously indicated in Figure 6.2 (bottom right).

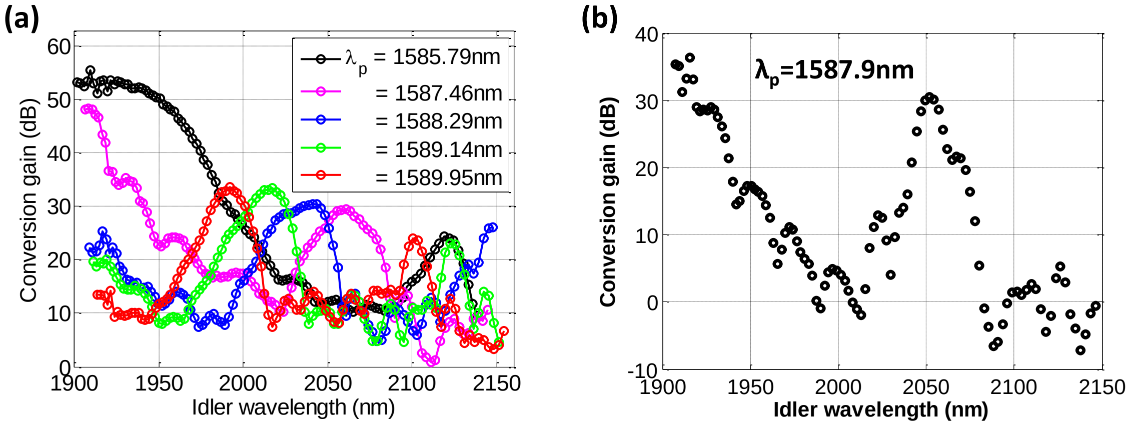

Figure 6.3: (a) Measured conversion gain spectra for several different pump wavelength positions; (b) Measured conversion gain spectrum with pump wavelength optimized for peak conversion gain at 2051 nm.

Following the rejection of pump, signal, and excess AQN by the WDMs, the idler pulse was sent through a 24-cm CO_2 cell held at a constant pressure of 600 Torr. The idler pulse was subsequently attenuated using a variable optical attenuator to miliwatt power levels acceptable for a commercially available 5-GHz bandwidth, 2-µm, extended-band InGaAs p-i-n photodetector (EOT, Inc.). By subtly changing the pump wavelength the idler was precisely tuned to the four different positions shown in Figure 6.4(a). One of the wavelength positions (color coded blue) was purposely centered off-line, while the other three were exactly positioned at three different absorption peaks.

The absorption spectrum of CO_2, obtained from the HITRAN2008 database is included in Figure 6.4(b) to show the relative strengths of the different absorption peaks. The received idler pulses corresponding to the four different wavelength positions were displayed on an electrical equivalent-time scope and are shown in Figure 6.4(c). As expected, the longer wavelength on-line idlers were attenuated more strongly by the CO_2 cell. The slope of the on-line idlers is a consequence of differential absorption due to the slight chirping of the pulse in the parametric SWIR transmitter setup. The idler's electrical SNR was measured to be in excess of 30 dB over the entire tuning range.

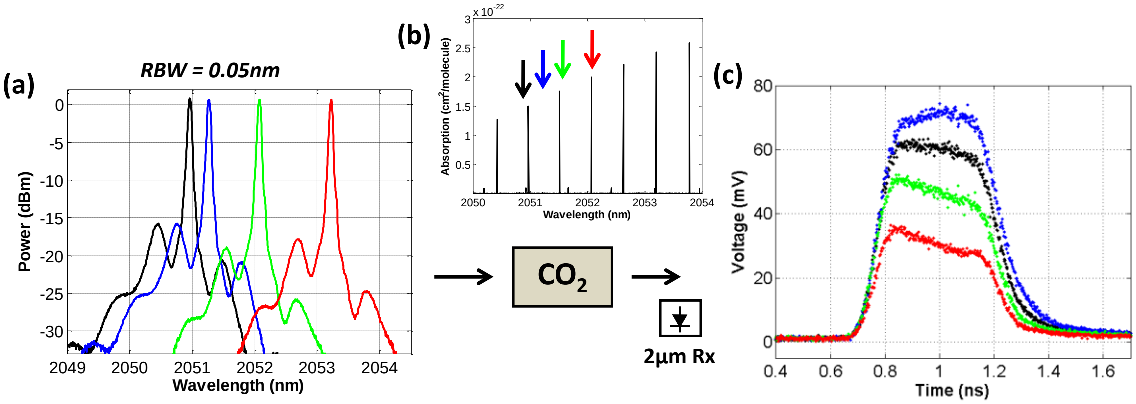

Figure 6.4: (a) Measured idler optical spectra at four different positions; (b) CO_2 absorption data obtained from HITRAN2008 database; (c) Measured idler pulses corresponding to the four different idler wavelengths shown in (a).

At this point we wish to emphasize an important benefit of using parametric SWIR transmitters which cannot be matched by conventional devices operating in the SWIR band. While the pump pulse is in its "off" state, the only photons that exist at the idler wavelength are due to zero-point vacuum field fluctuations. As a result, the SWIR idler pulse possesses a *vacuum-limited extinction ratio*. Poor pulse extinction ratios result in so-called ghost LIDAR returns which severely limit the sensing range of the system [140]. To mitigate this problem, some commercial all-fiber LIDAR technologies employ a cascade of acousto-optic modulators in order to achieve extinction ratios of more than 100 dB, which allows for an operation rage of approximately 1 km [141]. Keeping in mind that the technical requirements placed on longer range LIDAR systems grow with the square of the distance from the sensed target, the parametric conversion platform offers an inherent solution as the sensing system is never extinction-ratio-limited.

6.3 Parametrically-preamplifed SWIR receiver

The SWIR gain in low-ZDW-fluctuation HNLF (depicted in Figure 6.3) was limited to approximately 30 dB. Increasing the pump power resulted in further NIR AQN amplification and subsequent onset of pump pulse breakup via supercontinuum generation. The construction of parametrically-preamplified receiver requires optical gain of at least 40 dB (e.g. amplification/conversion of -45 dBm SWIR pulse to -5 dBm needed by NIR p-i-n photodetector). As HNLFs with lower ZDW fluctuations were not available during our work, we resorted to fibers with high dispersive fluctuations. While such fibers in principle have poorer phase matching in the NIR band (i.e. reduced AQN spectral density), high (> 40 dB) parametric amplification beyond 2000 nm can be achieved only by increasing parametric pump power. Figure 6.5 shows AQN spectra for high- (HNLF-1) and low-ZDW-variation (HNLF-2) nonlinear fibers at two different pump power levels. We see that at power level of 380 W necessary for SWIR gain synthesis using HNLF-1 (cyan), the washed-out spectral features for low-ZDW-fluctuation HNLF (magenta) are indicating the presence of supercontinuum.

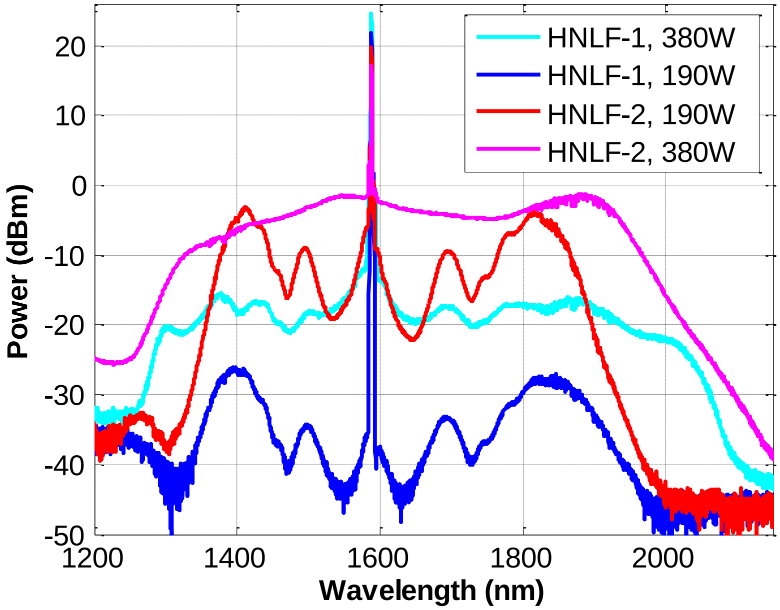

Figure 6.5: Measured amplified quantum noise spectra for high-ZDW-fluctuation (HNLF-1) and low-ZDW-fluctuation (HNLF-2) 7m-long nonlinear fibers at two different pump power levels.

A more detailed evolution of AQN spectra (which tend to closely resemble the parametric gain spectrum) with pump power is illustrated in Figure 6.6(a). Increasing the pump power leads to increased QN amplification in the SWIR band as well as distinct spectral features which can only be predicted via simulation utilizing an accurate map of ZDW fluctuation of this fiber. Unfortunately, the measurement method employed in [111] possesses longitudinal resolution of approximately 2 m and therefore cannot be used to generate an accurate ZDW map for short HNLFs. In practice, high-ZDW-variation HNLFs tend to be accompanied by increased birefringence (i.e. polarization-dependent phase matching). Consequently, the measured AQN spectra are characterized by polarization-dependent spectral features as shown in Figure 6.6(b). Hence, pump polarization can be used to tailor the spectral shape of parametric gain in birefringent nonlinear fibers.

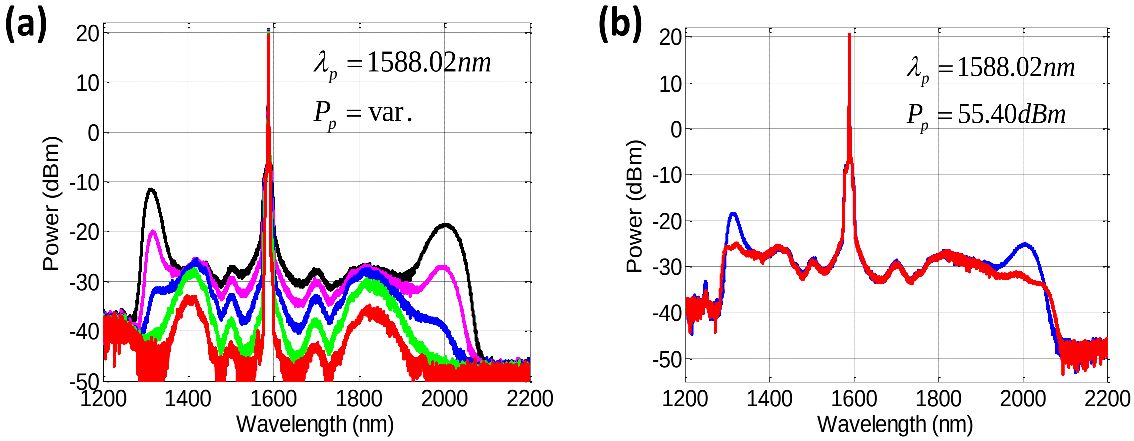

Figure 6.6: (a) Pump power dependence of AQN spectra of high-ZDW-variation HNLF (HNLF-1 in Figure 6.5); (b) Pump polarization dependence of AQN spectra due to HNLF-1's inherent birefringence.

The parametrically-preamplified SWIR receiver operating at 2015 nm was constructed as shown in Figure 6.7. A 2015-nm SWIR signal wave was provided by the parametric transmitter described in detail in Section 6.2. The idler wavelength was restricted to 1310-nm by the availability of narrowband fiber Bragg grating (FBG) optical filters. The 7m-long high-ZDW-fluctuation nonlinear fiber had the same global parameters as the one used in the transmitter setup. Following fixed parametric amplification/conversion of 40 dB in HNLF, the converted NIR idler wave was filtered with a combination of wideband (WDM) and narrowband (FBG) optical filters and detected with a 50-GHz InGaAs photodiode. A variable optical attenuator (VOA) was used to keep the optical power at the photodiode constant as the input 2015-nm signal power was varied. An electrical sampling scope with 50-GHz bandwidth was used to display the converted NIR pulse waveform and optimize the 2015-nm signal polarization prior to entering the HNLF.

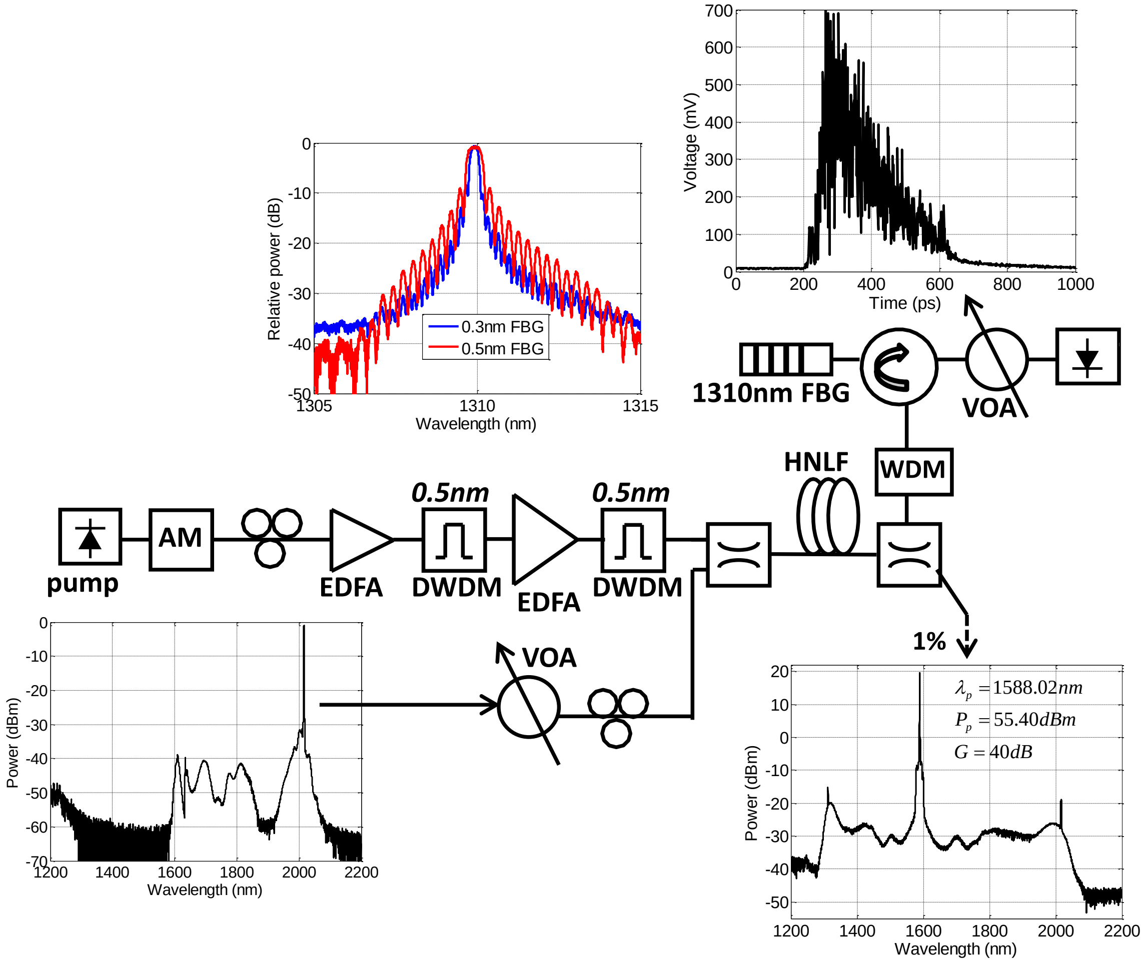

Figure 6.7: Experimental setup depicting the parametric SWIR receiver; (top left) optical transfer function of the two 1310-nm fiber Bragg gratings (FBGs); (top right) converted/amplified 1310-nm pulse waveform; (bottom left) optical spectrum of 2015-nm idler generated via a parametric transmitter described in Section 6.2; (bottom right) the optical spectrum following SWIR-to-NIR conversion in HNLF; Acronyms: AM – amplitude modulator, EDFA – Erbium doped fiber amplifier, DWDM – dense wavelength division multiplexer, VOA – variable optical attenuator.

In order to properly characterize the sensitivity of parametrically-preamplifed receiver, the 2015-nm SWIR signal power was varied prior to entering the HNLF. An optical spectrum analyzer was used to measure the optical signal-to-noise ratio (OSNR) of the converted idler wave. Meanwhile, 10,000 electrical waveforms were collected and used to compute the electrical signal-to-noise ratio (ESNR) in the middle of the slanted idler pulse. The measured OSNR and ESNR of the 1310-nm idler vs. input 2015-nm signal power are plotted in Figure 6.8. Measurement of ESNR at input signal powers below -40 dBm was limited by the electrical bandwidth of the p-i-n photodiode. Thus, a linear extrapolation of ESNR data at higher input powers was used to predict ESNR behavior in the low-input-power regime.

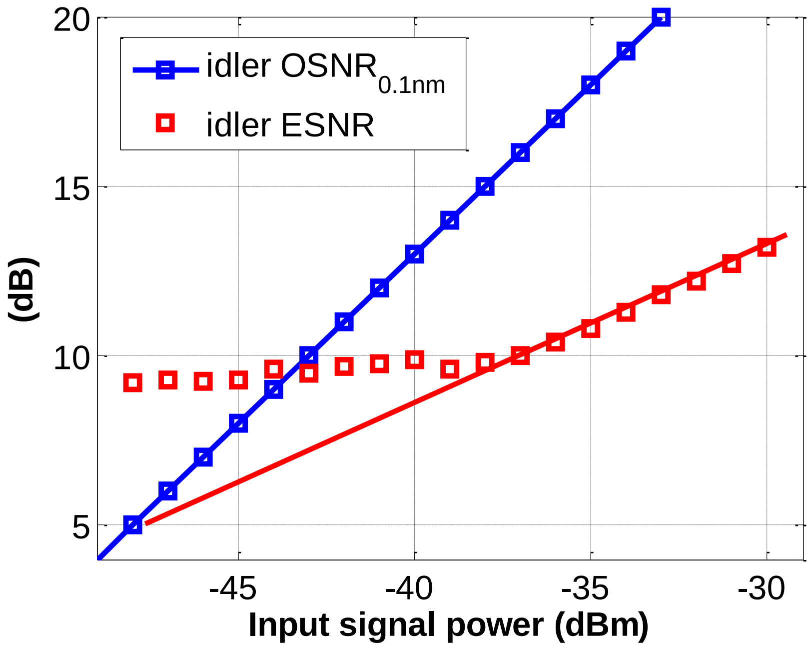

Figure 6.8: Measured OSNR and ESNR of converted 1310-nm idler vs. input signal power of 2015-nm signal

For linear optical amplifiers (e.g. EDFAs) dominated by *additive* white Gaussian noise, there exists a simple relationship relating the measured OSNR and amplifier noise figure (NF) [24]:

$$OSNR_{0.1nm}(dB) = 58 + P_{in}(dBm) - NF(dB). \tag{5.4}$$

We can therefore infer NF of 5 dB from the measured OSNR data of the SWIR parametric amplifier. Note that this is only 2 dB higher than the theoretical limit of 3 dB for phase-insensitive amplifiers! However, as discussed in Chapter **Error! Reference source not found.**, parametric amplifiers can have a significant *multiplicative* noise component due to Kerr-mediated noise transfer from the pump to the signal and idler wave. The pump transferred noise (PTN) increases with input signal power [77], leading to a reduction in the slope of the ESNR curve with respect to the OSNR curve in Figure 6.8. One way of reducing the PTN effects would be utilization of an even less noisy pump source than the one employed in our work. Unfortunately, we did not have access to such a source. A more practical solution would involve reduction of parametric pump power, while maintaining the same optical SWIR gain. As discussed earlier in this section, the latter could be accomplished with ultra-low-ZDW-fluctuation HNLF, which we also did not have access to.

6.4 Chapter summary

In this work, carbon-dioxide trace detection has been demonstrated for the first time using a continuously tunable parametric SWIR transmitter. Although this device has obvious implications for DIAL-type systems, we found it had a sufficient margin to operate even without relying on a differential-detection scheme. Clearly such a scheme can be used to further improve its performance in the future.

The transmitter utilizes a dispersion-engineered highly-nonlinear fiber platform for efficient wavelength conversion from NIR to SWIR band while using conventional NIR components. By precisely controlling the pump wavelength position the conversion gain spectrum was accurately tuned to probe a number of absorption lines of carbon dioxide in this proof-of-concept demonstration. Overall we feel this platform offers a practical way to leverage the benefits of advanced NIR technology for sensing and spectroscopy in the poorly-developed SWIR band. Moreover, the all-fiber design represents a significant advancement in terms of portability, stability, and cost when compared to existing SWIR technologies.

The synthesis of spectrally arbitrary conversion gain in the SWIR band used in the demonstration of widely-tunable transmitter provided means for highly-sensitive optically-preamplified detection. To this end, a parametrically-preamplified receiver operating at 2015 nm was demonstrated and characterized. The parametric device provided optical gain in excess of 40 dB accompanied by phase- and amplitude-preserving conversion to the NIR band. The receiver performance was limited by necessity for utilization of high-ZDW-fluctuation nonlinear fiber mixer, which demanded higher pump powers thereby increasing the so-called *pump transferred noise*.

7. Accessing mid-wave infrared: mixing in non-silica glass fibers

7.1 Introduction

Silica-based HNLFs have benefited from sharing the same material platform as low-loss single mode fibers developed for long-haul fiber-optic telecommunications, as losses below 1 dB/km around 1550 nm are routinely achieved [27, 142]. The mature fabrication platform provides for this low-loss, precision dispersion-engineered, nonlinear mixer media to have no equal in the near-infrared wavelength band. Unfortunately, extending the conversion bandwidth into the mid-wave infrared (MWIR) is fundamentally limited by exponentially increasing infrared absorption loss as well as some specific OH absorption bands [142, 143]. By combining NIR attenuation data for SMF [142] with more recently published MWIR data [144], and scaling the attenuation spectrum such that minima correspond to 1 dB/km, we obtain the HNLF attenuation spectrum depicted in Figure 7.1. As can be seen from the graph, the attenuation of approximately 1 dB/m is expected at 2450nm. This is in excellent agreement with measurement of 0.6 dB/m at 2400 nm recently reported in [145]. Due to the high GeO_2 doping of the HNLF core, the onset of exponential infrared absorption depicted in Figure 7.1 is slightly right-shifted compared to that of pure silica [146].

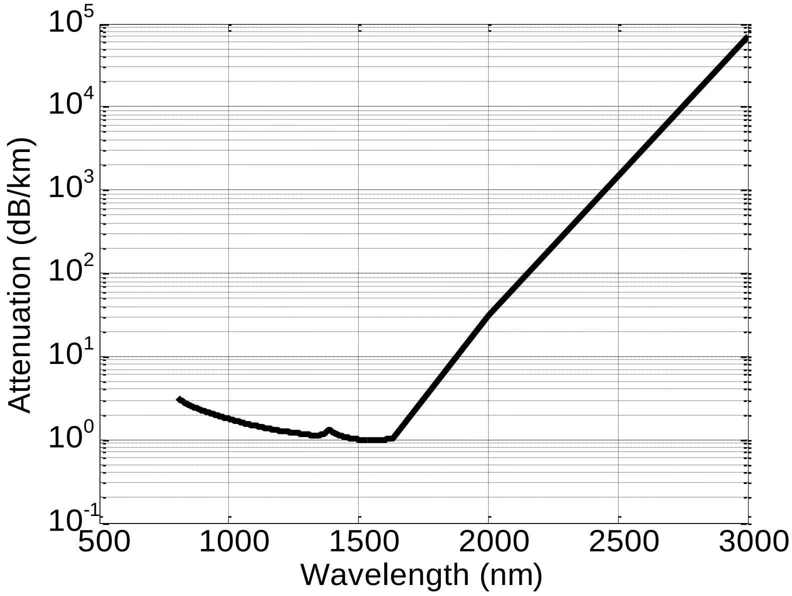

Figure 7.1: HNLF attenuation vs. wavelength.

In this Chapter, we will explore the possibility of using non-silica glass fibers for parametric wavelength conversion from NIR/SWIR into MWIR. Section 7.2 will provide an overview of material platforms, with focus on the transmitting window and Kerr nonlinearity. In Section 7.3, we will propose nonlinear mixing in weakly-guiding single-mode IR fibers, where waveguide dispersion is dominated by intrinsic material dispersion. The mixing process in this case is not impacted by detrimental waveguide dispersion fluctuations typical of dispersion-engineered high-confinement fibers (e.g. HNLFs), which are expected to be even higher for considerably less mature IR fiber fabrication technologies. Telluride and ZBLAN single-mode fiber platforms will be proposed for phase-matching Er/Tm and Yb/Er wavelength bands in order to generate MWIR light. Finally, in Section 7.3.1, rigorous numerical model will be used to calculate expected conversion efficiency for ZBLAN single-mode mixing platform.

7.2 MWIR-transmitting glass fibers

The interest in MWIR transmitting fibers has grown considerably over the last two decades with numerous emerging applications: power delivery for laser surgery; power delivery for laser cutting and welding; magnetic, current and acoustic sensing; environmental pollution monitoring using absorption, evanescent, or diffuse reflectance spectroscopy; IR imaging and countermeasures; laser threat-warning systems; and so on [147]. At the near-infrared end of their optical transparency window, MWIR fibers are eventually plagued by either multi-photon absorption or the onset of disorder-assisted electronic transitions (so-called Urbach tail) [148]. In order to utilize powerful NIR pump sources in FWM-based MWIR source synthesis, two-photon absorption (2PA) in these fibers must be completely avoided and three-photon absorption (3PA) may also need to be taken into consideration. In Table 7.1, selected IR transmitting fiber platforms are summarized along with their respective transmission windows and relative importance of three–photon absorption (3PA) at 1550nm. The material platforms are heavy-metal fluoride glass (ZBLAN – $ZrF_4 : BaF_2 : LaF_3 : AlF_3 : NaF$), tellurite multi-oxide glasses (Nb_2O_5-TeO_2), and chalcogenide glasses (As_2S_3 and As_2Se_3). The references for linear and nonlinear optical properties are also included in the table. As an example of typical loss performance, the spectral attenuation profile of commercially-available single-mode ZBLAN fiber [149] is plotted in Figure 7.2.

Table 7.1: Candidate non-silica glasses for MWIR light generation.

	ZBLAN	**Nb_2O_5-TeO_2**	**As_2S_3**	**As_2Se_3**
α < 1dB/m	1 - 4.5 µm	1 - 3.5 µm	1 – 6 µm	1 – 9 µm
3PA	No	No	Small	Significant
Reference	[149]	[150]	[151, 152]	[152,153]

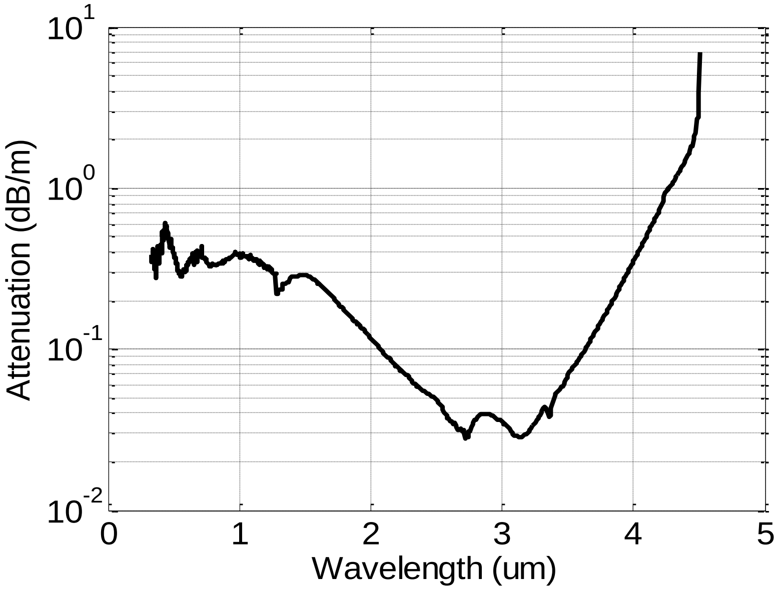

Figure 7.2: Attenuation of single-mode ZBLAN fiber.

At the long wavelength end, the intrinsic absorption is dominated by multi-phonon excitations; these are overtones and combinations of the far-infrared fundamental vibration frequencies that occur via coupling of individual imperfectly harmonic phonon modes via various mechanisms in the glass matrix [154, 155]. The long-wavelength transmitting fibers also tend to have either low Sellmeier energy gaps and/or high optical oscillator strengths, and therefore increased linear refractive index compared to that of SiO_2 [156-158]. To illustrate this trend, the index of refraction for glass platforms listed in Table 7.1 is plotted on the horizontal axis of Figure 7.3. The nonlinear index, n_2, characterizing the third-order susceptibility, is shown on the vertical axis of the same figure. The nonlinear index scales as $n^5d^2/E_s{}^2$, where n is the linear refractive index, d is the nearest-neighbor bond length, and E_s is the Sellmeier energy gap. The above dependence was theoretically predicted by the bond-orbital theory for ionic crystals [159], and found to be hold quite well for oxide and chalcogenide glasses [160-162].

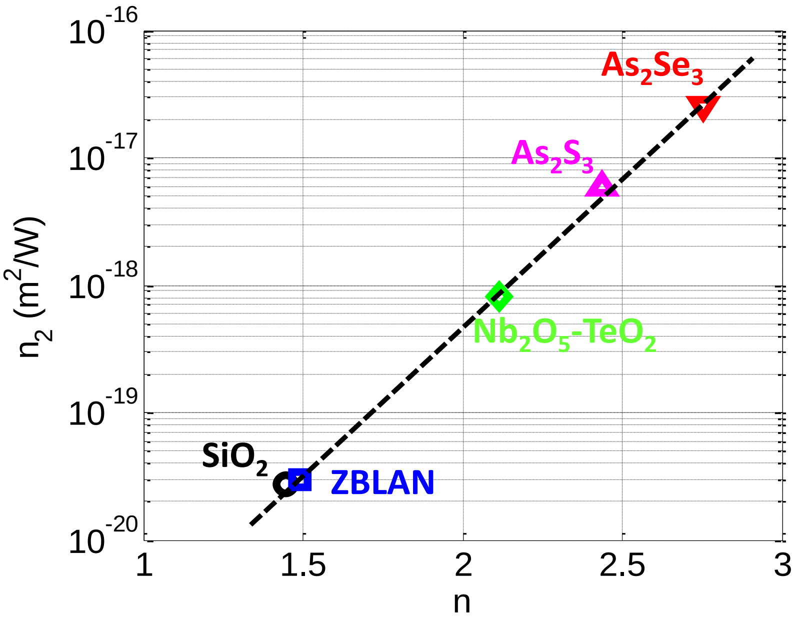

Figure 7.3: Nonlinear vs. linear refractive index of selected MWIR transmitting glasses at the wavelength of 1550nm.

The high nonlinear index of chalcogenide glasses is attributed to long anion-cation bond lengths, and therefore high polarizability, of the material. A good approximation to the dispersion of the linear refractive index is given by [163]

$$n^2(\lambda)-1=\frac{E_dE_s}{(E_s)^2-\left(hc/\lambda\right)^2} \tag{5.5}$$

where E_s is the Sellmeier gap energy and E_d is the electronic oscillator energy responsible for the Kerr effect. By differentiating Eq. (5.5) with respect to the wavelength and keeping only the leading-order terms in the expansion, we arrive at a simple expression for material dispersion:

$$D(\lambda) = -\frac{\lambda}{c}\frac{d^2 n}{d\lambda^2} \simeq -\frac{3h^2 c}{\lambda^3 n(\lambda)}\frac{E_d}{E_s{}^3} \tag{5.6}$$

From Eq. (5.6), we come to expect high-n_2 glasses, characterized by high dispersion energies and low Sellmeier gap energies, to also be highly dispersive at NIR wavelengths. Using Sellmeier coefficients for MWIR fibers from references in Table 7.1, and Silica dispersion data from [93], intrinsic material dispersion is calculated and plotted in Figure 7.4. As expected, tellurite and chalcogenide glasses are highly dispersive in the near-infrared wavelength regime. The ZBLAN fiber, with material zero-dispersion wavelength at 1650nm, exhibits very low material dispersion over wide wavelength range. This behavior is attributed to the fact that fluorides, as a class, posses the largest Sellmeier gaps of any anion [160].

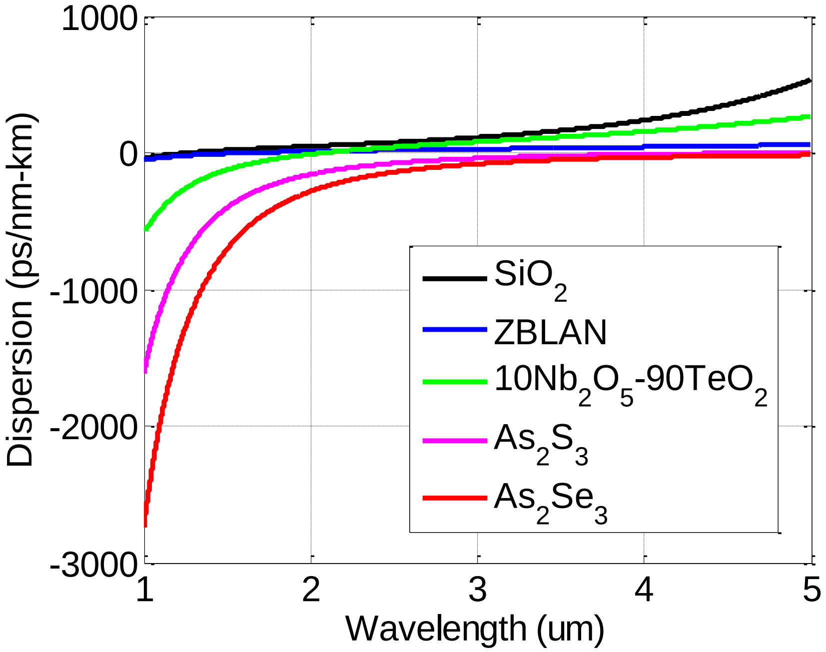

Figure 7.4: Material dispersion of selected MWIR transmitting glasses and silica.

7.3 Phase-matching via material dispersion

As discussed in Chapter 2, phase-matching over wide bandwidths in any $\chi^{(3)}$ nonlinear media is highly-sensitive to localized dispersion fluctuations. The dispersive variations tend to be pronounced in high-confinement structures (such as PCFs, Si waveguides, and silica-based HNLFs to some degree), where the group refractive index dispersion is dominated by index-profile-dependent waveguide dispersion. The waveguide dispersion is used to tailor the overall group index dispersion such that the nonlinear medium's zero-dispersion wavelength (ZDW) is positioned in the spectral bands where powerful and cost-effective pump sources exist (e.g. YDFA and EDFA band in the NIR). The sensitivity to core size fluctuations can be achieved via loosening of confinement and index profile re-engineering. However, even on the mature silica fabrication platform, waveguide designs exhibiting increased dispersion robustness can be quite complex and difficult to fabricate [164]. The MWIR glass platforms are far less advanced and it is therefore unreasonable to expect low-dispersion-fluctuation complex-structures to be fabricated in the near (and perhaps distant) future.

The problem of dispersion fluctuation can be avoided altogether by utilizing weakly-guided waveguides, where group index dispersion is dominated by intrinsically more stable material dispersion. The phase-matching based on material dispersion is inherently negative-β_4 type. So, the parametric pump has to be placed to the left of the material ZDW, as per discussion in Chapter 2. Out of the candidate MWIR transmitting fibers considered in this work, ZBLAN (ZDW ≈ 1650 nm) and Nb_2O_5-TeO_2 (ZDW ≈ 2050 nm) are well suited for distant wavelength conversion via Erbium (1530 -1620 nm) and Thulim (1870 – 2050 nm) band pumping, respectively. The calculated total dispersion and effective modal area for a simple SMF-type index profile ZBLAN fiber (commercially available from iRphotonics, Inc.) are shown in Figure 7.5. The 9/125 µm core/cladding radius was used along with the numerical aperature ($NA=(n_1^2-n_2^2)^{1/2}$, where n_1 is the core index and n_2 is the cladding index) of 0.18. The details of the dispersion and effective modal area calculation are outlined in Appendix C. The same calculation was performed for tellurite-based fiber (not depicted).

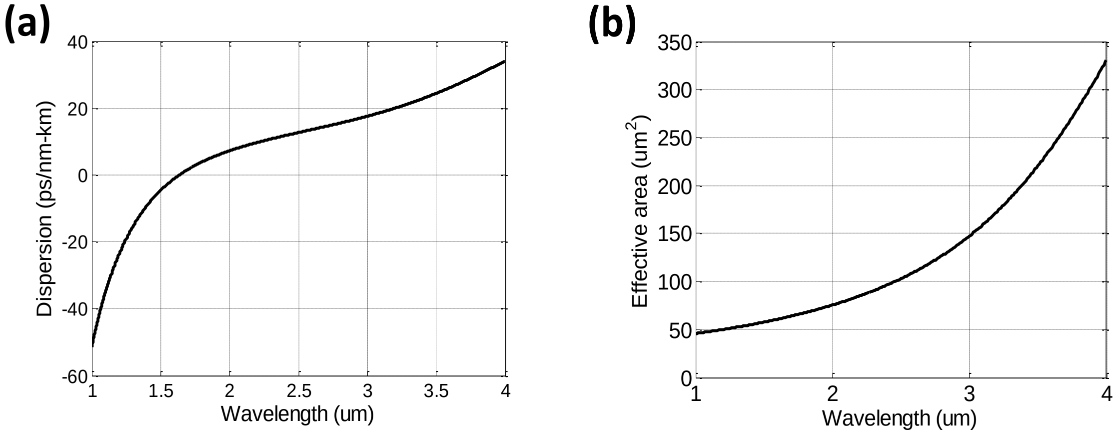

Figure 7.5: Calculated (a) dispersion, and (b) effective modal area of a single-mode ZBLAN fiber with simple (SMF-type) doping profile.

With knowledge of the dispersion of the effective index of propagation, the phase mismatch (Equation (3.2)) of the three propagating waves (pump, signal, and idler) can be calculated. The calculated phase-matched signal/idler wavelengths as well as pump/signal phase-matching contours for tellurite and ZBLAN single-mode fibers are depicted in Figure 7.6 and Figure 7.7, respectively. The tellurite single-mode platform successfully phase matches the Erbium and Thulium fiber amplifier band to generate MWIR light in the 2800-3100 nm range. The ZBLAN platform is quite a bit more interesting as it phase-matches Erbium and Ytterbium (990 - 1120 nm) - two very-well developed optical amplifier technologies. By continuous tuning of pump and signal NIR lasers over approximately 100nm (these are the bandwidths available to Er- and Yb-doped fiber amplifier technologies), the newly-created MWIR idler can be continuously tuned over 1000nm (2500 – 3500 nm).

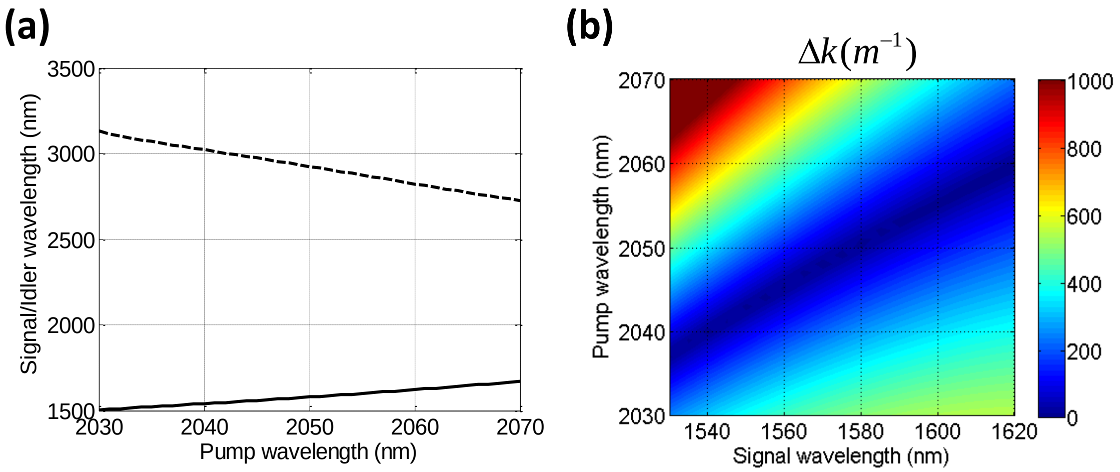

Figure 7.6: (a) Phase-matched signal/idler wavelengths, and (b) pump/signal phase-matching contours for single-mode tellurite fiber.

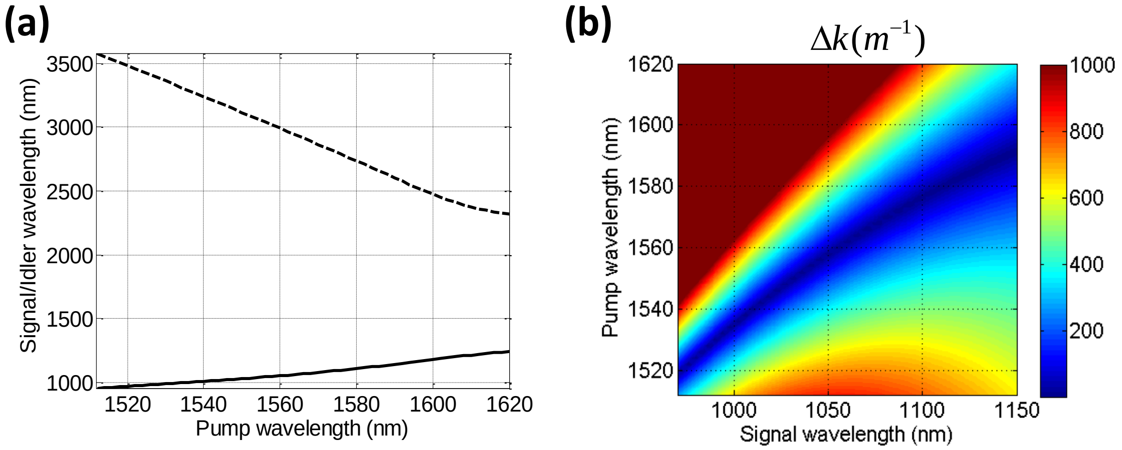

Figure 7.7: (a) Phase-matched signal/idler wavelengths, and (b) pump/signal phase-matching contours for single-mode ZBLAN fiber.

7.3.1 MWIR Conversion efficiency in ZBLAN fiber

In order to correctly estimate the expected NIR-to-SWIR conversion efficiency in single-mode ZBLAN fiber, the wavelength dependence of the attenuation (Figure 7.2), the total waveguide dispersion (Figure 7.5(b)), as well as the effective modal area (Figure 7.5(b)) must be properly accounted for. The solution is then numerically obtained by solving the nonlinear Schrödinger equation (NLSE) in the quasi-CW regime as outlined in Appendix D. The calculated signal-to-idler conversion efficiency for fixed pump wavelength of 1530 nm and signal tuned in the Ytterbium band is plotted in Figure 7.8. Pulsed-pump operation at 500 W (easily achieved in practice) and ZBLAN fiber length of 15 m were used in the calculation. The peak conversion efficiency of -5 dB of 992nm-signal was calculated at the MWIR idler wavelength of 3343 nm. The conversion efficiency is expected to improve significantly as the fabrication process is perfected and material losses are further reduced. In an ideal case (i.e. with no waveguide material losses in the simulation above), the expected parametric conversion gain is in excess of 59dB.

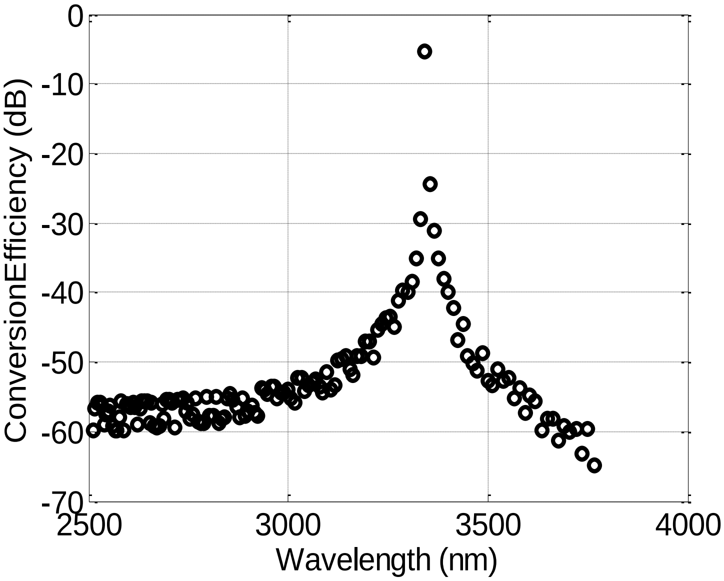

Figure 7.8: Calculated signal-to-idler conversion efficiency in single-mode ZBLAN fiber for pump wavelength position of 1530 nm.

7.4 Chapter summary

We have proposed ZBLAN and Tellurite optical waveguide platforms for synthesis of parametric gain in the MWIR frequency band. The weekly-guided non-silica platform relies on material dispersion for phase-matching of NIR/SWIR and MWIR bands, thereby minimizing the influence of waveguide-induced dispersion fluctuations. The ZBLAN material platform allows access further into the MWIR; however, it is challenged by low material nonlinearity as well as high (~0.3dB/m) waveguide losses. With current material losses, the ZBLAN platform is expected to provide parametric gain only above 1kW pump power levels. The parametric conversion efficiency is expected to increase rapidly as the fabrication process matures and material losses are further reduced.

Appendix A

Semi-analytical model for PM-to-AM in optical fiber

The semi-analytical model for conversion of phase/frequency fluctuations acquired by pump wave propagation in HNLF to amplitude fluctuations is developed according to the schematic shown in Figure A.1.

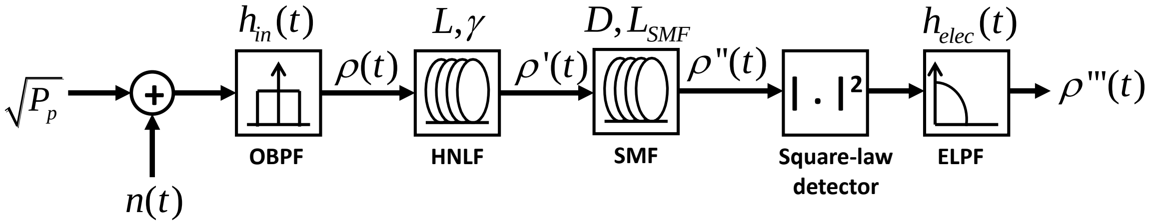

Figure A.1: Schematic for semi-analytical model of PM-to-AM in optical fiber.

Following band-pass optical filtering, the complex pump field is

$$\rho(t) = \sqrt{P_p} + n(t) \otimes h_{in}(t). \tag{A.1}$$

After propagation in HNLF, neglecting loss and depletion, the pump field acquires a nonlinear phase shift (and therefore a nonlinear frequency chirp):

$$\rho'(t) = \rho(t) \times e^{j\gamma L|\rho(t)|^2} = \rho(t) \times e^{j\phi_{NL}(t)}. \tag{A.2}$$

The optical fiber dispersion is simply treated as a phase shift in the Fourier domain:

$$\rho''(t) = \Im^{-1}\{\Im\{\rho'(t)\} \times e^{j\hat{D}(\omega)L_{SMF}}\}, \tag{A.3}$$

where $\Im\{\ldots\}$ and $\Im^{-1}\{\ldots\}$ represent the Fourier transform and inverse Fourier transform, respectively, L_{SMF} is the SMF length, and the dispersion operator is defined as [93]:

$$\hat{D}(\omega) = \frac{\beta_2(\omega_{ref})}{2}(\omega - \omega_{ref})^2 + \frac{\beta_3(\omega_{ref})}{6}(\omega - \omega_{ref})^3. \tag{A.4}$$

The β_2 and β_3 coefficients are related to the dispersion and the dispersion slope of the optical fiber and ω_{ref} is the center frequency of the optical pump wave. Following optical detection, the electrical voltage (or current) can be expressed as

$$\rho'''(t) = |\rho''(t)|^2 \otimes h_{elec}(t), \tag{A.5}$$

where $h_{elec}(t)$ is the impulse response of the optical sampling oscilloscope. Finally, the electrical SNR measured on the oscilloscope is

$$SNR = \frac{\langle \rho'''(t) \rangle^2}{\sigma^2_{\rho'''(t)}} \tag{A.6}$$

with $\langle\rangle$ and σ^2 symbolizing the mean and the variance of the acquired electrical waveform, respectively. Thus, the measurement of electrical SNR allows us to infer the amount of acquired noise-induced nonlinear chirp.

Appendix B

Raman gain measurements in HNLF

Accurate prediction of parametric amplification response in $\chi^{(3)}$ nonlinear media requires precise knowledge of the Raman susceptibility occurring at the amplified/converted wavelengths [165, 166]. The Raman scattering is also an additional source of noise in FOPAs, where the Kerr nonlinearity causes coupling of parametric amplification process to molecular vibration states at temperatures above 0 K. As a result, the amplifier/converter quantum-limited noise figure is increased beyond 3-dB and exhibits peaks at Raman gain/loss maxima [167, 168, 77]. Hence, precise measurement of HNLF Raman response is required for accurate modeling of noise properties of $\chi^{(3)}$-based parametric amplifiers.

The counter-propagating Raman gain measurement method, described in [169], was employed in characterization of 175m-long HNLF (HNLF1 in Table 5.1). The experimental setup is depicted in Figure B.1. A 1480-nm 200-mW DFB laser was used as a Raman pump. The laser wavelength, deep into the normal dispersion regime of the HNLF, was chosen in order to eliminate parametric effects in the fiber from polluting the measurement. Both the pump and the broadband noise source, which was used as a signal, were depolarized in order to eliminate effects of polarization mode dispersion (PMD) and polarization-dependent los (PDL). The counter-propagating scheme prevents

RIN transfer from pump to signal, which would cause noisy read-out measurements on the optical spectrum analyzer.

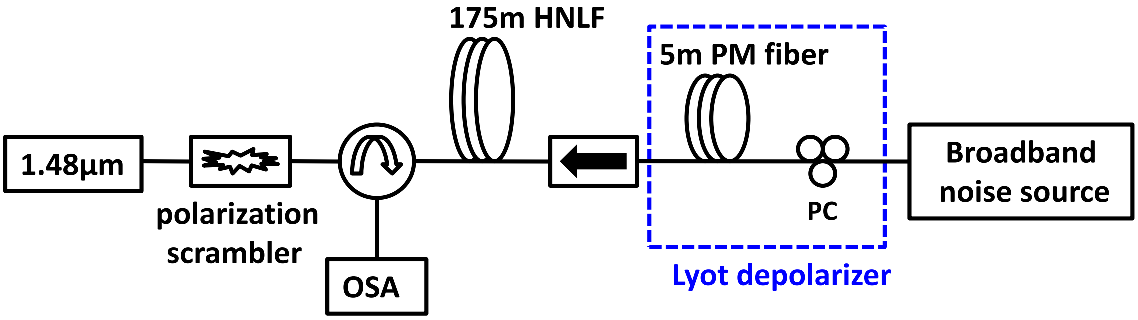

Figure B.1: Experimental setup for HNLF Raman gain/loss measurement; Acronyms: OSA – optical spectrum analyzer, PM – polarization-maintaining, PC – polarization controller.

By turning the pump and/or the broadband noise source on/off, three optical spectra are taken and Raman gain calculated from

$$g(\Delta\omega) = \frac{1}{P_p L_{eff}} \ln\left(\frac{S_{pumpON,bsON} - S_{pumpON,bsOFF}}{S_{pumpOFF,bsON}} \right), \tag{B.1}$$

where P_p is the pump power entering HNLF, $S_{pumpON,bsON}$ is the optical spectrum with both the pump and broadband noise source turned on, and similar for other spectra. The effective length, L_{eff}, is defined as $(1-exp(-\alpha L))/\alpha$, where α is the HNLF attenuation coefficient. The measured Stokes and anti-Stokes Raman gain/loss are shown in Figure B.2.

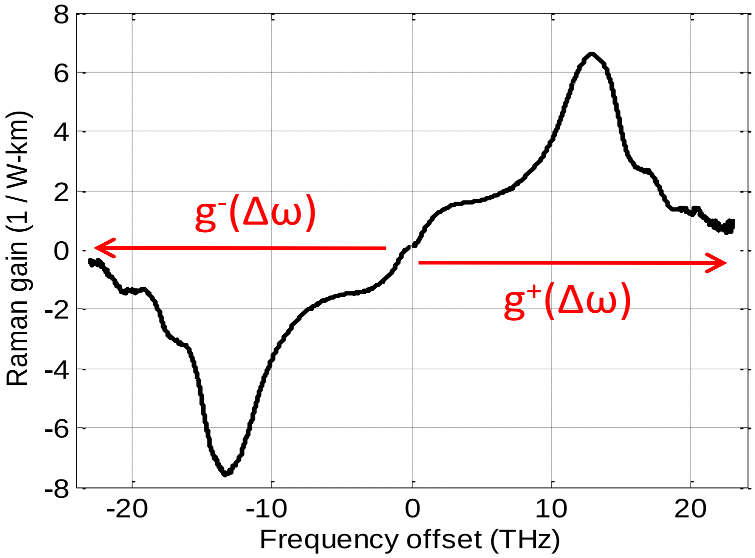

Figure B.2: Measured Raman gain/loss.

The Raman gain spectrum in all optical fibers exhibits pump wavelength dependence determined in large part by the overlap of the propagating mode with the waveguide doping profile. In FOPAs, the parametric pump is often placed in the anomalous dispersion regime in order to maximize the parametric gain bandwidth, making it impossible to measure Raman gain/loss exactly at the pump wavelength. Fortunately, pump wavelength dependence of Raman gain coefficient in most optical fibers can be determined from simple power-law scaling behavior [169]:

$$g^{+}(\omega_p, \Delta\omega) \approx {\omega_p}^{n_s} \rho(\Delta\omega) C. \tag{B.2}$$

ω_p is the pump frequency, ω_s is the signal frequency, $\Delta\omega = \omega_p - \omega_s$, n_s is the scaling factor, C is a frequency-independent constant and $\rho(\Delta\omega)$ is determined from

$$g^{-}(\Delta\omega) \approx -\frac{\omega_s}{\omega_p} {\omega_p}^{n_s} \rho(-\Delta\omega) C. \tag{B.3}$$

Then, the scaling factor n_s can be found from the asymmetry of the gain versus the loss:

$$A(\Delta\omega) = \frac{g^{+}(\Delta\omega) + g^{-}(\Delta\omega)}{g^{+}(\Delta\omega) - g^{-}(\Delta\omega)} \approx \frac{n_s + 1}{2\omega_p}\Delta\omega \tag{B.4}$$

The Raman gain/loss asymmetry of the measured 175m-long HNLF is plotted in Figure B.3. Since the asymmetry cannot be fitted by a straight line, we find that no simple pump wavelength scaling behavior exists for this particular fiber. In [169], similar behavior was observed for dispersion-compensating fibers (DCFs) and attributed to the high modal confinement characteristic of these fibers. HNLFs are characterized by even higher confinement; hence, the observed phenomenon comes as no surprise.

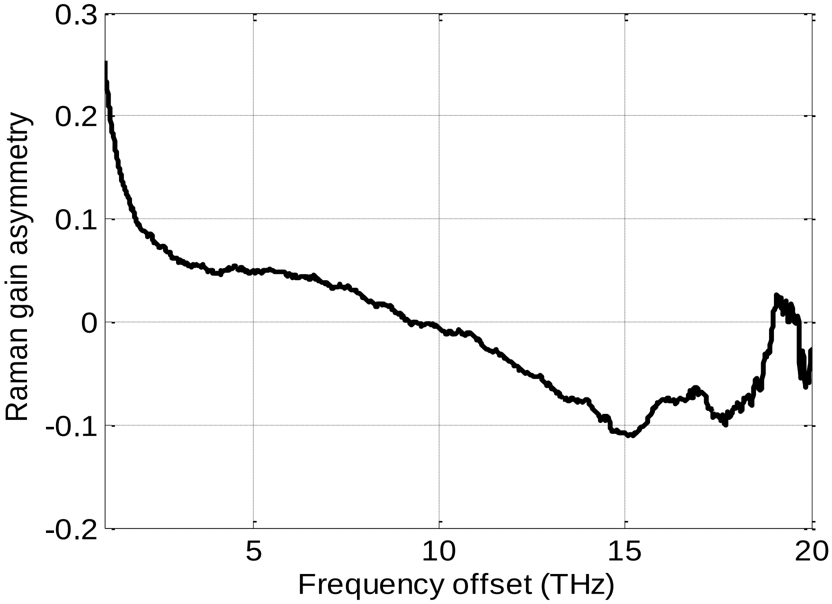

Figure B.3: HNLF Raman gain/loss asymmetry.

Approximation of spectral dependence of HNLF Raman gain coefficient can be made by simply scaling that of the standard single-mode fiber (SMF). The two gain spectra are plotted in Figure B.4. The difference in spectra is attributed in large part to the GeO_2 doping of the fiber core (~5mol% for SMF and 30mol% for HNLF), and the resulting fractional radial distribution of Si-O-Si and Ge-O-Si bridges [170].

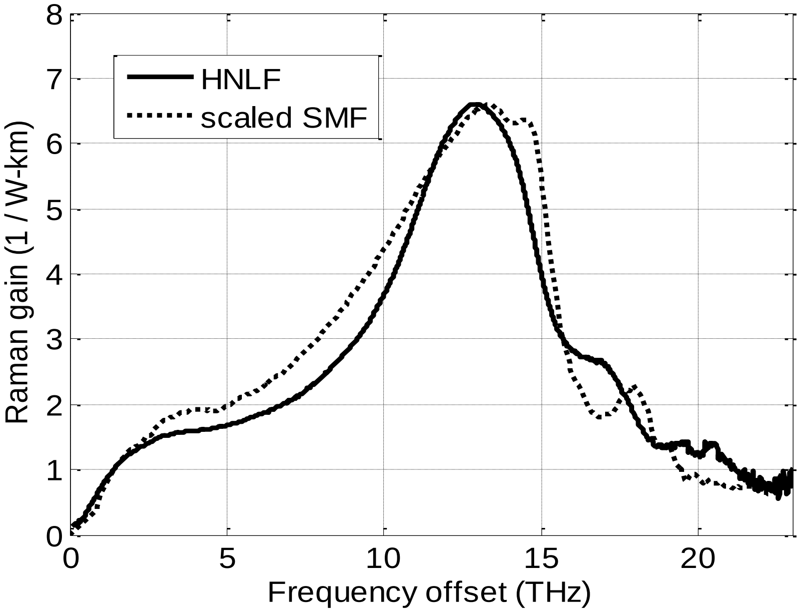

Figure B.4: Raman gain spectra of measured HNLF and scaled SMF.

Appendix C

Numerical calculation of waveguide dispersion and effective modal area

Optical properties of a cylindrically symmetric waveguides (e.g. optical fiber) can be calculated via solving the radial Helmholtz equation [171]:

$$\hat{L}E = \frac{\partial}{\partial r}\left(\frac{1}{\varepsilon(r,\lambda)}\frac{\partial}{\partial r}(\varepsilon(r,\lambda)E)\right) + \frac{1}{r}\frac{\partial E}{\partial r} - \frac{l^2}{r^2}E + \varepsilon(r,\lambda)k_0^2 E = n_{eff}^2 E. \qquad \text{(C.1)}$$

E is the mode profile, $\varepsilon(r,\lambda) = n^2(r,\lambda)$ is the radial profile of the wavelength-dependent dielectric constant, k_0 is the vacuum propagation vector, and n_{eff} is the effective index of propagation. Eq. (C.1) is solved for effective index of propagation and transverse fundamental mode profile via the finite-difference method described in [172]. The effective modal area is defined as:

$$A_{eff} = \frac{\left(\int |E(x,y)|^2\, dxdy\right)^2}{\int |E(x,y)|^4\, dxdy}. \qquad \text{(C.2)}$$

The total waveguide dispersion, D, can be found by differentiating n_{eff} with respect to the wavelength:

$$D(\lambda) = -\frac{\lambda}{c}\frac{\partial^2 n_{eff}(\lambda)}{\partial \lambda^2} = \frac{-2\pi c}{\lambda^2}\beta_2(\lambda). \qquad \text{(C.3)}$$

The dispersion slope is related to n_{eff} by

$$S(\lambda) = -\frac{1}{c}\left(3\frac{\partial^2 n_{eff}(\lambda)}{\partial\lambda^2} + \lambda\frac{\partial^3 n_{eff}(\lambda)}{\partial\lambda^3}\right). \tag{C.4}$$

Finally, the fourth-order dispersion coefficient is computed from S and D by the following relation:

$$\beta_4(\lambda) = \frac{\pi\lambda^4}{12c^3}\left(6D(\lambda) + 6\lambda S(\lambda) + \lambda^2\frac{\partial S(\lambda)}{\partial\lambda}\right). \tag{C.5}$$

Appendix D

Modeling light propagation and FWM in the quasi-CW regime

The propagation of light in guided, dispersive, nonlinear media is typically described by the generalized nonlinear Schrödinger equation (GNLSE) [173]:

$$\frac{\partial}{\partial z}A(t)=\left(-\frac{\alpha}{2}+\hat{D}+\hat{N}\right)A(t) \tag{D.1}$$

A(t) is the complex envelope of the propagating optical signal, α is the fiber attenuation coefficient, $\hat{D}$ is the (linear) dispersion operator, $\hat{N}$ is the nonlinear operator, and t is really the retarded time $t - z/\mathrm{v}_g$ (v_g is the pulse/field group velocity). The linear dispersive operator is defined as

$$\hat{D}=\sum_{q\geq 2}\frac{j^{q+1}}{q!}\beta_q\frac{\partial^q}{\partial t^q} \tag{D.2}$$

where β_q are the coefficients of the Taylor series expansion of the propagation vector $\beta=\left(2\pi/\lambda\right)n_{eff}$ around a specific reference frequency, ω_{ref} (usually chosen to be the pump frequency or the fiber zero-dispersion frequency). In the frequency domain, the dispersion operator is simply expressed as

$$\hat{D}(\omega)=\sum_{q\geq 2}\frac{\beta_q}{q!}\left(\omega-\omega_{ref}\right)^q. \tag{D.3}$$

The nonlinear operator has two contributions: (i) the near-instantaneous (few femtosecond) electronic (Kerr) nonlinearity, and (ii) the time-delayed molecular (Raman) scattering [174]. The expression for $\hat{N}$ thus becomes

$$\hat{\mathrm{N}}(t)A(t) = j\gamma A(t)\left((1-f_R)\left|A(t)\right|^2 + f_R A(t)\int_0^\infty h(\tau)\left|A(t-\tau)\right|^2 d\tau \right), \tag{D.4}$$

where $\gamma = n_2\omega_{ref}/cA_{eff}$ is the nonlinear coefficient, n_2 is the nonlinear index, A_{eff} is the effective modal area, f_R is the fractional Raman contribution to the total nonlinearity (~0.18 in silica fibers), and $h(t)$ is the normalized Raman response function $\left(\int_0^\infty h(\tau)d\tau = 1\right)$. Since we are interested in the FWM interaction responsible for the creation of new idlers, we restrict ourselves to the interaction of at most four optical frequencies. The complex envelope can then be expressed as

$$A(t) = A_i(t)e^{j\omega_i t} + A_j(t)e^{j\omega_j t} + A_k(t)e^{j\omega_k t} + A_l(t)e^{j\omega_l t}, \tag{D.5}$$

while obeying the energy conservation condition: $f_i + f_j = f_k + f_l$. Substituting Eq. (D.5) into (D.4), the nonlinear operator becomes:

$$\begin{aligned}
&\frac{1}{j}\hat{N}A_i(t) = (1-f_R)\gamma_{ii}\,|A_i(t)|^2\,A_i(t) + f_R\gamma_{ii}A_i(t)\int_0^\infty h(\tau)\,|A_i(t)|^2\,d\tau + \\
&2(1-f_R)A_i(t)\sum_{k\neq i}\gamma_{ki}\,|A_k(t)|^2 + f_R A_i(t)\sum_{k\neq i}\gamma_{ki}\int_0^\infty h(\tau)\,|A_k(t-\tau)|^2 d\tau + \\
&f_R\sum_{k\neq i}\gamma_{ki}A_k(t)\int_0^\infty h(\tau)A_i(t-\tau)A_k^*(t-\tau)e^{2\pi j(f_i-f_k)\tau}d\tau + \\
&(1-f_R)\sum_{j,l\neq k}\gamma_{ijkl}A_jA_k^*A_l + f_R A_j(t)\sum_{j,l\neq k}\gamma_{ijkl}\int_0^\infty h(\tau)A_k^*(t-\tau)A_l(t-\tau)e^{2\pi j(f_l-f_k)\tau}d\tau
\end{aligned} \tag{D.6}$$

The first and second term are the electronic and molecular contribution to self-induced nonlinear phase shifts known as selft-phase modulation (SPM) and intra-band Raman scattering. The third and fourth term represent the instantaneous (Kerr) and delayed (Raman) phase shifts induced on the $A_i(t)$ envelope by the other three propagating waves. The fifth term is the so-called inter-band Raman scattering. The last two terms represent Kerr-mediated FWM and coupling between FWM and Raman process, respectively.

The effective nonlinear coefficient is defined as

$$\gamma_{ijkl} = \frac{2\pi n_2 f_i}{cA_{eff}(f_i, f_j, f_k, f_l)}. \tag{D.7}$$

$A_{eff}(f_i, f_j, f_k, f_l)$ is the reciprocal to the overlap integral defined by

$$\frac{1}{A_{eff}(f_i, f_j, f_k, f_l)} = \frac{\int\limits_{-\infty}^{\infty}\int\limits_{-\infty}^{\infty}\left(\prod\limits_{p=i,j,k,l}\left|F_p(x,y)\right|^2\right)dxdy}{\prod\limits_{p=i,j,k,l}\left(\int\limits_{-\infty}^{\infty}\int\limits_{-\infty}^{\infty}\left|F_p(x,y)\right|^2 dxdy\right)}, \tag{D.8}$$

where $F_p(x,y)=F_p(f_p,x,y)$ is the mode field distribution of the mode propagating at frequency f_p. For Gaussian mode profiles, the above expression simplifies to

$$\begin{gathered} A_{eff}(f_i, f_j, f_k, f_l) = \frac{1}{4}\sqrt{A_{eff}(f_i)A_{eff}(f_j)A_{eff}(f_j)A_{eff}(f_k)} \times \\ \left[\frac{1}{A_{eff}(f_i)} + \frac{1}{A_{eff}(f_j)} + \frac{1}{A_{eff}(f_k)} + \frac{1}{A_{eff}(f_l)}\right]. \end{gathered} \tag{D.9}$$

Since we are interested in mixing of continuous-wave signals and/or relatively long pulses (>100ps), both Kerr and Raman response can be considered to be instantaneous. This allows us to eliminate the time dependence of the propagating envelopes and write the nonlinear operator in the frequency domain:

$$\begin{aligned}\frac{1}{j}\hat{N}A_i &= \left[\gamma_{ii}(1-f_R)+f_R H(0)\right]P_i A_i + \\ &+\sum_{k\neq i}\left[\gamma_{ki}2(1-f_R)+f_R H(0)+f_R H(f_i-f_k)\right]P_k A_i + \\ &\sum_{j,l\neq k}\gamma_{ijkl}A_j A_k^* A_l\left[(1-f_R)+f_R H(f_l-f_k)\right].\end{aligned} \tag{D.10}$$

$P_i=|A_i|^2$ is the power of the signal positioned at the frequency f_i, and $H(\omega)$ is the Fourier transform of the Raman response function. The Raman gain, which is measured experimentally (see Appendix B), is defined as

$$g_R(f_k,f_i)=2f_R\gamma_{ki}\,\mathrm{Im}\{H(f_k-f_i)\} \tag{D.11}$$

The real part of H can be found by invoking the Kramers-Kronig relations [49].

By using the frequency domain dispersion and nonlinearity operator, given by Eq. (D.3) and Eq. (D.11), respectively, in Eq. (D.1), the powers of propagating optical fields are quickly solved for using the split-step Fourier method (SSFM) described in [173].

References

1. M. Ebrahim-Zadeh, and I. T. Sorokina, eds., *Mid-Infrared Coherent Sources and Applications* (Springer, 2007).

2. C. Weitkamp, ed., *Lidar: Range-Resolved Optical Remote Sensing of the Atmosphere* (Springer, 2005).

3. G. Vosselman, and H.-G. Maas, *Airborne and Terrestrial Laser Scanning* (CRC Press, 2010).

4. A. Henderson, and R. Stafford, "Low threshold, singly-resonant CW OPO pumped by an all-fiber pump source," Optics Express **14**, 767-772 (2006).

5. Lockheed Martin Aculight Corporation, product Argos^{TM} 2400, website: http://www.aculight.com/.

6. E. Sorokin, I. T. Sorokina, M. S. Mirov, V. V. Fedorov, I. S. Moskalev, and S. B. Mirov, "Ultrabroad continous-wave tuning of ceramic Cr:ZnSe and Cr:ZnS lasers," ASSP, paper AMC2, San Diego, USA (2010).

7. G. J. Wagner, B. G. Tiemann, W. J. Alford, and T. J. Carrig, "Single-Frequency Cr: ZnSe Laser," ASSP, paper WB12, Santa Fe, USA (2004).

8. T. S. McComb, V. Sudesh, L. Shah, R. A. Sims, and M. C. Richardson, "Widely-tunable (>100nm) continuous-wave narrow-linewidth high-power thulium fiber laser," Proceedings of SPIE vol. 7193, SSL XVIII, San Jose, USA (2009).

9. AdValue Photonics, Inc., product: AP-Tm-P20, website: http://www.advaluephotonics.com/

10. S. Arafin, A. Bachmann, K. Vizbaras, J. Gustavsson, A. Larsson, and M. C. Amann, "Large-Area Single-Mode GaSb-based VCSELs using an Inverted Surface Relief," IEEE Photonics Society Annual Meeting, paper MI3, Denver, USA (2010).

11. M. C. Amann, "Recent progress on High-Speed and Tunable VCSELs in the 1.3 to 2.6µm Wavelength Range," CLEO, paper CME1, San Jose, USA (2010).

12. E. Geerlings, M. Rattunde, J. Schmitz, G. Kaufel, H. Zappe, and J. Wagner, "Widely Tunable GaSb-Based External Cavity Diode Laser Emitting Around 2.3µm," IEEE Photonics Technology Letters **18**, 1913-1915 (2006).

13. E. Geerlings, M. Rattunde, J. Schmitz, G. Kaufel, J. Wagner, B. Blasi, D. Kallweit, and H. Zappe, "Widely Tunable Micro-Mechanical External-Cavity Diode Laser Emitting Around 2.1µm," IEEE Journal of Quantum Electronics **44**, 1071-1075 (2008).

14. Roithner LaserTechnik, product: DFB-2050-3, DFB-2330-3, website: http://www.roithner-laser.com/

15. M. Raybaut, T. Schmid, A. Godard, A. J. Mohamed, M. Lefebvre, F. Marnas, P. Flamant, A. Bohman, P. Geiser, and P. Kaspersen, "High-energy single-longitudinal mode nearly diffraction-limited optical parametric source with 3MHz frequency stability for CO_2 DIAL," Optics Letters **34**, 2069-2071 (2009).

16. G. J. Koch, B. W. Barnes, M. Petros, J. Y. Beyon, F. Amzajerdian, J. Yu, R. E. Davis, S. Ismail, S. Vay, M. J. Kavaya, and U. N. Singh, "Coherent differential absorption lidar measurements of CO_2," Applied Optics **43**, 5092-5099 (2004).

17. Electro-Optics Technology, Inc., product ET-5000F, website: http://www.eotech.com/

18. T. F. Refaat, M. N. Abedin, G. J. Koch, S. Ismail, and U. N. Singh, "Infrared Detectors Characterization for CO2 DIAL Measurement," Proceedings of SPIE vol. 5154, 65-73 (2003).

19. T. F. Refaat, M. N. Abedin, O. V. Sulima, S. Ismail, and U. N. Singh, "III-V Compound Detectors for CO_2 DIAL Measurements," Proceedings of SPIE vol. 5887, Bellingham, WA, USA (2005).

20. A. Joshi, and D. Becker, "High-Speed Low-Noise p-i-n InGaAs Photoreceiver at 2-µm Wavelength," IEEE Photonics Technology Letters **20**, 551-553 (2008).

21. T. F. Refaat, M. N. Abedin, O. V. Sulima, S. Ismail, and U. N. Singh, "2.4-µm-Cutoff AlGaAsSb/InGaAsSb Phototransistors for Shortwave-IR Applications," IEEE Transactions on Electron Devices **54**, 2837-2842 (2007).

22. Electro-Optics Technology, Inc., product ET-4000F, website: http://www.eotech.com/

23. E. Säckinger, *Broadband Circuits for Optical Fiber Communication* (Wiley-Interscience, 2005).

24. P. C. Becker, N. A. Olsson, and J. R. Simpson, *Erbium-Doped Fiber Amplifiers: Fundamentals and Technology* (Academic Press, 1999).

25. N. K. Dutta, and Q. Wang, *Semiconductor Optical Amplifiers* (World Scientific, 2006).

26. M. E. Marhic, *Fiber Optical Parametric Amplifiers, Oscillators, and Related Devices* (Cambridge University Press, 2007).

27. M. Hirano, T. Nakanishi, T. Okuno, and M. Onishi, "Silica-Based Highly Nonlinear Fibers and Their Application," IEEE Journal of Selected Topics in Quantum Electronics **15**, 103-113 (2009).

28. S. Radic, "Parametric amplification and processing in optical fibers," Laser & Photon. Rev. **2**, 498-513 (2008).

29. J. Hansryd, P.A. Andrekson, M. Westlund, J. Li, and P.O. Hedekvist, "Fiber-based optical parametric amplifiers and their applications," IEEE J. Sel. Top. Quantum Electron. **8**, 506-520 (2002).

30. S. Radic and C.J. McKinstrie, "Optical Amplification and Signal Processing in Highly Nonlinear Optical Fiber," IEICE Trans. Electron. **EE88-C**, 859-869 (2005).

31. C.-S. Bres, N. Alic, A. H. Gnauc,, R. M. Jopson, and S. Radic, "Multicast Parametric Synchronous Sampling," IEEE Photonics Technology Letters **20**, 1222-1224 (2008).

32. C.-S. Bres, A. O. J. Wiberg, B. P.-P. Kuo, J. M. Chavez Boggio, C. F. Marki, N. Alic, and S. Radic, "Optical Demultiplexing of 320 Gb/s to 8 × 40 Gb/s in Single Parametric Gate," IEEE Journal of Lightwave Technology **28**, 434-442 (2010).

33. M. Skold, M. Westlund, H. Sunnerud, and P. A. Andrekson, "All-Optical Waveform Sampling in High-Speed Optical Communication Systems Using Advanced Modulation Formats," IEEE Journal of Lightwave Technology **27**, 3662-3671 (2009).

34. N. Alic, E. Myslivets, S. Moro, B. P.-P. Kuo, R. M. Jopson, C. J. McKinstrie, and S. Radic, "Microsecond Parametric Optical Delays," IEEE Journal of Lightwave Technology **28**, 448-455 (2010).

35. Q. Lin, R. Jiang, C. F. Marki, C. J. McKinstrie, R. M. Jopson, J. Ford, G. P. Agrawal, and S. Radic, "40-Gb/s Optical Switching and Wavelength Multicasting in A Two-Pump Parametric Device," IEEE Photonics Technology Letters **17**, 2376-2378 (2005).

36. P. A. Andrekson, H. Sunnerud, S. Oda, T. Nishitani, and J. Yang, "Ultrafast, atto-Joule switch using fiber-optic parametric amplifier operated in saturation," Optics Express 16, 10956-10961 (2008).

37. T. Inoue, and S. Namiki, "Pulse compression techniques using highly nonlinear fibers," Laser & Photon. Rev. **2**, 83-99 (2008).

38. B. P.-P. Kuo, and S. Radic, "Fast wideband source tuning by extra-cavity parametric process," Optics Express **19**, 19930-19940 (2010).

39. J. W. Nicholson, A. D. Yablon, P. S. Westbrook, K. S. Feder, and M. F. Yan, "High power, single-mode, all-fiber source of femtosecond pulses at 1550nm and its use in supercontinuum generation," Optics Express **12**, 3025-3034 (2004).

40. S. Radic, C. J. McKinstrie, R. M. Jopson, J. C. Centanni, and A. R. Chraplyvy, "All-Optical Regeneration in One- and Two-Pump Parametric Amplifiers Using Highly Nonlinear Optical Fiber," IEEE Photonics Technology Letters **15**, 957-959 (2003).

41. R. Slavik, F. Parmigiani, J. Kakande, C. Lundstrom, M. Sjodin, P. A. Andrekson, R. Weerasuriya, S. Sygletos, A. D. Ellis, L. Gruner-Nielsen, D. Jakobsen, S. Herstrom, R. Phelan, J. O'Gorman, A. Bogris, D. Syvridis, S. Dasgupta, P. Petropolous, and D. J. Richardson, "All-optical phase and amplitude regenerator for next-generation telecommunication systems," Nature Photonics **4**, 690-695 (2010).

42. R. Jiang, R. E. Saperstein, N. Alic, M. Nezhad, C. J. McKinstrie, J. E. Ford, Y. Fainman, and S. Radic, "Continuous-Wave Band Translation Between the Near-Infrared and Visible Spectral Ranges," IEEE Journal of Lightwave Technology **25**, 58-66 (2007).

43. R. Jiang, C.-S. Bres, N. Alic, E. Myslivets, and S. Radic, "Translation of Gbps Phase-Modulated Optical Signal From Near-Infrared to Visible Band," IEEE J. Lightwav. Technol. **26**, 131-37 (2008).

44. B. P.-P. Kuo, A. O. J. Wiberg, E. Myslivets, D. Blessing, N. Alic, and S. Radic, "Widely-Tunable, Multi-Wavelength Short Wave Infrared Light Source based on

Fiber Optical Parametric Oscillator," in Proc. OFC/NFOEC 2010, San Diego, CA, paper OThA5 (2010).

45. A. Gershikov, E. Shumakher, A. Willinger, and G. Eisenstein, "Fiber parametric oscillator for the 2 μm wavelength range based on narrowband optical parametric amplification," Optics Letters **35**, 3198-3200 (2010).

46. J. M. Chavez Boggio, S. Moro, B. P.-P. Kuo, N. Alic, B. Stossel, and S. Radic, "Tunable Parametric All-Fiber Short-Wavelength IR Transmitter," IEEE J. Lightwave Technol. **28**, 443–447 (2010).

47. P. A. Franken, A. E. Hill, C. W. Peters, and G. Weinreich, "Generation of Optical Harmonics," Physical Review Letters **7**, 118-119 (1961).

48. J. A. Armstrong, N. Bloembergen, J. Ducuing, and P. S. Pershan, "Interactions between Light Waves in a Nonlinear Dielectric," Physical Review **127**, 1918-1939 (1962).

49. R. W. Boyd, *Nonlinear Optics* (Academic Press, 2003), Chapter 1.

50. R. H. Stolen, J. E. Bjorkholm, and A. Ashkin, "Phase-matched three wave mixing in silica fiber optical waveguides," Applied Physics Letters **24**, 308-310 (1974).

51. R. H. Stolen, "Phase-Matched-Stimulated Four-Photon Mixing in Silica-Fiber Waveguides," IEEE Journal of Quantum Electronics **11**, 100-103 (1975).

52. R. H. Stolen, and J. E. Bjorkholm, "Parametric Amplification and Frequency Conversion in Optical Fibers," IEEE Journal of Quantum Electronics **18**, 1062-1072 (1982).

53. D. Gindre, H. Maillotte, J. Monneret, E. Lantz, and C. Froehly, "Coherent picoseconds parametric amplification through a Kerr-induced index grating in a single-mode fiber," Optics Communications **112**, 75-789 (1994).

54. V. I. Karpman, and E. M. Krushkal, "Modulated waves in nonlinear dispersive media," Soviet Physics JETP **28**, 277 (1969).

55. A. Hasegawa, and W. F. Brinkman, "Tunable Coherent IR and FIR Sources Utilizing Modulation Instability," IEEE Journal of Quantum Electronics **16**, 694-697 (1980).

56. K. Tai, A. Hasegawa, and A. Tomita, “Observation of Modulation Instability in Optical Fibers,” Physical Review Letters **56**, 135-138 (1986).

57. A. Owyoung, R. W. Hellwarth, and N. George, “Intensity-Induced Changes in Optical Polarization in Glasses,” Physical Review B **5**, 628-633 (1972).

58. A. G. Green, P. P. Mitra, and L. G. L. Wegener, “Effect of chromatic dispersion on nolinear phase noise,” Optics Letters **28**, 2455-2457 (2003).

59. G. Cappellini, and S. Trillo, “Third-order three-wave mixing in single-mode fibers: exact solutions and spatial instability effects,” J. Opt. Soc. Am. B **8**, 824-838 (1991).

60. C.J. McKinstrie, S. Radic, and A.R. Chraplyvy, “Parametric Amplifiers Driven by Two Pump Waves,” IEEE Journal of Selected Topics in Quantum Electronics **8**, 538-547 (2002).

61. R. M. Jopson, U.S. Patent 5 386 394 (1994).

62. M. Ho, M. E. Marhic, K. Y. K. Wong, and L. Kazovsky, “Narrow linewidth idler generation in fiber four-wave mixing and parametric amplification by dithering two pumps in opposition of phase,” IEEE J. Lightwave Technol. **20**, 469–476 (2002).

63. S. Radic, C. J. McKinstrie, R. M. Jopson, J. C. Centanni, A. R. Chraplyvy, C. G. Jorgensen, K. Brar, and C. Headley, “Selective Suppression of Idler Spectral Broadening in Two-Pump Parametric Architectures,” IEEE Photonics Technology Letters **15**, 673-675 (2003).

64. S. Radic, R. M. Jopson, C. J. McKinstrie, A. H. Gnauck, S. Chandrasekhar, and J. C. Centanni, “Wavelength division multiplexed transmission over standard single-mode fiber using polarization-insensitive signal conjugation in highly nonlinear optical fiber,” OFC/NFOEC, paper PD34, Atlanta, GA, USA (2003).

65. T. Hasegawa, K. Inoue, and K. Oda, “Polarization Independent Frequency Conversion by Fiber Four-Wave Mixing with a Polarization Diversity Technique,” IEEE Photonics Technology Letters **5**, 947-949 (1993).

66. J. M. Chavez Boggio, **S. Moro**, E. Myslivets, J. R. Windmiller, N. Alic, and S. Radic, “155-nm Continuous-Wave Two-Pump Parametric Amplification”, IEEE Photonics Technology Letters **21**, 612–614 (2009).

67. C.-S. Bres, J. M. Chavez Boggio, N. Alic, and S. Radic, “1-to-40 10-Gb/s Channel Multicasting and Amplification in Wideband Parametric Amplifier,” IEEE Photonics Technology Letters **16**, 1417-1419 (2008).

68. C.-S. Bres, N. Alic, E. Myslivets, and S. Radic, “Scalable Multicasting in One-Pump Parametric Amplifier,” IEEE J. Lightwave Technol. **27**, 356–363 (2009).

69. A. C. Turner-Foster, M. A. Foster, R. Salem, A. L. Gaeta, and M. Lipson, “Frequency conversion over two-thirds of an octave in silicon nanowaveguides,” Optics Express **18**, 1904-1908 (2010).

70. M. Szpulak, and S. Fevrier, “Chalcogenide As_2S_s Suspended Core Fiber for Mid-IR Wavelength Conversion Based on Degenerate Four-Wave Mixing,” IEEE Photonics Technology Letters **21**, 884-886 (2009).

71. Q. Lin, O. J. Painter, and G. P. Agrawal, “Nonlinear optical phenomena in silicon waveguides: Modeling and applications,” Optics Express **15**, 16604-16644 (2007).

72. X. Gai, T. Han, A. Prasad, S. Madden, D.-Y. Choi, R. Wang, D. Bulla, and B. Luther-Davies,” Progress in optical waveguides fabricated from chalcogenide glasses,” Optics Express **18**, 26635-26646 (2010).

73. M. E. Marhic, K. K.-Y. Wong, L. G. Kazovsky, “Wide-Band Tuning of the Gain Spectra of One-Pump Fiber Optical Parametric Amplifiers,” IEEE Journal of Selected Topics in Quantum Electronics **10**, 1133-1141 (2004).

74. C. J. McKinstrie, M. Yu, M. G. Raymer, and S. Radic, “Quantum noise properties of parametric processes,” Optics Express **13**, 4986-5012 (2005).

75. W. H. Louisell, *Radiation and Noise in Quantum Electronics* (McGraw-Hill, 1964).

76. P. Kylemark, M. Karlsson, T. Torounidis, and P. A. Andrekson, “Noise Statistics in Fiber Optical Parametric Amplifiers,” IEEE Journal of Lightwave Technology **25**, 612-620 (2007).

77. Z. Tong, A. Bogris, M. Karlsson, and P. Andrekson, “Full characterization of the signal and idler noise figure spectra in single-pumped fiber optical parametric amplifiers,” Optics Express **18**, 2884-2893 (2010).

78. J. P. Gordon, and L. F. Mollenauer, “Phase noise in photonic communication systems using linear amplifiers,” Optics Letters **15**, 1351-1353 (1990).

79. Y. Kim, S. Kim, Y.-J. Kim, H. Hussein, S.-W. Kim, "Er-doped fiber frequency comb with mHz relative linewidth," Optics Express **17**, 11972-11977 (2009).

80. N. Nishizawa, and J. Takayanagi, "Octave spanning high-quality supercontinuum generation in all-fiber system," J. Opt. Soc. Am. B **24**, 1786-1792 (2007).

81. N. R. Newbury, and W. C. Swann, "Low-noise fiber-laser frequency combs," J. Opt. Soc. Am. B **24**, 1756-1770 (2007).

82. S. J. McNaught, J. E. Rothenberg, P. A. Thielen, M. G. Wickham, M. E. Weber, and G. D. Goodno, "Coherent Combining of a 1.26-kW Fiber Amplifier," Advanced in Solid-State Photonics, paper AMA2 (2010).

83. K.-P. Ho, *Phase-Modulated Optical Communication Systems* (Springer, 2005), Chap. 5.

84. M. Skold, J. Yang, H. Sunnerud, M. Karlsson, S. Oda, and P. Andrekson, "Constellation diagram analysis of DPSK signal regeneration in a saturated parametric amplifier," Optics Express **16**, 5974-5982 (2008).

85. M. Skold, M. Karlsson, S. Oda, H. Sunnerud, and P. A. Andrekson, "Constellation diagram measurements of induced phase noise in a regenerating parametric amplifier," Optical Fiber Communications Conference, paper OML4 (2008).

86. M. Matsumoto, "Phase noise generation in an amplitude limiter using saturation of a fiber-optic parametric amplifier," Optics Letters **33**, 1638-1640 (2008).

87. R. Elschner, K. Petermann, "Impact of Pump-Induced Nonlinear Phase Noise on Parametric Amplification and Wavelength Conversion of Phase-Modulated Signals," European Conference in Optical Communications, paper 3.3.4 (2009).

88. A. Durecu-Legrand, A. Mussot, C. Simmoneau, D. Bayart, T. Sylvestre, E. Lantz, and H. Maillotte, "Impact of pump phase modulation on system performances of fiber optical parametric amplifiers," Electronics Letters **41**, 350-352 (2005).

89. P. Kylemark, J. Ren, Y. Myslivets, N. Alic, S. Radic, P. A. Andrekson, and Magnus Karlsson, "Impact of Pump Phase-Modulation on the Bit-Error Rate in Fiber-Optical Parametric-Amplifier-Based Systems, IEEE Photonics Technology Letters **19**, 79-81 (2007).

90. R. Elschner, C.-A. Bunge, B. Huttl, A. Gual i Coca, C. Schmidt-Langhorst, R. Ludwig, C. Schubert, and K. Petermann, "Impact of Pump-Phase Modulation on

FWM-Based Wavelength Conversion of D(Q)PSK Signals," IEEE J. Sel. Top. Quant. Elec. **14**, 666-673 (2008).

91. E. Desurvire, *Erbium-Doped Fiber Amplifiers: Principles and Applications* (Wiley-Interscience, 2002).

92. N. Alic, G. C. Papen, R. E. Saperstein, L. B. Milstein, and Y. Fainman, "Signal statistics and maximum likelihood sequence estimation in intensity modulated fiber optic links containing a single optical preamplifier," Optics Express **13**, 4568-4579 (2005).

93. G. P. Agrawal, *Nonlinear Fiber Optics* (Elsevier, 2007), Chap. 10.

94. J. Hansryd, and P. A. Andrekson, "Broad-Band Continuous-Wave-Pumped Fiber Optical Parametric Amplifier with 49-dB Gain and Wavelength-Conversion Efficiency," IEEE Photonics Technology Letters **13**, 194-196 (2001).

95. J. B. Coles, B. P.-P. Kuo, N. Alic, S. Moro, C-S Bres, J. M. Chavez Boggio, P. A. Andrekson, M. Karlsson, and S. Radic, "Bandwidth-efficient phase modulation techniques for stimulated Brillouing scattering suppression in fiber optic parametric amplifiers," Optics Express **18**, 18138-18150 (2010).

96. J. W. Goodman, *Statistical Optics* (Wiley, 1985), Chap. 2.

97. K. Shimoda, H. Takashi, and C. H. Townes, "Fluctuations in Amplification of Quanta with Application to Maser Amplifiers," J. Phys. Soc. Japan **12**, 686-700 (1957).

98. J. P. Gordon, W. H. Louisell, and L. R. Walker, "Quantum fluctuations and noise in parametric processes II," Phys. Rev. **129**, 481-485 (1963).

99. A. V. Kozlovskii, "Photodetection of a weak light signal in various quantum states by using an optical amplifier," Quantum Electronics **36**, 280-286 (2006).

100. H. Kim, "Cross-Phase-Modulation-Induced Nonlinear Phase Noise in WDM Direct-Detection DPSK Systems," IEEE Journal of Lightwave Technology **21**, 1770-1774 (2003).

101. R. Loudon, *The Quantum Theory of Light* (Oxford University Press, 2000).

102. J. W. Goodman, *Statistical Optics* (Wiley, 1985), Chap. 3.

103. P. G. Hoel, S. C. Port, and C. J. Stone, *Introduction to Stochastic Processes* (Waveland Press, 1987).

104. S. Moro, E. Myslivets, J. R. Windmiller, N. Alic, J. M. Chavez Boggio, and S. Radic, "Synthesis of Equalized Broadband Parametric Gain by Localized Dispersion Mapping," IEEE Photonics Technology Letters **20**, 1971-1973 (2008).

105. M. Ho, K. Uesaka, M. Marhic, Y. Akasaka, and L.G. Kazovsky, "200-nm-Bandwidth Fiber Optical Parametric Amplifier Combining Parametric and Raman Gain," IEEE Journal of Lightwave Technology **19**, 977-981 (2001).

106. G. P. Agrawal, *Lightwave Technology: Telecommunication Systems* (Wiley-Interscience, 2005).

107. Yi Bin Lu, P.L. Chu, A. Alphones, and P. Shum, "A 105-nm Ultrawide-Band Gain-Flattened Amplifier Combining C- and L-Band Dual-Core EDFAs in a Parallel Configuration," IEEE Photonics Technology Letters **16**, 1640-1642 (2004).

108. A. Mori, H. Masuda, K. Shikano, and M. Shimizu, "Ultra-Wide-Band Tellurite-Based Fiber Raman Amplifier," IEEE Journal of Lightwave Technology **21**, 1300-1306 (2003).

109. M. Karlsson, "Four-wave mixing in fibers with randomly varying zero-dispersion wavelength," J. Opt. Soc. Amer. B **15**, 2269-2275 (1998).

110. F. Yaman, Q. Lin, S. Radic, and G.P. Agrawal, "Impact of Dispersion Fluctuations on Dual-Pump Fiber-Optic Parametric Amplifers," IEEE Photonics Technology Letters **16**, 1292-1294 (2004).

111. E. Myslivets, N. Alic, T. Nakanishi, T. Okuno, M. Hirano, M. Onishi and S. Radic, "High Resolution Measurement of Nearly Dispersionless Fiber by Localized Four Photon Mixing," OFC, paper PDP11, San Diego, USA (2008).

112. T. Torounidis, and P. Andrekson, "Broadband Single-Pumped Fiber-Optic Parametric Amplifiers," IEEE Photonics Technology Letters **19**, 650-652 (2007).

113. E. Myslivets, N. Alic, J. R. Windmiller, and S. Radic, "A New Class of High-Resolution Measurements of Arbitrary-Dispersion Fibers: Localization of Four-Photon-Mixing Process," IEEE Journal of Lightwave Technology **27**, 364-375 (2009).

114. J.M. Chavez Boggio, and H.L. Fragnito, “Simple four-wave-mixing-based method for measuring the ratio between the third- and fourth-order dispersion in optical fibers,” J. Opt. Soc. Am. B **24**, 2046-2054 (2007).

115. M.J. Hamp, J. Wright, M. Hubbard, and B. Brimacombe, “Investigation into the Temperature Dependence of Chromatic Dispersion in Optical Fiber,” IEEE Photonics Technology Letters **14**, 1524-1526 (2002).

116. J. Hansryd, F. Dross, M. Westlund, P.A. Andrekson, and S.N. Knudsen, “Increase of the SBS Threshold in a Short Highly Nonlinear Fiber by Applying a Temperature Distribution,” IEEE Journal of Lightwave Technology **19**, 1691-1697 (2001).

117. A. Mussot, E. Lantz, A. Durecu-Legrand, C. Simonneau, D. Bayart, T. Sylvestre, and H. Maillote, “Zero-Dispersion Wavelength Mapping in Short Single-Mode Optical Fibers Using Parametric Amplification,” IEEE Photonics Technology Letters **18**, 22-24 (2006).

118. Y. Chen, and A. W. Snyder, “Four-photon parametric mixing in optical fibers: effect of pump depletion,” Optics Letters **14**, 87-89 (1989).

119. M. Marhic, K. K. Y. Wong, M. C. Ho, and L. G. Kazovsky, “92% pump depletion in a continuous-wave one-pump fiber optical parametric amplifier,” Optics Letters **26**, 620-622 (2001).

120. N. Alic, R. M. Jopson, J. Ren, E. Myslivets, R. Jiang, A. H. Gnauck, and S. Radic, “Impairments in deeply-saturated optical parametric amplifiers for amplitude- and phase-modulated signals,” Optics Express **15**, 8997-9008 (2007).

121. T. Torounidis, P. A. Andrekson, and B.-E. Olsson, “Fiber-Optical Parametric Amplifier With 70-dB Gain,” IEEE Photonics Technology Letters **18**, 1194-1196 (2006).

122. Y. Liang, Jia Li, P. C. Chu, and K. K. Y. Wong, “High-Sensitivity Optical Preamplifer for WDM Systems Using an Optical Parametric Amplifier,” IEEE Photonics Technology Letters **21**, 1562-1564 (2009).

123. A. H. Gnauck, and P. J. Winzer, “Optical Phase-Shift-Keyed Transmission,” IEEE Journal of Lightwave Technology **23**, 115-130 (2005).

124. D. Derickson, *Fiber Optic Test and Measurement* (Prentice Hall, 1998), Ch. 13.

125. K. K. Y. Wong, et al., “Polarization-Independent Two-Pump Fiber Optical Parametric Amplifier,” IEEE Photonics Technology Letters **14**, 911-913 (2002).

126. E.-G. Neumann, *Single-Mode Fibers: Fundamentals* (Springer-Verlag, 1988).

127. E. Nisbet, and R. Weiss, “Top-Down Versus Bottom-Up,” Science **328**, 1241-1243 (2010).

128. B. B. Stephens, K. R. Gurney, P. T. Tans, C. Sweeney, W. Peters, L. Bruhwiler, P. Ciais, M. Ramonet, P. Bousquet, T. Nakazawa, S. Aoki, T. Machida, G. Inoue, N. Vinnichenko, J. Lloyd, A. Jordan, M. Heimann, O. Shibistova, R. L. Langefelds, L. P. Steele, R. J. Francey, A. S. Denning, “Weak Northern and Strong Tropical Land Carbon Uptake from Vertical Profiles of Atmospheric CO_2,” Science **316**, 1732-1735 (2007).

129. S. L. Lewis, G. Lopez-Gonzalez, B. Sonke, K. Affum-Baffoe, T. R. Baker, L. O. Ojo, O. L. Phillips, J. M. Reitsma, L. White, J. A. Comiskey, M.-N. Djuikouo K., C. E. N. Ewango, T. R. Feldpausch, A. C. Hamilton, M. Gloor, T. Hart, A. Hladik, J. Lloyd, J. C. Lovett, J.-R. Makana, Y. Malhi, F. M. Mbago, H. J. Ndangalasi, J. Peacock, K. S.-H. Peh, D. Sheil, T. Sunderland, M. D. Swaine, J. Taplin, D. Taylor, S. C. Thomas, R. Votere, and H. Woll, “Increasing carbon storage in intact African tropical forests,” Nature **457**, 1003-1006 (2009).

130. S. Piao, J. Fang, P. Ciais, P. Peylin, Y. Huang, S. Sitch, and T. Wang, “The carbon balance of terrestrial ecosystems in China,” Nature **458**, 1009-1013 (2009).

131. W. Peters, A. R. Jacobson, C. Sweeney, A. E. Andrews, T. J. Conway, K. Masarie, J. B. Miller, L. M. P. Bruhwiler, G. Petron, A. I. Hirsch, D. E. J. Worthy, G. R. van der Werf, J. T. Randerson, P. O. Wennberg, M. C. Krol, and P. P. Tans, “An atmospheric perspective on North American carbon dioxide exchange: Carbon Tracker,” PNAS **104**, 18925-18930 (2007).

132. G. R. van der Werf, D. C. Morton, R. S. DeFries, J. G. J. Olivier, P. S. Kasibhatla, R. B. Jackson, G. J. Collatz, and J. T. Randerson, “CO_2 emissions from forest loss,” Nature Geoscience **2**, 737-738 (2009).

133. M. O. Andreae, and P. Merlet, “Emission of trace gases and aerosols from biomass burning,” Global Biogeochemical Cycles **15**, 955-966 (2001).

134. A. Lavrov, A. B. Utkin, R. Vilar, and A. Fernandes, “Applications of lidar in ultraviolet, visible, and infrared ranges for early forest fire detection,” Applied Physics B **76**, 87-95 (2003).

135. J. S. Gregg, L. M. Losey, R. J. Andres, T. J. Blasing, and G. Marland, "The Temporal and Spatial Distribution of Carbon Dioxide Emissions from Fossil-Fuel Use in North America," Journal of Applied Meteorology and Climatology **48**, 2528-2542 (2009).

136. R. T. Menzies, and D. M. Tratt, "Differential laser absorption spectrometry for global profiling of tropospheric carbon dioxide: selection of optimum sounding frequencies for high-precision measurement," Applied Optics **42**, 6569-6577 (2003).

137. L. S. Rothman, et al., "The HITRAN 2008 molecular spectroscopic database," Journal of Quantitative Spectroscopy & Radiative Transfer **110**, 533-572 (2009).

138. A. Boskovic, S. V. Chernikov, J. R. Taylor, L. Gruner-Nielsen, and O. A. Levring, Direct continuous-wave measurement of n_2 in various types of telecommunication fiber at 1.55 μm," Optics Letters **21**, 1966-1968 (1996).

139. F. Gholami, J. M. Chavez Boggio, S. Moro, N. Alic, and S. Radic, "Measurement of ultra-low fourth order dispersion coefficient in nonlinear fiber by distant low-power FWM," IEEE Photonics Society Summer Topical Meeting, paper WC1.1, Playa Del Carmen, Mexico (2010).

140. V. A. Kovalev, and W. E. Eichinger, *Elastic Lidar: Theory, Practice, and Analysis Methods* (Wiley, 2004), Ch. 7.

141. S. Kameyama, T. Ando, K. Asaka, Y. Hirano, and S. Wadaka, "Compact all-fiber pulsed coherent Doppler lidar system for wind sensing," Applied Optics **46**, 1953-1962 (2007).

142. T. Miya, Y. Terunuma, T. Hosaka, and T. Miyashita, "Ultimate low-loss single-mode fibre at 1.55 μm," Electronics Letters **15**, 106-108 (1979).

143. O. Humbach, H. Fabian, U. Grzesik, U. Haken, and W. Heitmann, "Analysis of OH absorption bands in synthetic silica," Journal of Non-Crystalline Solids **203**, 19-26 (1996).

144. J. D. Shephard, W. N. MacPherson, R. R. J. Maier, J. D. C. Jones, and D. P. Hand, M. Mohebbi, A. K. George, P. J. Roberts, and J. C. Knight, "Single-mode mid-IR guidance in a hollow-core photonics crystal fiber," Optics Express **13**, 7139-7144 (2005).

145. J. M. Chavez Boggio, S. Zlatanovic, F. Gholami, J. M. Aparicio, S. Moro, K. Balch, N. Alic, and S. Radic, "Linear and Nonlinear Properties of Ultra-Compact Fiber Device," OFC/NFOEC, paper OWT8, San Diego, USA (2010).

146. S. Sakaguchi, and S. Todoroki, "Optical properties of GeO_2 glass and optical fibers," Applied Optics **36**, 6809-6814 (1997).

147. J. S. Sanghera, I. D. Aggarwal, eds., *Infrared Fiber Optics* (CRC Press, 1998).

148. F. Urbach, "The Long-Wavelength Edge of Photographic Sensitivity and of the Electronic Absorption of Solids," Physical Review **92**, 1324-1324 (1953).

149. Private communication with iRphotonics, Inc., product: iGuide single-mode infrared fiber, website: http://www.irphotonics.com/

150. G. Ghosh, "Sellmeier coefficients and Chromatic Dispersion for Some Tellurite Glasses," Journal of American Ceramic Society **78**, 2828-2830 (1995).

151. P. Klocek, *Handbook of Infrared Optical Materials*, (CRC Press, 1991).

152. J. M. Harbold, F. O. Ilday, F. W. Wise, J. S. Sanghera, V. Q. Nguyen, L. B. Shaw, and I. D. Aggarwal, "Highly nonlinear As-S-Se glasses for all-optical switching," Optics Letters **27**, 119-121 (2002).

153. R. E. Slusher, G. Lenz, J. Hodelin, J. Sanghera, L. B. Shaw, and I. D. Aggarwal, "Large Raman gain and nonlinear phase shifts in high-purity As_sSe_3 chalcogenide fibers," Journal of Optical Society of America B **21**, 1146-1154 (2004).

154. B. Bendow, "Fundamental Optical Phenomena in Infrared Window Materials," Annual Review of Material Science **7**, 23-53 (1977).

155. M. E. Lines, "The Search for Very Low Loss Fiber-Optic Materials," Science **226**, 663-668 (1984).

156. M. DiDomenico, "Material Dispersion in Optical Fiber Waveguides," Applied Optics **11**, 652-654 (1972).

157. S. H. Wemple, "Optical oscillator strengths and excitation energies in solids, liquids, and molecules," Journal of Chemical Physics **67**, 2151-2168 (1977).

158. M. E. Lines, Bond-orbital theory of linear and nonlinear electronic response in ionic crystals. I. Linear response," Physical Review B **41**, 3372-3382 (1990).

159. M. E. Lines, "Bond-orbital theory of linear and nonlinear electronic response in ionic crystals. II. Nonlinear response," Physical Review B **41**, 3383-3390 (1990).

160. M. E. Lines, "Oxide glasses for fast photonic switching: A comparative study," Journal of Applied Physics **69**, 6876-6884 (1991).

161. S.-H. Kim, T. Yoko, and S. Sakka, "Linear and Nonlinear Optical Properties of TeO_2 Glass," Journal of American Ceramic Society **76**, 2486-2490 (1993).

162. G. Lenz, J. Zimmermann, T. Katsufuji, M. E. Lines, H. Y. Hwang, S. Spalter, R. E. Slusher, S.-W. Cheong, J. S. Sanghera, and I. D. Aggarwal, "Large Kerr effect in bulk Se-based chalcogenide glasses," Optics Letters **25**, 254-256 (2000).

163. S. H. Wemple, and M. DiDomenico, "Behavior of the Electronic Dielectric Constant in Covalent and Ionic Materials," Physical Review B **3**, 1338-1351 (1971).

164. L. H. Gabrielli, H. E. Hernandez-Figueroa, and H. L. Fragnito, "Robustness Optimization of Fiber Index Profiles for Optical Parametric Amplifiers," IEEE Journal of Lightwave Technology **27**, 5571-5579 (2009).

165. A. S. Y. Hsieh, S. G. Murdoch, S. Coen, R. Leonhardt, and J. D. Harvey, "Influence of Raman susceptibility on optical parametric amplification in optical fibers," Optics Letters **32**, 521-523 (2007).

166. Q. Lin, F. Yaman, and G. P. Agrawal, "Raman-Induced Polarization-Dependent Gain in Parametric Amplifiers Pumped With Orthogonally Polarized Lasers," IEEE Photonics Technology Letters **18**, 397-399 (2006).

167. P. L. Voss and P. Kumar, "Raman-noise-induced noise-figure limit for $\chi^{(3)}$ parametric amplifiers," Optics Letters **29**, 445-447 (2004).

168. R. Tang, P. L. Voss, J. Lasri, P. Devgan, and P. Kumar, "Noise-figure limit of fiber-optical parametric amplifiers and wavelength converters: experimental investigation," Optics Letters **29**, 2372-2374 (2004).

169. N. R. Newbury, "Pump wavelength dependence of Raman gain in single mode optical fibers," Journal of Lightwave Technology 21, 3364-3373 (2003).

170. J. Bromage, K. Rotwitt, and M. E. Lines, “A Method to Predict the Raman Gain Spectra of Germanosilicate Fibers With Arbitrary Index Profiles,” IEEE Photonics Technology Letters **14**, 24-26 (2002).

171. A.W. Snyder, and J. Love, *Optical Waveguide Theory* (Springer, 1983).

172. K. Kawano, and T. Kitoh, *Introduction to Optical Waveguide Analysis* (Wiley, 2001), Chapter 4.

173. G. P. Agrawal, *Nonlinear Fiber Optics* (Elsevier, 2007), Chapter 2.

174. K. J. Blow, and D. Wood, “Theoretical description of transient stimulated Raman scattering in optical fibers”, IEEE Journal of Quantum Electronics **25**, 2665–2673 (1989).